

**EFFECTS OF JOINT CONSTRAINTS ON
DEFORMATION OF MULTI-BODY COMPLIANT
MECHANISMS**

A Thesis
Presented to
The Academic Faculty

by
Jiajie Guo

In Partial Fulfillment
Of the Requirements for the Degree
Doctor of Philosophy in Mechanical Engineering

Georgia Institute of Technology
Atlanta, Georgia
December 2011

**EFFECTS OF JOINT CONSTRAINTS ON
DEFORMATION OF MULTI-BODY COMPLIANT
MECHANISMS**

Approved by:

Dr. Kok-Meng Lee, Advisor
School of Mechanical Engineering
Georgia Institute of Technology

Dr. Jun Ueda
School of Mechanical Engineering
Georgia Institute of Technology

Dr. Shreyes N. Melkote
School of Mechanical Engineering
Georgia Institute of Technology

Dr. Yang Wang
School of Civil and Environmental
Engineering
Georgia Institute of Technology

Dr. Lena H. Ting
School of Biomedical Engineering
Georgia Institute of Technology

Date Approved: November 10, 2011

To my parents:

Zhaoqi Guo and Shaozhen Zhang

ACKNOWLEDGEMENTS

I would like to thank Dr. Kok-Meng Lee for his intensive attention and exemplary guidance on my graduate life. I feel very lucky that I can always get immediate advices and extensive supports from him since the first day I came to US. Under his systematic training, I have not only learned academic knowledge and technical skills, but also shaped my mind as a professional researcher and responsible teacher through our daily discussion. I am grateful that he has offered me great opportunities to get involved in different projects, work with many intelligent people and expand my horizon. I always appreciate his metaphor that a great researcher should be like a general who not only can work on details, but also can see broad and think broad. Without his encouragement and patience, this research could not be done. Besides, I would like to acknowledge the supports from my committee members, Dr. Shreyes Melkote, Dr. Jun Ueda, Dr. Yang Wang and Dr. Lena Ting. I especially thank Dr. Wang for his helpful and instructive suggestions to my work.

I would like to thank the GTRI staffs especially Garry McMurray, Wayne Daley, Josh Bailey, Jonathan Holmes and Wiley Holcombe for their helps on experiment in the intelligent cutting project. I also appreciate collaboration with Dapeng Zhu and Xiaohua Yi at Civil Engineering in the structural health monitoring project. Machine shop staffs, John Graham and Louis Boulanger, also provide many suggestions and helps on these projects. I also want to acknowledge my current and former colleagues in the AIMRL group, especially Dr. Shaohui Foong, Jungyoul Lim, Kun Bai, Yang Xie, as well as

visiting scholars Xianmin Chen, Zihua Zhao and Wei Wang. Discussion and cooperation with all of them has led to results in this thesis.

Finally, I wish to give my special thanks to my parents, Zhaoqi Guo and Shaozhen Zhang, without whose endless loves and cares, I would not become who I am and achieve what I have today.

This thesis research is funded by the Georgia Agriculture Technological Research Program (ATRP) under project numbers N5012-1000, N4432-2800, N5431-1000, N4430-2300, N4419-9200, N4418-8200 and N4410-7200, and National Science Foundation under grant number CMMI-0928095 (Program Manager: Dr. Shih-Chi Liu).

TABLE OF CONTENTS

ACKNOWLEDGEMENTS	IV
LIST OF TABLES	VIII
LIST OF FIGURES	IX
LIST OF SYMBOLS	XII
LIST OF ABBREVIATIONS	XV
SUMMARY	XVI
CHAPTER I INTRODUCTION AND BACKGROUND	1
1.1 BACKGROUND AND MOTIVATION	1
1.2 PROBLEM DESCRIPTION AND OBJECTIVES	4
1.3 REVIEW OF PRIOR WORK.....	5
1.3.1 Beam theory and its applications	6
1.3.2 Contact analysis	8
1.3.3 Numerical Methods	9
1.3.4 Processing of meat products.....	10
1.3.5 Bio-inspired mechanisms (compliant beam in a flexonic car).....	12
1.4 THESIS OUTLINE	13
CHAPTER II CURVATURE-BASED BEAM MODEL.....	15
2.1 COORDINATES	17
2.2 CURVATURE OF A 3D BEAM	20
2.3 KINEMATICS OF A 3D BEAM	23
2.4 SUMMARY.....	36
CHAPTER III GENERALIZED CONSTRAINT	38
3.1 FORMULATION OF KINEMATICS	39
3.1.1 Algorithm	42
3.1.2 Human Knee Kinematics	50
3.2 FORMULATION OF DYNAMICS.....	55
3.3 SUMMARY.....	61
CHAPTER IV MODEL AND ANALYSIS OF A BIO STRUCTURE	62
4.1 FORMULATION OF BIO STRUCTURE MODEL.....	65
4.1.1 Coordinates	66

4.1.2 Bio Joint Constraint on Clavicle	67
4.1.3 Clavicle Model	71
4.1.4 Soft Tissue Mechanics	76
4.2 EXPERIMENTAL INVESTIGATION	77
4.2.1 Elastic modulus of clavicle	78
4.2.2 Ligament mechanics.....	84
4.3 ILLUSTRATIVE APPLICATION TO WING MANIPULATION	86
4.4 SUMMARY.....	89
CHAPTER V DESIGN OF COMPLIANT MECHANISM FOR A FLEXONIC	
MOBILE NODE.....	91
5.1 DESIGN CONCEPT	92
5.2 COMPLIANT BEAM DESIGN.....	97
5.2.1 Sensor attachment	100
5.2.2 Convex corner negotiation	105
5.3 EXPERIMENTS AND MODEL VALIDATION.....	109
5.3.1 Validation of the beam model	112
5.3.2 Effect of gravity on sensor attachment.....	116
5.3.3 Validation of the corner negotiation	118
5.3.4 Modal Analysis	120
5.4 APPLICATIONS WITH 3-D DEFORMATION.....	123
5.4.1 Corner Negotiation within limited space	126
5.4.2 Environment monitoring	130
5.5 SUMMARY.....	135
CHAPTER VI CONCLUSIONS AND FUTURE WORKS.....	137
6.1 CONCLUSIONS.....	137
6.2 FUTURE WORKS.....	139
APPENDIX A DERIVATION OF CURVATURE.....	141
APPENDIX B MULTIPLE SHOOTING METHOD (MSM)	143
REFERENCES.....	145

LIST OF TABLES

Table 1.1 Joints and corresponding models.....	12
Table 2.1 Spring specification and boundary conditions.....	33
Table 2.2 Ring specification and boundary conditions.....	35
Table 3.1 Algorithm for bio-joint kinematics.....	42
Table 3.2 Simulation parameter values.....	43
Table 3.3 Dimension of Ω_A and Ω_B	49
Table 3.4 Geometry approximation.....	52
Table 3.5 Physical parameters of human's lower leg.....	57
Table 4.1 Dimensions of coracoid-keel joint and bones.....	68
Table 4.2 Force sensor and sample dimensions.....	85
Table 4.3 Measured data and simulation results.....	88
Table 5.1 Boundary conditions for generalized constraints.....	98
Table 5.2 Slope angle and critical values.....	103
Table 5.3 Mechanical properties and thickness of the spring steel laminate.....	110
Table 5.4 Steel frame material properties and robot dimensions.....	121
Table 5.5 Comparison of frequencies.....	122
Table 5.6 Numerical values for simulation.....	132

LIST OF FIGURES

Figure 1.1 Ligament-skeletal structure of a chicken-shoulder joint.	3
Figure 1.2 Magnetic wheeled flexonic mobile node (FMN).	4
Figure 2.1 Flow chart of the beam formulation.	16
Figure 2.2 Multi-body compliant mechanism.	18
Figure 2.3 Coordinates for a 3-D compliant beam.	19
Figure 2.4 A 3-D curve.	21
Figure 2.5 Verification with a planar curve (non-constant curvature).	27
Figure 2.6 Verification with a helix curve (constant curvature).	28
Figure 2.7 Verification with a 3-D curve with non-constant curvatures.	29
Figure 2.8 Equilibrium of a beam segment.	31
Figure 2.9 Lateral deflection under axial compression.	34
Figure 2.10 Normalized deformed shape of the twisted ring.	36
Figure 2.11 Effect of aspect ratios and materials.	36
Figure 3.1 Bio-joint constraint.	39
Figure 3.2 Snapshots illustrating the formulation.	44
Figure 3.3 Effect of shapes on the osculating circle.	45
Figure 3.4 Ellipse – cylinder contact.	45
Figure 3.5 Effect of sliding on contact kinematics.	46
Figure 3.6 Effect of sliding on orientation.	47
Figure 3.7 Snapshots illustrating the effect of shape.	49
Figure 3.8 Effect of Ω_B on Ω_A position / orientation.	50
Figure 3.9 MRI of a cadaver knee.	50
Figure 3.10 Comparison of current contact point C.	53
Figure 3.11 Rolling and sliding velocities of the current contact point (Model 3).	54
Figure 3.12 Coordinates illustrating the knee joint rotation.	55
Figure 3.13 Kinematics of the tibia mass-center.	57
Figure 3.14 Comparing snapshots of an exoskeleton between two knee joint models.	58
Figure 3.15 Force and torque comparison between two knee joint models (with/without exoskeleton).	60
Figure 4.1 The effect of wing manipulation on shoulder location.	63

Figure 4.2 Flow chart of bio structure modeling.	64
Figure 4.3 Ligament-skeletal structure of a chicken carcass.	66
Figure 4.4 Change of shoulder height due to $\Delta\theta_y$	70
Figure 4.5 Change of shoulder position due to $\Delta\theta_x$	70
Figure 4.6 Clavicle deformation.	72
Figure 4.7 Structural hierachy of ligament or tendon.	76
Figure 4.8 Experiment setup with a calibrated linear motor.	79
Figure 4.9 Calibration of the linear motor on the force-voltage relation.	79
Figure 4.10 Relation between pulling force and deflection on clavicles.	81
Figure 4.11 Tests on samples of full clavicles.	82
Figure 4.12 Tests on samples of half clavicles.	83
Figure 4.13 Uniaxial extension of ligaments [46].	84
Figure 4.14 Ligament / tendon charateristic relation.	87
Figure 5.1 Design concept of an FMN.	93
Figure 5.2 A steel bridge on Georgia Tech campus.	94
Figure 5.3 The compliant beam buckling.	94
Figure 5.4 Compliant beam bending.	95
Figure 5.5 Twisting for a 90° direction change.	96
Figure 5.6 Twist / bend for direction change on different surfaces.	96
Figure 5.7 Effect of gravity.	101
Figure 5.8 Relationship between normalized force and displacements.	104
Figure 5.9 Convex corner negotiation.	105
Figure 5.10 Simulation of corner negotiation.	107
Figure 5.11 Relation between rotation angle θ and required moment M_r	108
Figure 5.12 Relation between rotation angle α and normalized force n	109
Figure 5.13 Prototype FMN.	111
Figure 5.14 Validation of the beam model.	113
Figure 5.15 Model validation with FEM and experiment.	115
Figure 5.16 Validation of sensor attachment.	117
Figure 5.17 Convex right corner negotiation.	119
Figure 5.18 Steel frame structure.	120
Figure 5.19 Comparison of FMN with rigid configuration design.	121

Figure 5.20 FFT of vertical vibration in the steel frame.....	123
Figure 5.21 Prototype of FMN with a camera.....	124
Figure 5.22 Design of the compliant beam.....	125
Figure 5.23 Turning within limited space.....	126
Figure 5.24 Snapshots of the deformed beam.....	128
Figure 5.25 Normalized displacement and force.....	129
Figure 5.26 Front axle yawing and pitching.....	130
Figure 5.27 Deformed beam shapes for a pitching camera.....	133
Figure 5.28 Required input of the rear axle for different of ψ and θ	134

LIST OF SYMBOLS

Capitalized Symbols

A	Cross section area
C	An instantaneous contact point
E	Young's Modulus
G	Shear Modulus
I_1, I_2, I_3	Moment of inertia
J	Moment of inertia
L	Beam length
N_r	Number of rigid bodies in a multi-body system
N_c	Number of compliant beam in a multi-body system
P_s	Material point on the initial beam axis
Q_s	Material point on the deformed beam axis
XYZ	Global reference coordinate frame
$\mathbf{E}_1, \mathbf{E}_2$ and \mathbf{E}_3	Unit vectors along global referenced frame X, Y and Z axes, respectively
$\mathbf{F} = [F_1 F_2 F_3]^T$	External force acting on a compliant beam
$\mathbf{K}^{(0)}$	Curvature of the initial beam
$\mathbf{K}^{(e)}$	Curvature change due to elastic deformation
\mathbf{K}	Curvature of the deformed beam
$Skew(\mathbf{K})$	$\begin{bmatrix} 0 & k_3 & -k_2 \\ -k_3 & 0 & k_1 \\ k_2 & -k_1 & 0 \end{bmatrix}$
$\mathbf{M} = [M_1 M_2 M_3]^T$	External Moment acting on a compliant beam

$\mathbf{R}, \mathbf{R}^{(0)}$ Rotational matrix

\mathbf{X} State variables

Lower case symbols

a, b, c Length of principal axis of an ellipsoid

b Beam width

h Beam thickness

k Curvature

m Mass

p pitch

r Radius of an osculating circle at contact point

r_w Wheel radius

s Undeformed path length from the beam root to the reference point

t Time

x_s, y_s and z_s x_s is the longitudinal axis, y_s and z_s are the principal axis of the cross section area in the initial beam

$\mathbf{e}_1^{(0)}, \mathbf{e}_2^{(0)}$ and $\mathbf{e}_3^{(0)}$ unit vectors along principal axes of x_s, y_s and z_s , respectively

$\mathbf{e}_1, \mathbf{e}_2$ and \mathbf{e}_3 unit vectors along principal axes of ξ_s, η_s and ζ_s , respectively

$[\mathbf{e}_T, \mathbf{e}_N, \mathbf{e}_B]$ Frenet-Serret frame where \mathbf{e}_T is the tangent unit vector, \mathbf{e}_N is the normal unit vector and \mathbf{e}_B is the binormal unit vector

\mathbf{f} External force acting on a rigid body

\mathbf{q}_F Distributed force

\mathbf{q}_M Distributed moment

$\mathbf{x}^{(0)} = [x_1^{(0)} \quad x_2^{(0)} \quad x_3^{(0)}]^T$	Global nodal coordinates of initial beam shape
$\mathbf{x} = [x_1 \quad x_2 \quad x_3]^T$	Global nodal coordinates of deformed beam shape

Greek symbols

Ω	Rigid body
Γ	Boundary of a rigid body
α, β	Angles
κ	Curvature
τ	Torsion External moment acting on a rigid body
ψ, θ and φ	Euler angles
ξ_s, η_s and ζ_s	ξ_s is the longitudinal axis, η_s and ζ_s are the principal axis of the cross section area in the deformed beam
ρ	Density
ν	Poisson ratio
ω	Angular velocity
ε	Longitudinal strain on the beam axis
μ	Friction coefficient

Subscripts and superscripts

(0)	Initial state
(e)	Elastic deformation

LIST OF ABBREVIATIONS

2-D	Two dimensional
3-D	Three dimensional
AWM	Automated wing manipulation
BJC	Bio-joint constraint
BVP	Boundary value problem
CBM	Curvature-based beam model
DOF	Degrees of freedom
FE	Finite element
IVP	Initial value problem
MSM	Multiple shooting method
SHM	Structure health monitoring
SM	Shooting method

SUMMARY

Motivated by the interests to understand bio-structure deformation and exploit their advantages to create bio-inspired systems for engineering applications, this thesis presents a curvature-based model for analyzing compliant mechanisms capable of large deformation in a three dimensional (3-D) space.

This thesis formulates the large deformation of a 3-D compliant beam as a boundary value problem (BVP). Unlike other methods, such as finite element (FE) method, that formulate problems based on displacements and/or rotational angles, the BVP formulation has been derived using curvatures that are more fundamental in presenting nonlinear geometries. Since in the case of finite rotation, superposition holds for curvatures but not for rotational angles, the model is much simpler and the resulting computational process is more efficient. The above advantages have been employed in this research to analyze compliant mechanism designs using curvature-based beam models. Along with the method of deriving the compliant members in the same global reference frame, a generalized constraint acting on a compliant mechanism is presented to replace traditional boundary constraints (such as fixed, pinned or sliding constraint) where none or only one degree of freedom (DOF) is allowed. Inspired by the dexterity of a natural biological joint that offers efficient multi-axis rotation, this research extends to the modeling method of a generalized constraint (or referred to here as a bio-joint constraint) to develop designs emulating commonly observed human motions of multi-DOFs . Using a multiple shooting method (MSM), the BVP is treated as an initial value problem and higher order accuracy can be achieved than finite element (FE) methods.

The attractive features of the method, which greatly simplifies the models and improves the computation efficiency of multi-body system deformation where compliant beams play an important role, have been experimentally validated. To demonstrate the applicability of this proposed method to a broad spectrum of applications, the analytical models have been employed (with experimental validation) to investigate the effects of different joint constraints on the mechanism deformations in two practical applications. The first analyzes deformable bio-structures for automated poultry meat processing. The second has led to a compliant mechanism (known as flexonic mobile node) for health monitoring of a ferromagnetic structure. It is expected that the proposed method will find a broad range of applications involving compliant mechanisms.

CHAPTER I

INTRODUCTION AND BACKGROUND

1.1 Background and Motivation

A compliant mechanism is a mechanical system composed of flexible links, which are designed to transfer force/moments to strain energy by large deformations, and have been widely used for many engineering applications such as snap-fits [1], micro grippers [2] and flexure hinges [3]. In recent years, compliant mechanisms have attracted more and more attention for biology related applications, such as food processing industry and bio inspired robotics, because compliant mechanisms exhibit many advantages in dealing with highly deformable biological materials over rigid engineering tools in terms of simple structures and light weight. While multi-body compliant mechanisms can achieve a larger range of motion and are energy efficient because of being free from contact friction, their designs are difficult to analyze and often based on assumptions (such as small deformation and fixed rotation center) in order to reduce the three dimensional (3-D) nonlinear problem to a more tractable two dimensional (2-D) formulation for solving using a lumped-parameter approach. Such simplified analyses

generally yield only first-order approximation, and are unable to capture 3D behaviors such as the coupled effects among bending, twisting, and contact with joint clearances.

This thesis research has been motivated by two practical applications. The first is an immediate application in poultry industry, where boneless breast meat is removed from chicken carcasses for subsequent meat processing [4]. The job requires pulling and then twisting a wing to sever the ligaments/tendons for deboning the meat typically at a rate of 1 bird/second. This repetitive job is a potential cause of cumulative trauma disorder, and thus a candidate for automation. A critical part of this process is the need to manipulate both wings to tension the ligaments and tendon before severing them as illustrated in Figure 1.1, which leads the following questions to be answered: 1) where are the ligaments and tendon located? 2) How much force and torque are required to manipulate the wings? 3) In what directions should the force and torque be applied? Most of the early research effort focused on developing a method (based primarily on vision sensing feedback) to position the cutting blade for the initial insertion. A good understanding of the important factors (such as the structural compliance due to joint clearance and connecting soft tissues) contributing to the whole carcass deformation is essential to the precision deboning. In this thesis, a musculoskeletal structure of a chicken shoulder is modeled as a multi-body compliant mechanism with bio joints to predict the locations of ligaments/tendon and required manipulating forces under large deformation of a carcass. This mechanism differs from others in the sense that rigid bodies (bones) and compliant links (tiny bones / soft tissues) are not connected in series but in a 3-D topology. The deformation of this compliant bio-structure, together with

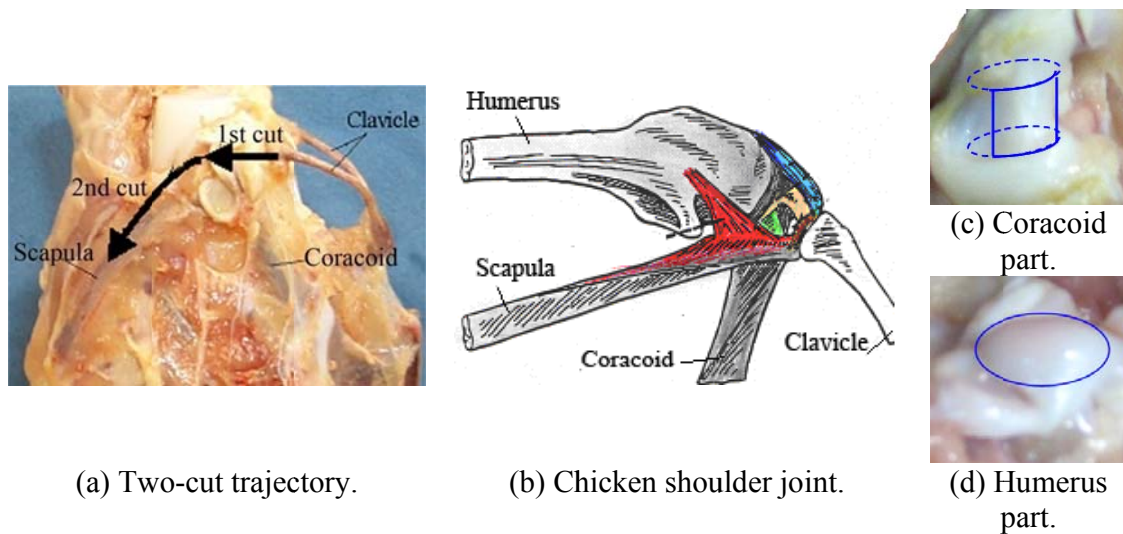
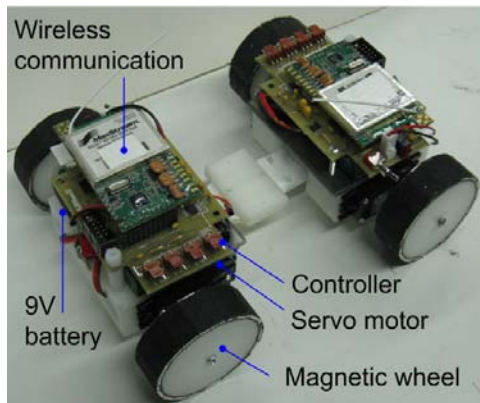


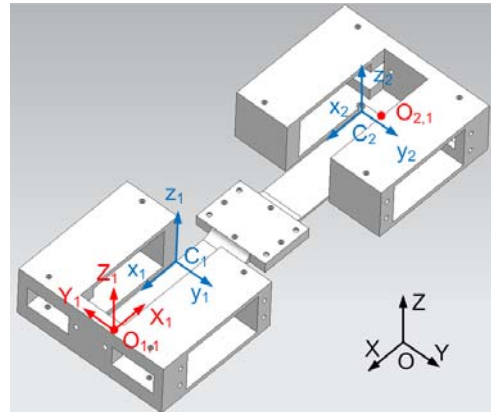
Figure 1.1 Ligament-skeletal structure of a chicken-shoulder joint.

non-uniform joint constraints, will be analyzed using the model for multi-body compliant mechanisms.

The second application is to design a miniature robotic car to serve as a mobile sensor node (MSN) for structure health monitoring (SHM) and dynamic testing of large civil structures (such as ferromagnetic bridges) [5]. Current bridge inspections (relying on visual identification of damages on structure surfaces) are laborious and costly, and limited to once every two years; damages located below the surface often remain elusive to the inspectors. In order to reduce these costs, the MSN should be able to perform two functions; negotiating obstacles within limited space on structures being inspected and attaching/detaching an accelerometer to collect data for vibration analysis. Thus, the mechanical structure of a MSN has to be flexible enough to successfully perform all these functions. Unlike other field robots designed solely on rigid links, compliant links offer more flexibility in maneuvering various poses for the robot, thus it is more adaptive to complex terrains. Moreover, by replacing revolute joints with flexible beams, it also reduces friction between components. When a MSN is incorporated with a compliant



(a) FMN Prototype.



(b) CAD Model.

Figure 1.2 Magnetic wheeled flexonic mobile node (FMN).

mechanism, it is called flexure-based-mechatronic (Flexonic) Mobile Node (FMN). As shown in Figure 1.2, the interest here is the design and control of the flexible link between the front and rear axles of an FMN. Besides, various terrains with limited turning spaces also exert certain motion constraints on the car, which could be regarded as a generalized contact similar to that encountered in a bio joint.

1.2 Problem Description and Objectives

With the emerging applications in mind, there is a need to develop a modeling method for designing and analyzing compliant mechanisms capable of 3-D large deformation. Although many methods are available in modeling flexible structures, challenges still exist in the following aspects:

- 1) Formulations based on local nodal coordinates are not numerically efficient in capturing large deformation, especially for 3-D cases.
- 2) Most existing modeling methods are based on small deformation analysis, such as finite element (FE) methods, which require incremental loadings to achieve large deformation and their performances are not optimal.

- 3) Nonlinearity in material properties and geometries in biological applications brings in new problems to traditional engineering applications.

As a result, the objectives of this thesis include the following:

- 1) Formulate a compliant beam model that is capable of capturing large deformation in 3D space.
- 2) Develop an approach to quantify the nonlinear geometry confronted in biology related applications.
- 3) Given the geometry nonlinearity, design and analyze compliant mechanisms for engineering application.

1.3 Review of Prior Work

Compliant mechanisms have a long history and can be found in our daily life in numerous applications (such as catapults, bows, binder clips, diving boards and clocks). A comprehensive review of compliant mechanisms is beyond the scope for this thesis. The reviews conducted for this thesis research focus on practical issues related to two practical applications that have motivated this research; namely, natural bio-product processing and design of bio-inspired mechanisms. In relation to these applications, several problems arise for designing compliant mechanisms. For example, 2-D models of engineering mechanisms are not suitable for characterizing 3-D natural objects. Assumptions such as small deformation are no longer adequate for design analysis of compliant structures involving large deformation and nonlinear dynamic behaviors. Moreover, typical engineering designs based on fixed rotation centers or standard cylindrical/sphere geometries could not capture the natural properties of contact in bio joints. Typical biological joints can attain limited translational motions in addition to the three rotational freedoms due to the deformability of the connective tissues. Given the

complex assembly with clearances, a biological joint is often compliant and has more degrees of freedom (DOF) than an engineering joint [6, 7]. Existing ball-socket approximations are often inadequate to characterize biological joints and their associated bio-skeleton kinematics. Thus, the contact point between these extraordinary shapes, in general, is difficult to locate.

Given the dimension of the above difficulties, the remaining review begins with related works on the two applications of processing natural objects and bio-inspired mechanisms for field robots. Next, formulations of a compliant beam and contact analysis are addressed. Finally, a review on the MSM for solving boundary value problem (BVP) of a compliant beam large deformation is provided.

1.3.1 Beam theory and its applications

Flexible beams are used as a fundamental component in many compliant mechanisms, and have been modeled using different formulations. The pseudo-rigid-body approach [8] is among the most commonly used approximation, which extends the rigid body analysis by modeling the beam as a torsional spring connecting two rigid links. One of the difficulties in the pseudo-rigid-body approach is to find the beam equivalent stiffness and its location for modeling it as a torsional spring. Although errors of the tip deflection are within 0.5% of exact solutions, it is not accurate about the displacement along the path length.

Distributed beam models for small deformations fall into two main categories: Euler-Bernoulli beam theory [9] and Timoshenko beam theory [10]. Euler-Bernoulli beam theory is also called the classical beam theory, which has been widely used to solve

engineering problems. It assumes material linear elasticity, small deformation, no shear distortions, and plane section normal to the undeformed beam referenced axis remains planar and normal to the deformed axis. Timoshenko beam theory takes shear deformation and rotational inertia effects into account, which is suitable for studying short beams or beams subject to high frequency excitation.

For formulating the large deflection of a two-dimensional beam under various load conditions, Frisch-Fay [11] presented closed form solutions; as the solutions incorporate elliptic integrals, the calculation procedure is cumbersome. Although Frisch-Fay also presented some results for analyzing 3-D beams, closed form solutions are still not available. Numerical methods are generally required to solve for 3-D beam deformation. This thesis research formulates the equations of motion for a 3-D beam based on the model by Pai and Nayfeh [12] for solving using a MSM [13].

In analyzing flexible body dynamics, four groups of formulations have been developed to capture the large displacements and rotations of structural components:

- 1) The floating frame of reference method [14] defines each body deformation with respect to their local body-fixed coordinate systems using modal representation or the FE method.
- 2) The incremental FE method uses infinitesimal rotations as nodal coordinate, which may not be correct to solve large rotation problems [15].
- 3) The large rotation vector method employs large rotation coordinates in the inertial frame, which leads to a simple expression for the kinetic energy but results in redundant representation of derivatives of displacement coordinates besides the rotation coordinate [16, 17].
- 4) More recently, the absolute nodal coordinate formulation which does not require interpolation of finite rotations has been widely used for FE analysis, [18].

1.3.2 Contact analysis

For compliant mechanisms involving contacts, several questions must be answered: 1) Whether there is contact? 2) Where is the contact? 3) What is happening during contact? Numerical methods for determining contact between rigid bodies fall into two formulations. The first is the penalty formulation utilizing the no-interpenetration condition, which avoids the solution existence questions and avoids impulses. The second is the time-stepping formulation that employs complementarity (or optimization) conditions to determine contact or not. Some reviews and recent developments on both formulations can be found from the works of Stewart [19, 20], Song [21], and Adly and Goeleven [22].

For contact problems involving flexible bodies, the two main formulations are the methods of variational inequality (VI) [23] and the variational equality (VE) [24], which have been investigated for frictionless and frictional contact problems respectively. When considering biological joints, contact kinematic problems arise because of the non-uniform shapes of joints. Kelkar et al. [25] quantitatively studied the translational motion of humeral head during the rotation of shoulder joints. Similar results of tibia translational motion in human knee joints are observed in experiments by Iwaki et al. [26]. Yang and Meng [27] used a 3D friction contact model for planar contact and developed analytical criteria to determine the transitions among stick, slip and separation of contact. Montana [28] studied the velocity of a rolling sphere between two grasping fingers of arbitrary shapes.

At Georgia Tech, Lee [29] introduced an analytical model of a compliant grasping mechanism for automated transferring of live objects [30], where multiple rubber fingers

are employed to emulate a pair of human hands. For such a grasping problem, the contact location (between the flexible finger and object) and its corresponding force are not known a priori. To accommodate size and shape variations encountered in grasping live objects, several methods [31, 32] have been proposed to improve the prediction of the contact location and force due to a 2D flexible beam. More recently, Li and Lee [33] developed an adaptive meshless method (MLM) for analyzing stresses due to large deformable contacts on the products being handled. The adaptive MLM, which is similar to FE methods but requires no meshes, increases the nodal density in regions of high mechanical stresses. This thesis research extends the studies to analyze contacts within a bio joint, where both rolling and sliding occurs during contact between two non-engineering geometries.

1.3.3 Numerical Methods

The shooting method (SM) was first proposed by Keller [34] to solve the boundary value problem (BVP) of ordinary differential equations. It transforms the BVP into an initial value problem (IVP) by guessing the unknown initial values first, and then utilizes Newton's methods to iteratively re-evaluate the initial guesses to "shoot" at the terminal values. Like most iterative methods for nonlinear problems, the convergence of SM is also sensitive to the initial guesses. To reduce the solution sensitivity to the initial guesses and thus improve the convergence property, Keller[34], Stoer and Bulirsch [35] developed the multiple SM by dividing the integration region into smaller sections and performing SM within each section. The continuity of the pieced solutions is guaranteed

by adding new constraints on the boundaries of each section, so it greatly increases the scale of the problem size.

Some improved SMs are proposed in recent years. Holsapple et al. [36] used modified SM to “shoot” at intermediate values until the solution matches its terminal value. A generalized SM (GSM) developed by Lan and Lee [32] includes unknown parameters into the formulation in order to solve compliant mechanisms of flexible links in series. Liu [37] used Lie-Group SM to solve BVP with multiple solutions. Most of the SM applications have been devoted to the design analysis of flexible beams and frames [13, 31, 38-40], in which SM is used to study the deflection of the compliant beam rather than the dynamics in time domain. Although Lan et al. [40] formulated the PDE for dynamic analysis, GSM is still limited to solve deformed shape along the path length. SM has been designed to solve ODEs, and little efforts have been made to extend it to solving PDEs until recent years. Chang [41] solved a heat conduction problem with SM; and Liu [42] identified the damping and stiffness by transforming an ODE to PDE.

1.3.4 Processing of meat products

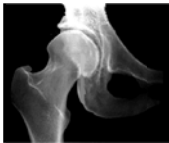
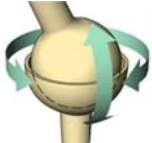

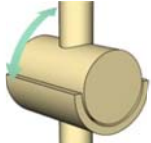


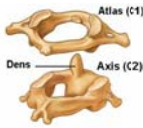
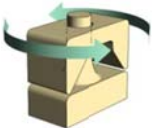



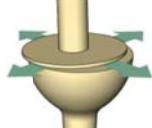
Processing of natural products (such as poultry and meat) requires presentation of the target area for subsequent handling (such as cutting). Bone structures deform as a result of manipulation through bio joints. A good application example is the deboning of chicken breast meat [4], where the shoulder joint must be accurately located for severing the ligaments and tendons. Although marketed deboning machines are available, these “hard automation” systems, in general, are not as dexterous as human labors in handling with highly deformable natural objects. Given the high size/shape variations in natural

products, Sandlin [43] explored a method to correlate the bone locations relative to the external surface features using a combination of X-ray and machine vision images. He [44] investigated the feasibility to emulate human deboning chicken breast meat using a spherical wrist motor [45] by experimentally measuring their arm motion and wrist torque profiles. More recently, Claffee [46] experimentally studied the effect of pulling the wing of a chicken carcass (on a commercial fixture) on the shoulder height suggesting that bio-structural deformation cannot be neglected for precision deboning of chicken breast meat.

Precision deboning requires a good understanding of compliant joints and their effects on fixture designs and manipulation of the biological structure. Unlike an engineering joint where assembled parts are usually concentric cylinders or spheres, biological joints are often a complex assembly of two or more different shaped components as shown in Table 1.1 [47]. Bio joint geometries have also been mathematically described for bio-medical and surgery; see for examples, [26, 48, 49]. With the development of non-contacting scanning technologies (such as MRI and laser beams), relatively accurate 2D and 3D bone geometries can be obtained. However, most real biological joints are approximated by simple geometries (circles and spheres) [26, 49] in order to reduce their highly nonlinear kinematics to a more tractable form. The oversimplified ball-socket approximation generally neglects the joint clearance, and cannot account for deformable effects needed for applications such as breast-meat deboning where percent yields (hence highly precise cutting) are of particular concern.

To provide an essential basis for optimizing the design of a manipulating trajectory for effective cutting, this research develops a more realistic and yet general

Table 1.1 Joints and corresponding models.

					
Hip Joint	Ball-Socket	Elbow Joint	Hinge	Metacarpophalangeal Joint	Condyloid
					
Atlantoaxial Joint	Pivot	Carpometacarpal Joint	Saddle	Acromioclavicular Joint	Plane

model to characterize the bio joint kinematics. The analysis method is presented in the context of poultry processing but also helps analyze the motion of cam mechanisms or engineering joints where wears and tears could result in clearances in the joint and/or non-circular elements.

1.3.5 Bio-inspired mechanisms (compliant beam in a flexonic car)

As field robots have been attracting increasing interests in replacing human labor working in a hazardous or high-risk environment, two issues are of most concerned in the design; attachment and mobility. Using magnetic devices and vacuum suction cups are two major methods to attach a robot on a working surface. Based upon magnetic on-off robotic attachment devices, a magnetic walker has been developed for maneuvering on a 2D surface [50]. In order to inspect carbon steel pipe, a magnetic wheeled robot has been developed to move automatically along the outside [51] and inside [52] of piping. Backes et al. [53] designed a robot for visually inspecting aircraft exterior using suction cups for

adherence and ultrasonic motors for mobility to crawl on a 2D surface. Other attaching methods include aerodynamic attraction [54] and biomimetic approach [55]. However, robots designed based on rigid components often have limited range of motion thus are not adaptable to complicated working environment.

Flexible structures can also be found in compliant robots; see for examples [56-59] where focuses have been on modeling and control. At Georgia Tech [5], the design of a flexure-based mechatronic (flexonic) car for SHM has led to the development of an FMN. The FMN consists of a compliant beam between the front and rear axles carrying magnetic-wheels. The FMN that has more DOF but no relative moving parts is more adaptive to complicated working conditions. As analyzed in [60], the FMN has the potentials to negotiate various obstacles and attach/detach a sensor on the iron surface on which it moves. These attractive features found in the FMN designed at Georgia Tech provide the motivation for further studies in this thesis research, which will be illustrated as an example of a multi-body compliant mechanism.

1.4 Thesis Outline

The remainder of this thesis is organized as follows: Chapter II starts with the formulation of the boundary value problem (BVP) for the large deformation of a 3-D compliant beam, including the derivation of constitutive equations, curvature description and boundary conditions.

Chapter III employs numerical examples to illustrate the procedure in solving the BVP for flexible beam large deformation, which has been formulated in Chapter II. Each

of the examples may focus on one topic, but some of the conclusions are helpful for subsequent discussion.

Chapter IV presents a dimension-based method to characterize bone and soft tissue deformation by accounting for the large size variation of natural products. Both simulation and experimental data are provided to validate the musculo-skeletal model for the compliant chicken carcass under wing manipulation for intelligent cutting.

In Chapter V, a magnetic flexonic mobile node (FMN) incorporating a compliant mechanism has been designed to negotiate corners and carry a sensor for placing on a ferromagnetic structure. Two functions of sensor attachment and corner negotiation are presented for different constraints for the same mechanical design of FMN. Simulation, analysis and experiment are provided for detailed discussion.

Finally, the conclusions of the thesis and recommendations for future work are presented in Chapter VI. Several issues on extending the current work are addressed to increase potential applications of the modeling and analysis method presented in this thesis.

CHAPTER II

CURVATURE-BASED BEAM MODEL

This chapter formulates the large deformation of a 3-D compliant beam as a boundary value problem (BVP) along with the derivation of related beam constitutive equations. The formulation of the boundary conditions, which are application specific, will be covered in the next chapter.

Unlike methods (such as FE methods) that formulate problems based on displacements and/or rotational angles, the formulation in this thesis has been derived using curvature as a fundamental concept in presenting nonlinear geometries. Although curvature has three components (as in the case of displacement and rotational angle) in 3D space, it is independent of coordinate frames while displacement and rotational angle would change with coordinate systems. It is worth noting that in the case of finite rotation, superposition holds for curvatures but not for rotational angles. This is the reason why FEA methods employ incremental approach to solve problems of large deformations. Hence, formulation based on curvature is much simpler; and the resulting computational process is much more efficient – the above advantages motivate the use of Curvature-based Beam Model (CBM) to analyze and design compliant mechanisms.

The organization of this chapter is illustrated in Figure 2.1, which begins with the coordinate systems for describing the beam variables (the nodal coordinates \mathbf{x} , the nodal rotation \mathbf{R} and φ , and the external force \mathbf{F} and moment \mathbf{M}). In Figure 2.1, the superscript $^{(0)}$ and $^{(e)}$ denote the beam initial configuration and elastic deformation respectively. It

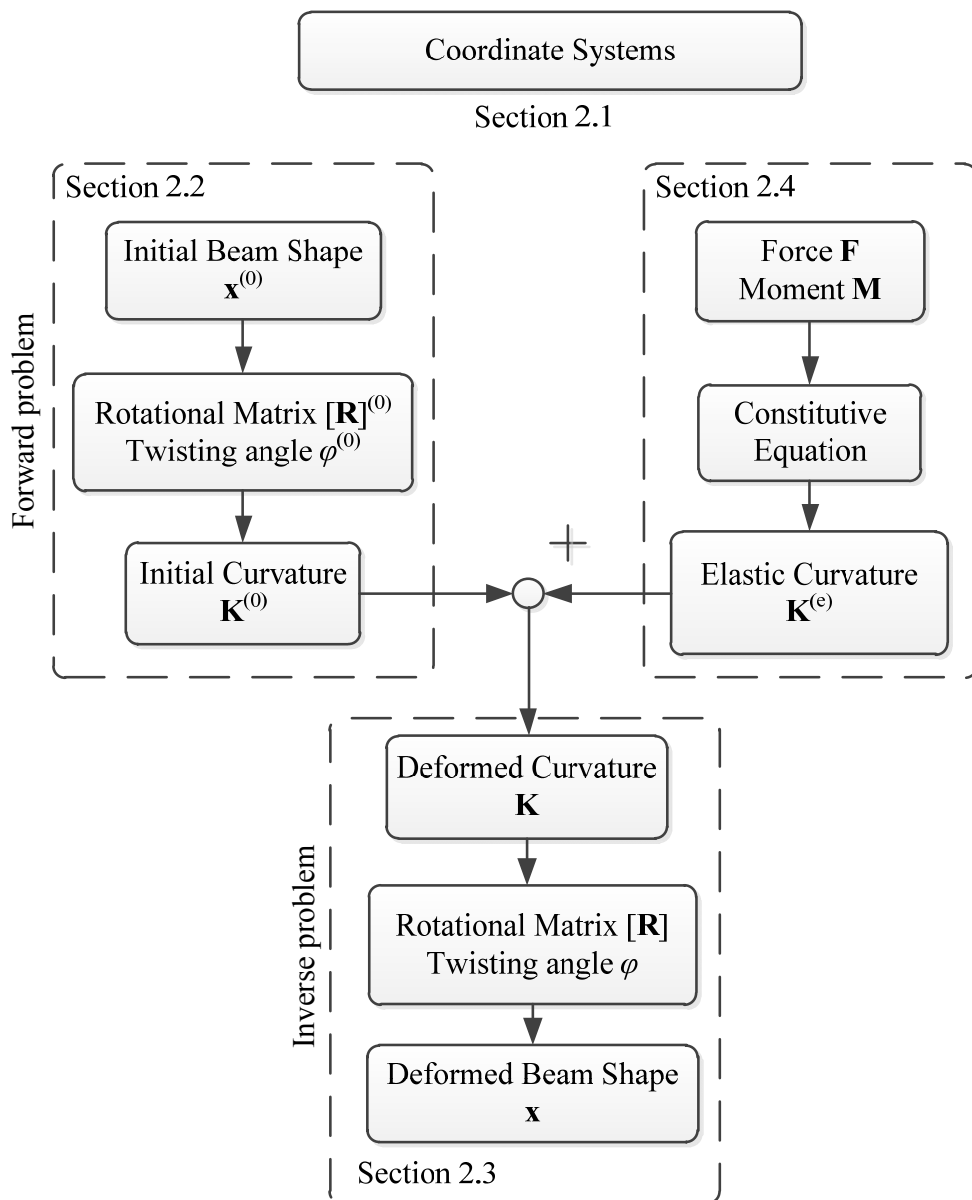


Figure 2.1 Flow chart of the beam formulation.

will be shown that the initial curvature $\mathbf{K}^{(0)}$ can be determined from the initial beam shape $\mathbf{x}^{(0)} = [x_1^{(0)} \ x_2^{(0)} \ x_3^{(0)}]^T$; and that the deformed shape $\mathbf{x} = [x_1 \ x_2 \ x_3]^T$ can be obtained from \mathbf{K} . These forward and inverse processes will be detailed in Sections 2.2 and 2.3. Then the elastic curvature $\mathbf{K}^{(e)}$ will be determined from the beam constitutive relations in Section 2.4. Illustrative numerical examples on curved beam geometry reconstruction and large deformation analysis of 3D curved beams will be used to validate the presented CBM. It is noted that only cantilever constraint will be used in this chapter before any generalized type of boundary condition is discussed in later chapters.

2.1 Coordinates

Figure 2.2 schematically illustrates a multi-body compliant mechanism consisting of N_r rigid bodies and N_c mass-less compliant beams, where $i = 1, 2, \dots, N_r$ and $j = 1, 2, \dots, N_c$. The rigid bodies, each of which has multi-DOF with respect to the global (reference) coordinate system XYZ, are constrained by (rotational and/or sliding) joints or contact (between two rigid bodies i and $i+1$) while the compliant beams (capable of deforming in the 3D space) may be fixed or pinned on the rigid bodies. External forces and moments (denoted as \mathbf{f}_i and $\boldsymbol{\tau}_i$ and \mathbf{F}_j and \mathbf{M}_j in Figure 2.2 respectively) may be applied to the i^{th} rigid body and/or the j^{th} compliant beam. The problem can be formulated in two opposing ways, which are referred to here as forward and inverse problems. The former solves for deformation of the system given the external loadings while the latter determines the required forces/moments for a specified deformation configuration.

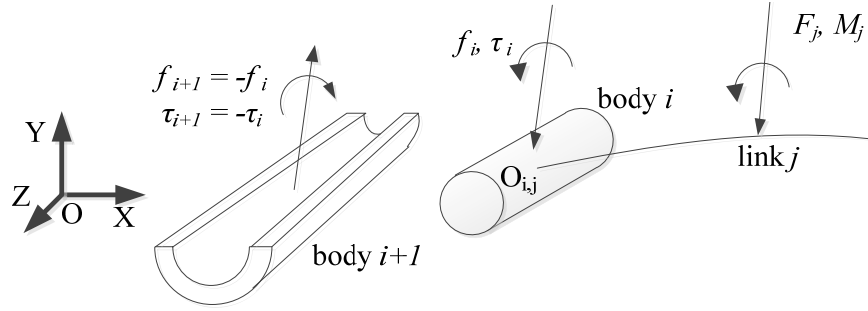


Figure 2.2 Multi-body compliant mechanism.

Specifically, this thesis research investigates the effects of joint constraints on the deformation of a compliant mechanism.

In Figure 2.3, OXYZ is a global reference frame; the local coordinate frames, “xyz” and “ $\xi\eta\zeta$ ” (each with a subscript indicating its location along the beam path-length), are defined in the un-deformed and deformed configurations respectively. For examples, $x_0y_0z_0$ and $x_1y_1z_1$ are the local coordinate frames at P_0 and P_1 in the undeformed configuration, respectively. Similarly, $P_s(x_s, y_s, z_s)$ and $Q_s(\xi_s, \eta_s, \zeta_s)$, represent the same material point to describe the beam shapes before and after deformation respectively, where the subscript s denotes the path-length. All the coordinates follow the right-hand rule with x_s and ξ_s assigned along the neutral axis of the beam, and y_s, z_s, η_s and ζ_s are the principal axes on the corresponding cross-sections. To simplify the formulation, it is assumed that $P_0x_0y_0z_0$ differs from OXYZ only in translation (meaning that their base axes are well aligned without relative rotation); otherwise, there is a rigid body rotation to transform the results into the coordinate system OXYZ.

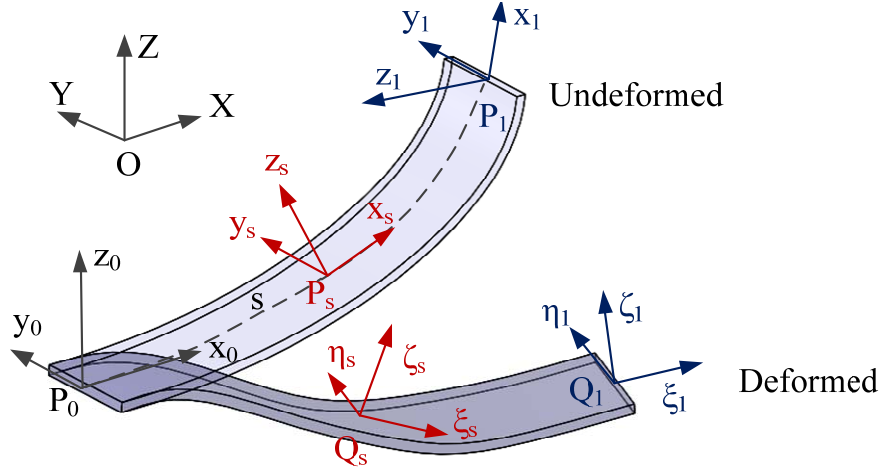


Figure 2.3 Coordinates for a 3-D compliant beam.

To facilitate the discussion, the unit vectors along the coordinate axes are denoted as follows:

\mathbf{E}_1 , \mathbf{E}_2 and \mathbf{E}_3 are unit vectors along X, Y and Z axes, respectively.

$\mathbf{e}_1^{(0)}$, $\mathbf{e}_2^{(0)}$ and $\mathbf{e}_3^{(0)}$ are unit vectors along principal axes of x_s , y_s and z_s , respectively.

\mathbf{e}_1 , \mathbf{e}_2 and \mathbf{e}_3 are unit vectors along principal axes of ξ_s , η_s and ζ_s , respectively.

The initial and deformed curves of the beam axis, $\{\mathbf{e}_i^{(0)}\}$ and $\{\mathbf{e}_i\}$ ($i = 1, 2, 3$), can be obtained by the following relations:

$$\mathbf{e}_i^{(0)} = R_{ij}^{(0)} \mathbf{E}_j \quad (2.1a)$$

$$\mathbf{e}_i = R_{ij} \mathbf{E}_j \quad (2.1b)$$

In (2.1), $R_{ij}^{(0)}$ and R_{ij} (i and $j = 1, 2, 3$) or the components of rotational matrixes $[\mathbf{R}]^{(0)}$ and $[\mathbf{R}]$ respectively are functions of the path length s . It is noted that bases $\{\mathbf{e}_i^{(0)}\}$ and $\{\mathbf{e}_i\}$ only describe the beam axial curve. To account for the 3-D geometry of a beam, one more variable φ or $\varphi^{(0)}$ is needed to quantify the twisting of its cross-section relative to the beam axis.

Since the initial or deformed beam geometry is readily determined by $[\mathbf{R}]^{(0)}$ and $\varphi^{(0)}$ (or $[\mathbf{R}]$ and φ), the task is to find the rotational matrix and twisting angle. Because only three components among the rotational matrix elements and twisting angle are independent, it is better to reduce the order of the problem by using three independent components; namely, the curvature. So the formulation is based on vector superposition of curvatures as given in (2.2) implying that the deformed curvature $\mathbf{K} = [k_1 \ k_2 \ k_3]^T$ is the summation of the initial curvature $\mathbf{K}^{(0)} = [k_1^{(0)} \ k_2^{(0)} \ k_3^{(0)}]^T$ and the elastic curvature $\mathbf{K}^{(e)} = [k_1^{(e)} \ k_2^{(e)} \ k_3^{(e)}]^T$ due to an external loading (of force \mathbf{F} and moment \mathbf{M}):

$$\mathbf{K} = \mathbf{K}^{(0)} + \mathbf{K}^{(e)} \quad (2.2)$$

In summary, thirteen variables are involved in formulating the beam deformation problem; namely, the nodal coordinates $\mathbf{x} = [x_1 \ x_2 \ x_3]^T$, the orientations including first row of $[\mathbf{R}]_1 = [R_{11} \ R_{12} \ R_{13}]$ and twisting angle φ , the force $\mathbf{F} = [F_1 \ F_2 \ F_3]^T$ and moment $\mathbf{M} = [M_1 \ M_2 \ M_3]^T$. The 13 state variables are organized as $\mathbf{X} = [x_1 \ x_2 \ x_3; R_{11} \ R_{12} \ R_{13} \ \varphi; F_1 \ F_2 \ F_3 \ M_1 \ M_2 \ M_3]^T$ with one constraint relation $R_{11}^2 + R_{12}^2 + R_{13}^2 = 1$.

2.2 Curvature of a 3D Beam

As shown in Figure 2.4, the longitudinal axis of a curved beam in the 3-D space is described in a parametric form:

$$\mathbf{x}^{(0)} = x_i^{(0)}(t)\mathbf{E}_i \quad (2.3)$$

where t is not necessary to be the path length but any parameter ranging from t_0 to t_f .

In Figure 2.4, $[\mathbf{e}_T, \mathbf{e}_N, \mathbf{e}_B]$ is the Frenet-Serret frame where \mathbf{e}_T , \mathbf{e}_N and \mathbf{e}_B are the tangent, normal and binormal unit vectors given in [61] as

$$\mathbf{e}_T = \frac{\dot{\mathbf{x}}^{(0)}}{|\dot{\mathbf{x}}^{(0)}|}, \quad \mathbf{e}_N = \frac{\ddot{\mathbf{x}}^{(0)}}{|\ddot{\mathbf{x}}^{(0)}|}, \quad \mathbf{e}_B = \mathbf{e}_T \times \mathbf{e}_N \quad (2.4)$$

where “.” denotes the derivate with respect to t .

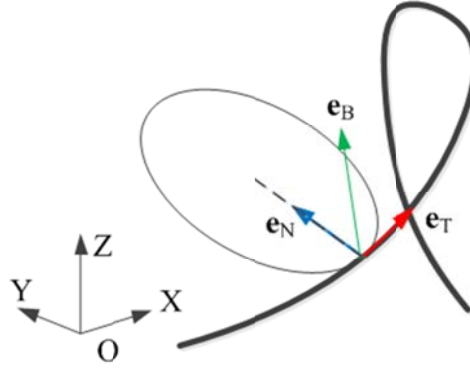


Figure 2.4 A 3-D curve.

The Frenet-Serret formula is provided as:

$$\frac{d}{ds} \begin{Bmatrix} \mathbf{e}_T \\ \mathbf{e}_N \\ \mathbf{e}_B \end{Bmatrix} = \begin{bmatrix} 0 & \kappa & 0 \\ -\kappa & 0 & \tau \\ 0 & -\tau & 0 \end{bmatrix} \begin{Bmatrix} \mathbf{e}_T \\ \mathbf{e}_N \\ \mathbf{e}_B \end{Bmatrix} \quad (2.5)$$

where the path length s can be calculated as a function of t

$$s = \int_{t_0}^t \sqrt{\dot{x}_1^{(0)2} + \dot{x}_2^{(0)2} + \dot{x}_3^{(0)2}} dt \quad (2.6)$$

So the overall length of the curve can be obtained as

$$L = s(t_f) = \int_{t_0}^{t_f} \sqrt{\dot{x}_1^{(0)2} + \dot{x}_2^{(0)2} + \dot{x}_3^{(0)2}} dt \quad (2.7)$$

And the curvature κ and torsion τ are given by

$$\kappa = \frac{|\dot{\mathbf{x}}^{(0)} \times \ddot{\mathbf{x}}^{(0)}|}{|\dot{\mathbf{x}}^{(0)}|^3} \quad (2.8a)$$

$$\tau = \frac{\dot{\mathbf{x}}^{(0)} \cdot (\ddot{\mathbf{x}}^{(0)} \times \ddot{\mathbf{x}}^{(0)})}{|\dot{\mathbf{x}}^{(0)} \times \ddot{\mathbf{x}}^{(0)}|^2} \quad (2.8b)$$

It is noted that $\mathbf{e}_1^{(0)}$ and \mathbf{e}_T are the same unit tangent vector, while $\mathbf{e}_2^{(0)}$ and \mathbf{e}_N , $\mathbf{e}_3^{(0)}$ and \mathbf{e}_B are not necessarily the same. Because based on definition, $\mathbf{e}_2^{(0)}$ and $\mathbf{e}_3^{(0)}$ are defined by the shape of the beam cross section while \mathbf{e}_N and \mathbf{e}_B are defined by the axial curve shape as indicated in (2.4). These two frames are related by a pure rotation

$$\begin{Bmatrix} \mathbf{e}_T \\ \mathbf{e}_N \\ \mathbf{e}_B \end{Bmatrix} = [\mathbf{R}_\varphi^{(0)}] \begin{Bmatrix} \mathbf{e}_1^{(0)} \\ \mathbf{e}_2^{(0)} \\ \mathbf{e}_3^{(0)} \end{Bmatrix} \quad \text{where} \quad [\mathbf{R}_\varphi^{(0)}] = \begin{bmatrix} 1 & 0 & 0 \\ 0 & \cos \varphi^{(0)} & \sin \varphi^{(0)} \\ 0 & -\sin \varphi^{(0)} & \cos \varphi^{(0)} \end{bmatrix} \quad (2.9)$$

Assume $\varphi^{(0)}$ is constant and $\mathbf{e}_i^{(0)}$ coincide with \mathbf{E}_i ($i = 1, 2$ and 3) at the base ($s = 0$), then

$$\cos \varphi^{(0)} = \mathbf{E}_2 \cdot \mathbf{e}_N \Big|_{s=0}, \quad \sin \varphi^{(0)} = \mathbf{E}_3 \cdot \mathbf{e}_N \Big|_{s=0} \quad (2.10)$$

Differentiating (2.9) and combining with (2.5), one can arrive at

$$\frac{d}{ds} \begin{Bmatrix} \mathbf{e}_1^{(0)} \\ \mathbf{e}_2^{(0)} \\ \mathbf{e}_3^{(0)} \end{Bmatrix} = [\mathbf{R}_\varphi^{(0)}]^T \frac{d}{ds} \begin{Bmatrix} \mathbf{e}_T \\ \mathbf{e}_N \\ \mathbf{e}_B \end{Bmatrix} = [\mathbf{R}_\varphi^{(0)}]^T \begin{bmatrix} 0 & \kappa & 0 \\ -\kappa & 0 & \tau \\ 0 & -\tau & 0 \end{bmatrix} [\mathbf{R}_\varphi^{(0)}] \begin{Bmatrix} \mathbf{e}_1^{(0)} \\ \mathbf{e}_2^{(0)} \\ \mathbf{e}_3^{(0)} \end{Bmatrix}$$

Derived in Appendix A,

$$\frac{d}{ds} \begin{Bmatrix} \mathbf{e}_1^{(0)} \\ \mathbf{e}_2^{(0)} \\ \mathbf{e}_3^{(0)} \end{Bmatrix} = \text{skew}(\mathbf{K}^{(0)}) \begin{Bmatrix} \mathbf{e}_1^{(0)} \\ \mathbf{e}_2^{(0)} \\ \mathbf{e}_3^{(0)} \end{Bmatrix}$$

where

$$\text{skew}(\mathbf{K}^{(0)}) = \begin{bmatrix} 0 & k_3^{(0)} & -k_2^{(0)} \\ -k_3^{(0)} & 0 & k_1^{(0)} \\ k_2^{(0)} & -k_1^{(0)} & 0 \end{bmatrix}$$

Comparing the above relations, the components of the initial curvature $\mathbf{K}^{(0)}$ are given as:

$$k_1^{(0)} = \tau, \quad k_2^{(0)} = \kappa \sin \varphi^{(0)}, \quad k_3^{(0)} = \kappa \cos \varphi^{(0)} \quad (2.11)$$

Here, $\varphi^{(0)}$ is a constant while κ and τ are functions of s , which can be interpolated using polynomials.

2.3 Kinematics of a 3D Beam

Previous section presented the forward procedure to obtain initial curvature $\mathbf{K}^{(0)}$ from the initial curved beam shape, and this section will focus on the inverse process to obtain the nodal coordinate along beam axis from the calculated deformed curvature \mathbf{K} .

The deformed curve beam axis is given by

$$\mathbf{x} = x_i \mathbf{E}_i \quad (2.12)$$

where x_i ($i = 1, 2$ and 3) are the nodal coordinates. It is noted that differentiation of (2.12) will give the tangential direction

$$\frac{d\mathbf{x}}{ds} = \frac{dx_i \mathbf{E}_i}{ds} = \frac{dx_i}{ds} \mathbf{E}_i = (1 + \varepsilon) \mathbf{e}_1 = (1 + \varepsilon) R_{1i} \mathbf{E}_i$$

hence
$$\frac{dx_i}{ds} = (1 + \varepsilon) R_{1i} \quad (2.13)$$

where ε is the longitudinal strain to be discussed in Section 2.4. Recall that only the first row of \mathbf{R} is involved in the nodal coordinates along the beam axis; and angle φ determines the relative twisting of the beam cross section with respect to the axis. In other words, they completely determine the deformed beam shape, so it is the next task to find $[R_{11} \ R_{12} \ R_{13}]$ and φ from \mathbf{K} .

As derived in Appendix A, the moving frame along the beam axis satisfies

$$\frac{d}{ds} \mathbf{e}_i = skew(\mathbf{K})_{ij} \mathbf{e}_j \quad (2.14)$$

where

$$skew(\mathbf{K})_{ij} = \frac{dR_{ik}}{ds} R_{kj}^T \quad (2.15)$$

As discussed in Section 2.1, the deformed beam shape can be obtained once the rotational matrix $[\mathbf{R}]$ is determined. Referring to [13], \mathbf{R} can be completely determined by its first row of $[\mathbf{R}]_1 = [R_{11} \ R_{12} \ R_{13}]$ and twisting angle φ ,

$$\begin{aligned} \mathbf{R} &= \begin{bmatrix} R_{11} & R_{12} & R_{13} \\ R_{21} & R_{22} & R_{23} \\ R_{31} & R_{32} & R_{33} \end{bmatrix} \\ &= \begin{bmatrix} 1 & 0 & 0 \\ 0 & \cos \varphi & \sin \varphi \\ 0 & -\sin \varphi & \cos \varphi \end{bmatrix} \begin{bmatrix} R_{11} & R_{12} & R_{13} \\ -R_{12} & 1 - R_{12}^2 / (1 + R_{11}) & -R_{12}R_{13} / (1 + R_{11}) \\ -R_{13} & -R_{12}R_{13} / (1 + R_{11}) & 1 - R_{13}^2 / (1 + R_{11}) \end{bmatrix} \end{aligned} \quad (2.16)$$

then the task becomes to determine φ and $[R_{11} \ R_{12} \ R_{13}]$ from \mathbf{K} .

From (2.14), k_1 can be expressed as following:

$$k_1 = \mathbf{e}_3 \cdot \frac{d\mathbf{e}_2}{ds}$$

Substituting (2.1b), (2.14), (2.15) and (2.16), and also considering $R_{11}^2 + R_{12}^2 + R_{13}^2 = 1$, the above equation can be rewritten as

$$\frac{d\varphi}{ds} = k_1 - k_2 \frac{R_{12} \cos \varphi + R_{13} \sin \varphi}{1 + R_{11}} - k_3 \frac{R_{13} \cos \varphi - R_{12} \sin \varphi}{1 + R_{11}} \quad (2.17)$$

From (A.4) in Appendix A, the first row of \mathbf{R} is readily expressed as

$$\frac{dR_{1j}}{ds} = skew(\mathbf{K})_{1k} R_{kj} \quad (2.18)$$

Grouping (2.13), (2.17) and (2.18), the kinematics of a 3D beam is governed by

$$R'_{11} = k_3 R_{21} - k_2 R_{31} \quad (2.19a)$$

$$R'_{12} = k_3 R_{22} - k_2 R_{32} \quad (2.19b)$$

$$R'_{13} = k_3 R_{23} - k_2 R_{33} \quad (2.19c)$$

$$\varphi' = k_1 + k_2 \frac{R_{13}R_{32} - R_{12}R_{33}}{1 + R_{11}} + k_3 \frac{R_{12}R_{23} - R_{13}R_{22}}{1 + R_{11}} \quad (2.19d)$$

$$x'_1 = (1 + \varepsilon)R_{11} \quad (2.19e)$$

$$x'_2 = (1 + \varepsilon)R_{12} \quad (2.19f)$$

$$x'_3 = (1 + \varepsilon)R_{13} \quad (2.19g)$$

where ' denotes derivative with respect to path length s .

Now that the formulation is partially complete, it is best illustrated with numerical examples loading free conditions to verify the kinematic analysis. So, the curvature should not change and the longitudinal strain is zero, or

$$\mathbf{K} = \mathbf{K}^{(0)} \text{ and } \varepsilon = 0$$

The following procedure will be adopted.

- 1) Given a parametric relation (2.3) of a beam axial curve, determine the curvature (2.11) as a function of the path length.
- 2) Reconstruct the original beam shape $\mathbf{x}^{(0)}$ by numerically solving the IVP of (2.19) with initial conditions at $s = 0$:

$$R_{11} = 1, R_{12} = R_{13} = 0; \varphi = 0; x_1 = x_2 = x_3 = 0$$

- 3) Compare the calculated curve shape \mathbf{x} with the original shape $\mathbf{x}^{(0)}$.

Three examples are chosen to illustrate the curvature description of a beam geometry. The first example is a planar curved beam with non-constant curvature κ and zero torsion τ . The next example illustrates the case of constant κ and τ using a helix curved beam, where the principal axes are not aligned with the global reference frame at

the base. The final example shows the case of non-constant κ and τ with a general 3-D curved beam.

Example 2.3.1 Planar Curved Beam:

Consider a curved beam on the XY plane with the axial curve described as

$$x_1^{(0)} = 10 \sin t, \quad x_2^{(0)} = 5 - 5 \cos t, \quad x_3^{(0)} = 0$$

For $t \in [0 \quad 2\pi]$, the overall curve length given by (2.7) is $L = 48.44$.

As shown in Figure 2.5(a), for a planar curve, there is only one non-zero component of curvature, κ . Given the highly nonlinear relation between κ and path length s , a polynomial is used for approximation. Percentage errors for the approximated curvature and the reconstructed beam shape \mathbf{x} are calculated as

$$e_\kappa = \frac{\max |\kappa - \kappa_{approx.}|}{\kappa} \times 100\%$$

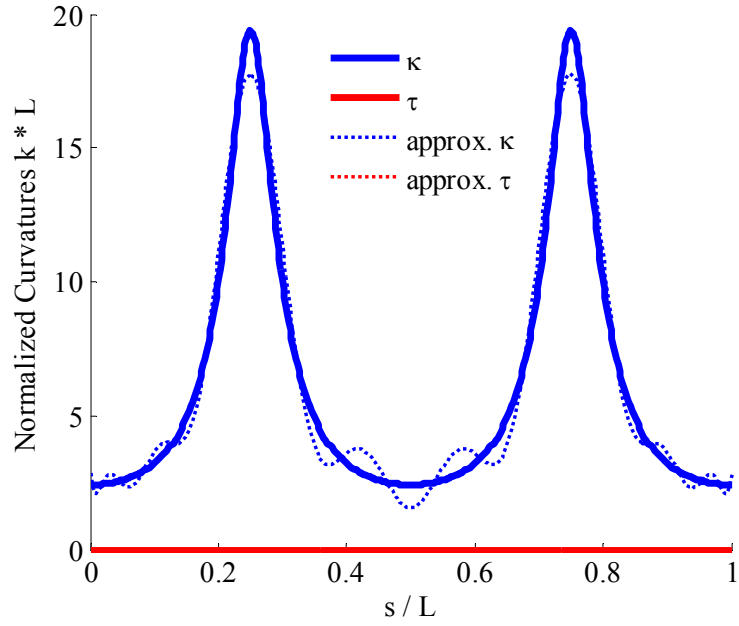
$$e_{beam} = \frac{|\mathbf{x} - \mathbf{x}^{(0)}|_{s=L}}{L} \times 100\%$$

Because the calculation error accumulates through the integration, it is expected that the reconstructed beam shape has maximum error at the end $s = L$. In this example, $e_\kappa = 8.38\%$ and $e_{beam} = 0.025\%$. Even though there is obvious deviation between the polynomial approximation and the actual value of κ , the elliptic shape can still be reconstructed as shown in Figure 2.5(b).

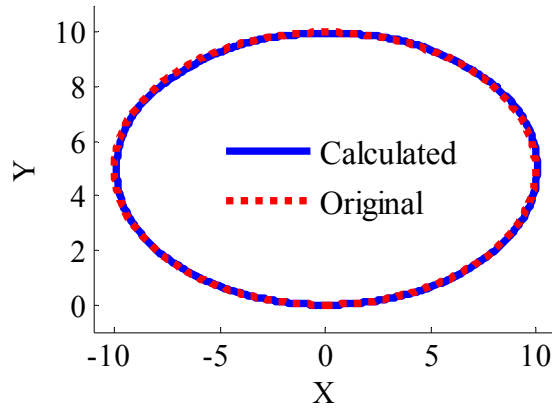
Example 2.3.2 A Helix Curved Beam:

For a helix curve with radius of r and pitch of $2\pi p$, its parametric expression can be written as

$$x = r \sin t, \quad y = r - r \cos t, \quad z = pt$$



(a) Curvatures.



(b) Comparison of the original and calculated curves.

Figure 2.5 Verification with a planar curve (non-constant curvature).

In order to orient the global reference frame to the Frenet-Serret frame at the helix base, it requires a rigid body rotation

$$\begin{Bmatrix} x_1^{(0)} \\ x_2^{(0)} \\ x_3^{(0)} \end{Bmatrix} = \begin{bmatrix} \cos \beta & 0 & \sin \beta \\ 0 & 1 & 0 \\ -\sin \beta & 0 & \cos \beta \end{bmatrix} \begin{Bmatrix} x \\ y \\ z \end{Bmatrix} \quad \text{where } \beta = \tan^{-1} \frac{p}{r}$$

Employing (2.8), it can be obtained that

$$\kappa = \frac{r}{r^2 + p^2} \quad \text{and} \quad \tau = \frac{p}{r^2 + p^2}$$

When $r = 7.239\text{mm}$ and $p = 5.715\text{mm}$, the curvatures are calculated as $\kappa = 0.0851\text{mm}^{-1}$ and $\tau = 0.0672\text{mm}^{-1}$. Figure 2.6 shows the simulated result of the helix curve with 10 pitches ($t \in [0 \quad 20\pi]$) and the percentage error $e_{\text{beam}} = 2.83\%$.

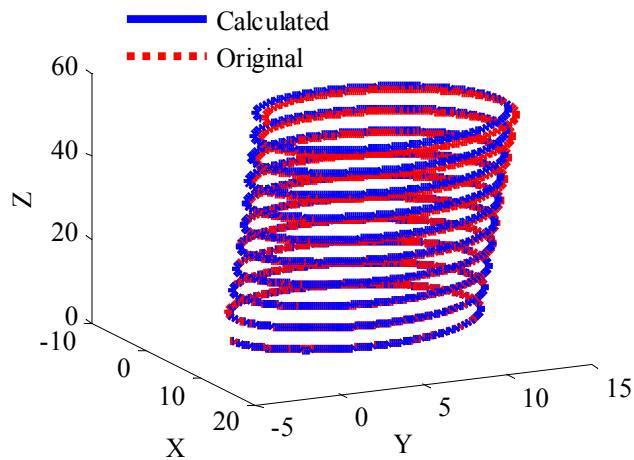


Figure 2.6 Verification with a helix curve (constant curvature).

Example 2.3.3 A 3-D Curved Beam:

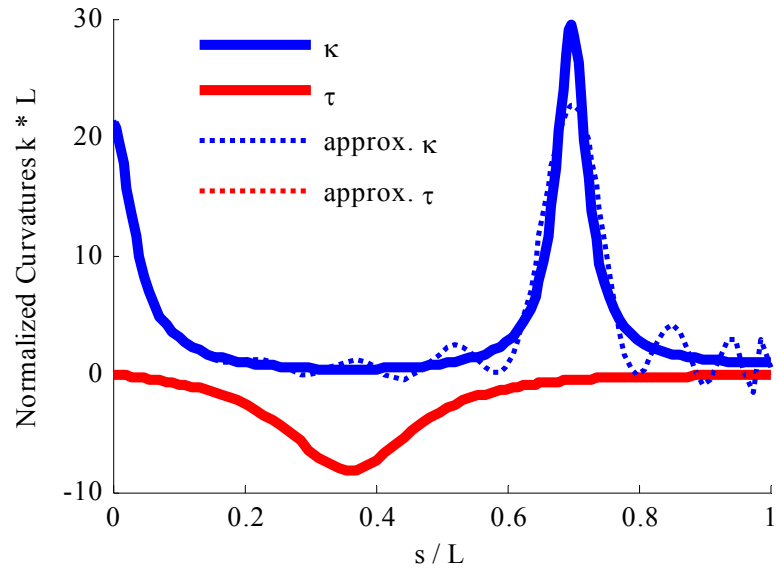
The last example is given by

$$x_1^{(0)} = 25 \sin t, \quad x_2^{(0)} = 10 - 10 \cos 2t, \quad x_3^{(0)} = 20 - 20 \cos 3t$$

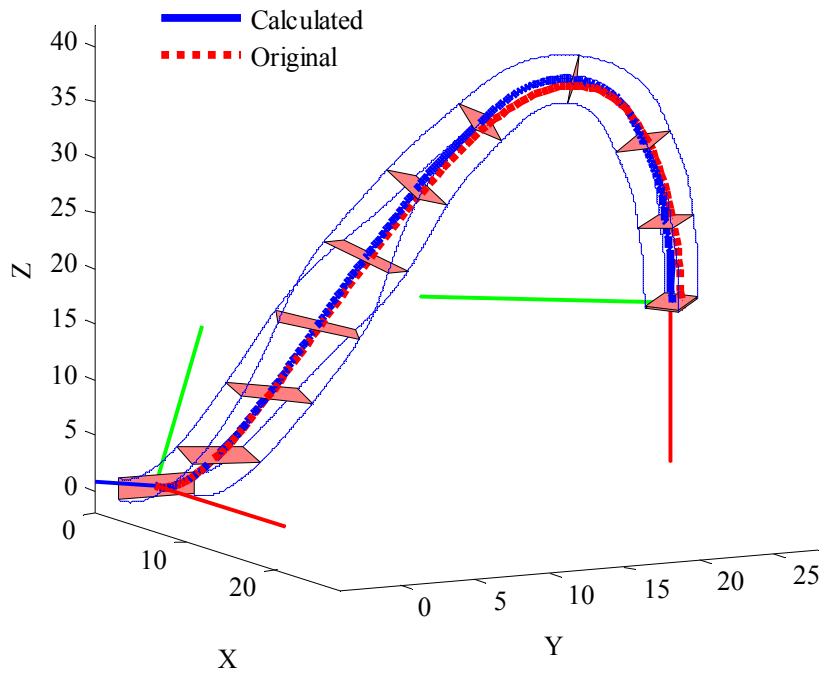
For $t \in [0 \quad \pi/2]$, the overall curve length given by (2.7) is $L = 71.973$.

For illustration, the beam cross-section aspect ratio is set to be 5:2 and its snapshots are shown along the longitudinal axis. As shown in Figure 2.7(a), both κ and τ are nonlinear functions of s . Although the error e_{κ} in the curvature approximation is as large as 23.22%, the error in the calculated beam shape is obtained as $e_{\text{beam}} = 0.71\%$. In Figure 2.7(b), the Frenet-Serret frame is also shown at the base and tip of the curved beam, with

red denoting the tangent \mathbf{e}_T , green denoting the normal \mathbf{e}_N and blue denoting the binormal \mathbf{e}_B . From (2.4), \mathbf{e}_N and \mathbf{e}_B can be obtained as following:



(a) Curvatures.



(b) Comparison of the original and calculated curves.

Figure 2.7 Verification with a 3-D curve with non-constant curvatures.

$$\mathbf{e}_N = [0 \quad 0.2169 \quad 0.9762]^T, \quad \mathbf{e}_B = [0 \quad -0.9762 \quad 0.2169]$$

So they do not necessarily coincide with the cross section principal axes $\mathbf{e}_2^{(0)}$ and $\mathbf{e}_3^{(0)}$.

The components of the elastic curvature $\mathbf{K}^{(e)} = [k_1^{(e)} \quad k_2^{(e)} \quad k_3^{(e)}]^T$ due to external loadings can be calculated as

$$k_i^{(e)} = \frac{\mathbf{M} \cdot \mathbf{e}_i}{(EI)} = \frac{M_k \mathbf{E}_k \cdot R_{ij} \mathbf{E}_j}{(EI)} = \frac{M_j R_{ij}}{(EI)} \quad (2.20)$$

where $k_1^{(e)}$ is the twisting curvature; and $k_2^{(e)}$ and $k_3^{(e)}$ are the bending curvatures; $(EI) = GI_1$ for $i = 1$, $(EI) = EI_i$ for $i = 2$ and 3 ; E is the Young's modulus; G is the shear modulus; and I_i ($i = 1, 2$ and 3) is the moment of inertia. Then, the longitudinal strain ε is given by (2.21) with A denoting the cross section area

$$\varepsilon = \frac{\mathbf{F} \cdot \mathbf{e}_1}{EA} = \frac{F_i \mathbf{E}_i \cdot R_{1j} \mathbf{E}_j}{EA} = \frac{F_i R_{1i}}{EA} \quad (2.21)$$

Based on the static analysis of the beam segment, the equations for the force and moment equilibrium are given by

$$\begin{aligned} -\mathbf{F} + (\mathbf{F} + \Delta\mathbf{F}) + \int_s^{s+\Delta s} \mathbf{q}_F d\rho &= 0 \\ -\mathbf{M} + (\mathbf{M} + \Delta\mathbf{M}) + \int_s^{s+\Delta s} \mathbf{q}_M d\rho \\ + [\mathbf{e}_1(1+e)\Delta s] \times (\mathbf{F} + \Delta\mathbf{F}) + \int_s^{s+\Delta s} [\mathbf{e}_1(\rho-s)] \times \mathbf{q}_F d\rho &= 0 \end{aligned}$$

where $\Delta\mathbf{R} = \text{skew}(\mathbf{K})\Delta s$. In the above moment equilibrium equations, all the moment terms are written out with respect to point Q_s in Figure 2.8.

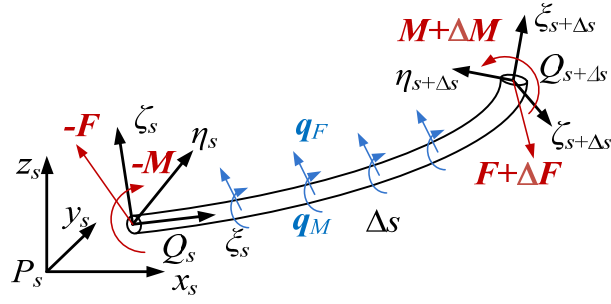


Figure 2.8 Equilibrium of a beam segment.

For an infinitesimally small Δs and neglecting the higher order terms, the above can be rewritten as

$$\frac{d\mathbf{F}}{ds} = -\mathbf{q}_F \quad (2.22)$$

$$\frac{d\mathbf{M}}{ds} = -\mathbf{q}_M - [(1 + \varepsilon)\mathbf{e}_1] \times \mathbf{F} \quad (2.23)$$

Grouping (2.19), (2.22) and (2.23), the governing equations of a 3-D beam are

$$R'_{11} = k_3 R_{21} - k_2 R_{31} \quad (2.24a)$$

$$R'_{12} = k_3 R_{22} - k_2 R_{32} \quad (2.24b)$$

$$R'_{13} = k_3 R_{23} - k_2 R_{33} \quad (2.24c)$$

$$\varphi' = k_1 + k_2 \frac{R_{13}R_{32} - R_{12}R_{33}}{1 + R_{11}} + k_3 \frac{R_{12}R_{23} - R_{13}R_{22}}{1 + R_{11}} \quad (2.24d)$$

$$x'_1 = (1 + \varepsilon)R_{11} \quad (2.24e)$$

$$x'_2 = (1 + \varepsilon)R_{12} \quad (2.24f)$$

$$x'_3 = (1 + \varepsilon)R_{13} \quad (2.24g)$$

$$F'_1 = -q_{F1} \quad (2.24h)$$

$$F'_2 = -q_{F2} \quad (2.24i)$$

$$F'_3 = -q_{F3} \quad (2.24j)$$

$$M'_1 = -q_{M1} - (1 + \varepsilon)(R_{12}F_3 - R_{13}F_2) \quad (2.24k)$$

$$M'_2 = -q_{M2} - (1 + \varepsilon)(R_{13}F_1 - R_{11}F_3) \quad (2.24l)$$

$$M'_3 = -q_{M3} - (1 + \varepsilon)(R_{11}F_2 - R_{12}F_1) \quad (2.24m)$$

where ε and $\mathbf{K} = [k_1 \ k_2 \ k_3]^T$ are given by

$$\varepsilon = \frac{1}{EA}(F_1R_{11} + F_2R_{12} + F_3R_{13}) \quad (2.25a)$$

$$k_1 = k_1^{(0)} + \frac{1}{GI_1}(M_1R_{11} + M_2R_{12} + M_3R_{13}) \quad (2.25b)$$

$$k_2 = k_2^{(0)} + \frac{1}{EI_2}(M_1R_{21} + M_2R_{22} + M_3R_{23}) \quad (2.25c)$$

$$k_3 = k_3^{(0)} + \frac{1}{GI_3}(M_1R_{31} + M_2R_{32} + M_3R_{33}) \quad (2.25d)$$

The boundary value problem (BVP) of the compliant beam can be written compactly in the following form:

$$\mathbf{X}' = \mathbf{f}(s, \mathbf{X}), \quad \mathbf{g}(\mathbf{X}(0), \mathbf{X}(L)) = \mathbf{0} \quad (2.26)$$

where \mathbf{X} is a vector of the 13 variables $[x_1 \ x_2 \ x_3 \ R_{11} \ R_{12} \ R_{13} \ \varphi \ F_1 \ F_2 \ F_3 \ M_1 \ M_2 \ M_3]^T$; $0 \leq s \leq L$; and $\mathbf{g}(\bullet)$ is the boundary conditions specifying the geometrical and/or loading constraints at both ends. The BVP (2.26) can be solved using an MSM [34, 35] given in Appendix B, which recasts the BVP into an IVP. In the following, two illustrative examples of a compressive spring and a twisted ring are presented under boundary conditions of cantilever constraint. The first considers a forward problem in which a compressive axial force is applied on the spring to obtain its deformed shape. The second

illustrates an inverse problem, where the input rotational angle is specified on an elliptical ring to solve for the output torque.

Example 2.4.1 A Compressive Spring:

In this example, the compressive spring is modeled as a helix curved beam with circular cross-section. Its initial curvature has been studied in Example 2.3.2 but the case is now considered under axial compression. Table 2.1 lists the spring specifications in terms of its dimensions and material properties. The boundary conditions show that one end of the spring is completely fixed while the other end is completely free and subjected to axial compression. As shown in Figure 2.9, instability can occur for spring under axial compression, and the CBM produces close result ($e_{\text{beam}} = 3.96\%$) with FE method.

Table 2.1 Spring specification and boundary conditions.

Dimension		Material properties	
Radius (mm)	7.239	Elastic modulus (GPa)	193
Pitch (mm)	5.715	Shear modulus (GPa)	80.8
Cross section radius (mm)	0.6985	Poisson ratio	0.25
Boundary conditions			
$s = 0$	$x_1 = 0, x_2 = 0, x_3 = 0, R_{11} = 1, R_{12} = 0, R_{13} = 0, \varphi = 0;$		
$s = L$	$F_1 = 0, F_2 = 0, F_3 = F, M_1 = 0, M_2 = 0, M_3 = 0.$		

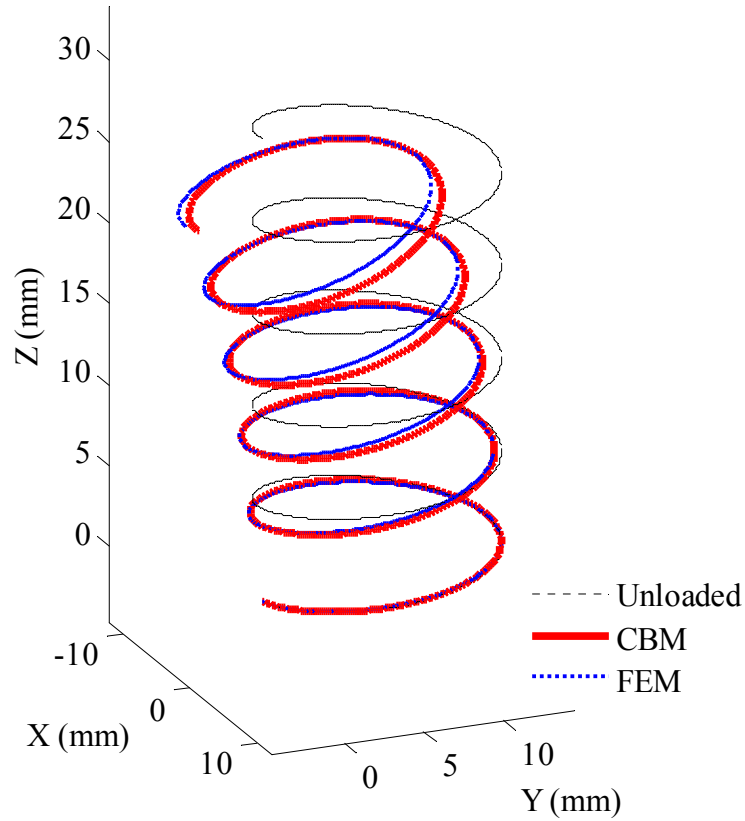


Figure 2.9 Lateral deflection under axial compression.

Example 2.4.2 A Twisted Ring:

The half-circle twisting-ring has been chosen for illustration because it has a number of applications in mechatronics. Table 2.2 shows a compliant half-ring mechanism with both ends pinned and twisted by an angle θ . Numerical values of the characteristic parameters for the four materials are compared in Table 2.2. For design purposes, the results are presented in non-dimensional forms; the following normalization rules are applied to the beam equations (2.24):

$$F_i = \tilde{F}_i \frac{EI_2}{r^2}, \quad M_i = \tilde{M}_i \frac{EI_2}{r}, \quad q_{Fi} = \tilde{q}_{Fi} \frac{EI_2}{r^3}, \quad q_{Mi} = \tilde{q}_{Mi} \frac{EI_2}{r^2},$$

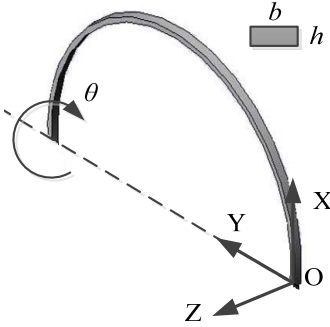
$$k_i^{(0)} = \tilde{k}_i^{(0)} \frac{1}{r}, \quad \kappa_i = \tilde{\kappa}_i \frac{1}{r}, \quad \text{and} \quad x_i = \tilde{x}_i r$$

where r is radius of the ring.

The deformed shape of the compliant ring ($b/h = 2$) subject to a pure twisting of $\theta = \pi/4$ at both ends is shown in Figure 2.10. The effects of aspect ratios ($b/h = 2, 3, 6$), and four different materials (steel, titanium, aluminum and delrin) on the (normalized) twisting moment M_2 in direction along Y axis at the ends are compared in Figure 2.11. As shown in Figure 2.11, the effect of different materials is relatively insensitive on the normalized twisting moment M_2 at the ends. However, different normalized M_2 curves are needed for different aspect ratios (b/h).

Table 2.2 Ring specification and boundary conditions.

Parameters	Steel	Titanium	Aluminum	Delrin
E (GPa)	193	116	70	3.1
Poisson ratio	0.25	0.34	0.3	0.35
Density(10^3kg/m^3)	7.85	4.54	2.7	1.42



$b/h = 2; \theta = \pi/4$

$s/r = 0,$
 $R_{11} = \cos \theta, R_{12} = \sin \theta, R_{13} = 0$
 $x_1 = x_2 = x_3 = \varphi = 0$

 $s/r = \pi,$
 $R_{12} = \sin \theta, R_{13} = 0$
 $x_1 = 0, x_3 = 0, \varphi = 0$

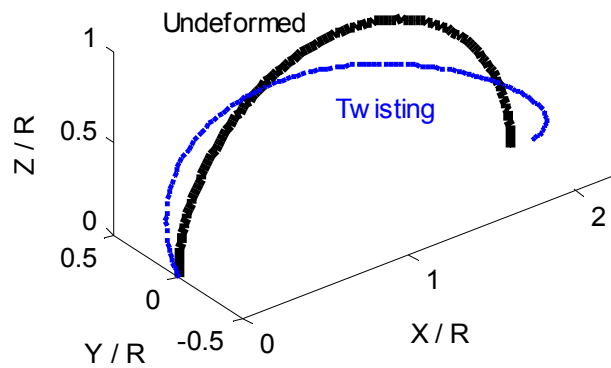


Figure 2.10 Normalized deformed shape of the twisted ring.

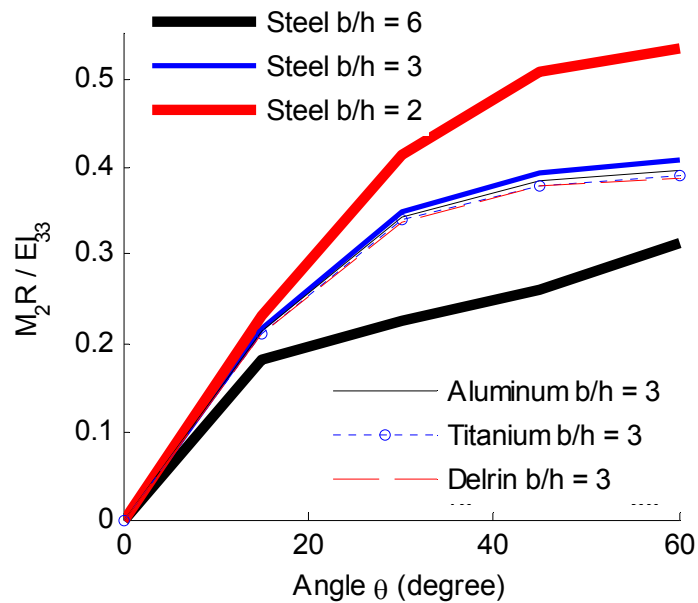


Figure 2.11 Effect of aspect ratios and materials.

2.4 Summary

A Curvature-based Beam Model (CBM) has been formulated for the large deformation problem of a 3-D compliant beam. Relation between the curvature and absolute nodal coordinate of a curved beam is derived. It has shown that curvature is a

key characteristic of curved beam geometry. This CBM has fully explored the advantages of curvature description by formulating all state variables of a curved 3-D beam in the global reference frame. The CBM is verified by the FEM through the large deformation analysis of 3-D curved beams under cantilever constraints. Generalized boundary constraints will be formulated in Chapter III, and two specific applications will be presented to illustrate how the CBM (with general constraints) is implemented for engineering purposes in Chapter IV and V.

CHAPTER III

GENERALIZED CONSTRAINT

This chapter presents a generalized constraint by relaxing common assumptions in traditional boundary constraints such as fixed, pinned or sliding constraint on compliant mechanisms, where none or only one DOF is allowed. Motivated by the multi-axis rotation within a natural biological joint, this chapter defines a generalized constraint referred to here as bio-joint constraint (BJC) on compliant mechanism for emulating motions of multi-DOF.

In a multi-body system, a compliant beam can be regarded to move with a rigid body as shown in Figure 2.2. The BJC can then be formulated as a contact constraint between two rigid bodies; without loss of generality, they are approximated locally as two ellipsoids in the following discussions. This constraint can be used for kinematic or dynamic analysis based on the curvature description presented in Chapter II.

The remainder of this chapter begins with the kinematic formulation of the BJC and related algorithm in Section 3.1, and the method is validated with published experiment data on human knee joint. Then, the dynamic analysis is provided in Section 3.2 to illustrate that how a multi-body system compliance is designed. Finally, Section 3.3 shows how this BJC is incorporated as boundary conditions into the BVP of compliant mechanisms.

3.1 Formulation of Kinematics

Consider two bodies, Ω_A and Ω_B , bound by boundaries Γ_A and Γ_B respectively. As shown in Figure 3.1, Ω_A rolls on Ω_B ; and C is an instantaneous contact point satisfying (3.1a,b):

$$\mathbf{P}_A(\mathbf{x}_c) = \mathbf{P}_B(\mathbf{x}_c) \text{ and } \mathbf{P}'_A(\mathbf{x}_c) = \mathbf{P}'_B(\mathbf{x}_c) \quad (3.1a,b)$$

where $\mathbf{P}_A(\mathbf{x})$ and $\mathbf{P}_B(\mathbf{x})$ describe the contact points on Ω_A and Ω_B in terms of a position vector \mathbf{x} in the world frame; and $\mathbf{P}'_A(\mathbf{x})$ and $\mathbf{P}'_B(\mathbf{x})$ are their derivatives with respect to \mathbf{x} ; and the subscript “c” denotes the contact point C . It is worth noting that common engineering joints and mechanical cams are special cases of the biological joint illustrated in Figure 3.1.

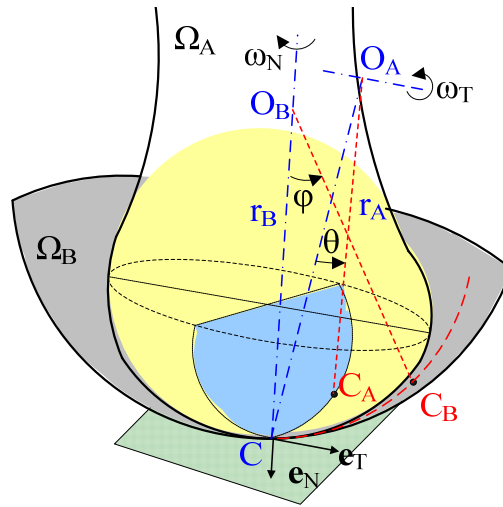


Figure 3.1 Bio-joint constraint.

Given C on Γ_A , there always exists a tangential plane with a normal vector \mathbf{e}_N such that the angular velocity $\boldsymbol{\omega}$ describes the motion of Ω_A at C :

$$\boldsymbol{\omega} = \omega_N \mathbf{e}_N + \omega_T \mathbf{e}_T \quad (3.2)$$

where \mathbf{e}_T is a unit vector on the tangential plane. We define an osculating plane (indicated in blue in Figure 3.1) perpendicular to ω_T at C. The contact point on Γ_A and Γ_B moves incrementally from C_A and C_B to C along the respective osculating circles as shown in Figure 3.1, where (O_A, ρ_A) and (O_B, ρ_B) are the centers and radii of the osculating circles intersecting at Γ_A and Γ_B respectively; and θ and φ are the angles describing the corresponding displacements of the contact points on Ω_A and Ω_B respectively. The 3-D motion of a biological joint can be characterized in the instantaneous osculating plane that depends on the location of the contact point (and hence is a function of time).

The contact point displacement of Ω_A is

$$ds = \sqrt{(ds_N)^2 + (ds_T)^2} = ds_T \sqrt{1 + (\omega_N dt)^2} \approx ds_T \quad (3.3)$$

where $ds_T = \rho_A \omega_T dt$ and $ds_N = ds_T \omega_N dt$ are in the \mathbf{e}_T and \mathbf{e}_N directions, when neglecting the higher order infinitesimal time interval dt^2 . Without loss of generality, the effect of ω_N (that may be nonzero) on the contact point displacement s is neglected; $\omega_T = \omega$ is assumed for simplicity of analyzing the biological kinematics in the following discussions. The 3D kinematics of a biological joint is reduced to finding the contact location in the osculating circular motion and the position and orientation of Ω_A . In addition, the boundaries (Γ_A and Γ_B) are assumed known with respect to their own local coordinate frames. In polar coordinates, a smooth 2D curve on the boundary is denoted as

$$\mathbf{P}[\mathbf{x}(\psi)] = \mathbf{P}[x(\psi), y(\psi)] = x(\psi)\mathbf{E}_1 + y(\psi)\mathbf{E}_2 \quad (3.4)$$

where ψ is an angle with respect to a reference body axis. The tangential and normal directions at \mathbf{x} on the curve are

$$\mathbf{e}_T = \mathbf{P}' = \frac{dx}{d\psi} \mathbf{E}_1 + \frac{dy}{d\psi} \mathbf{E}_2; \text{ and } \mathbf{e}_N = -\frac{dy}{d\psi} \mathbf{E}_1 + \frac{dx}{d\psi} \mathbf{E}_2 \quad (3.5a,b)$$

We can always find an osculating circle with a radius [61]:

$$r = \frac{|\mathbf{P}'|^3}{|\mathbf{P}' \times \mathbf{P}''|} \quad (3.6)$$

For a sliding contact, there is a relative velocity v_r between Ω_A and Ω_B ,

$$r_A \omega_r = r_B (d\varphi / dt) + v_r \text{ where } \omega_r = d\theta / dt. \quad (3.7)$$

The lengths of CC_A and CC_B , in polar coordinates, are respectively given by (3.8a) and (3.8b), where “ \sim ” refers to the value of the dummy variable in the curve equation:

$$s + \int_0^{t_c} v_r dt = \int_0^{t_c} r_A \omega_r dt = \int_{\tilde{\theta}_0}^{\tilde{\theta}_c} |\mathbf{P}'_A [x(\psi), y(\psi)]| d\psi \quad (3.8a)$$

$$s = \int_0^{t_c} r_B \dot{\phi} dt = \int_{\tilde{\phi}_0}^{\tilde{\phi}_c} |\mathbf{P}'_B [x(\psi), y(\psi)]| d\psi \quad (3.8b)$$

It is worth noting that for the case of a non-slip rolling, $v_r = 0$; thus, from (3.8) the curve lengths, CC_A and CC_B , along their respective osculating circles are equal. Unlike a cylindrical or spherical (engineering) joint which is free to spin about its own axis, bio joints generally have very limited spinning freedom about its own axis as the contact pair of a bio joint is typically connected by ligaments and tendons. In the following discussions, we focus on the orientation of two degrees-of-freedom inclination.

3.1.1 Algorithm

The contact point and the position/orientation of Ω_A can be found using the steps summarized in Table 3.1:

Table 3.1 Algorithm for bio-joint kinematics.

1)	Determine the initial contact position between Ω_A and Ω_B , i.e. $\tilde{\theta}_0$ and $\tilde{\varphi}_0$ in their own local frame
2)	Calculate the increment of s from $r_A(\psi)\omega\Delta t$ (Δt is the time step, for the first step $\psi = \tilde{\theta}_0$).
3)	Find the contact point C on Ω_A by solving
	$s = \int_{\tilde{\theta}_0}^{\tilde{\theta}_c} d\mathbf{P}_A / d\psi d\psi \quad (3.9)$
4)	To find C at $t = n\Delta t$ on Ω_A , repeat step 2 and 3 by updating $r_A(\psi)$.
5)	Determine C on Ω_B by solving (3.8b) for $\tilde{\varphi}_c$.
6)	Use (3.8) to determine the position/orientation of Ω_A .

There are three examples, on-sliding and sliding contacts between two ellipses, provide intuitive insights into the contact kinematics of a typical biological joint. The dimensions used in these examples are summarized in Table 3.2, where a_i and b_i are the major and minor radii of the ellipses. Although we employ ellipses for illustration, this model can be used to analyze contact kinematics of non-uniform shapes because the

formulation, (3.1) to (3.8), requires only local geometric properties rather than the whole geometry.

Table 3.2 Simulation parameter values.

$\omega = \pi / 12$	Ω_A		Ω_B	
rad/s	b_1/a_1	a_1 (cm)	b_2/a_2	a_2 (cm)
Dimensions	0.5	2	1	1

Example 3.1.1 Contact between Ellipses

Figure 3.2 shows three snapshots of the ellipse Ω_A rolling on the (fixed) circle Ω_B , where the solid black ellipse and circle are the contact pair at the initial position ($\tilde{\theta}_0=0$). The two consecutive snapshots are graphed in red and blue colors respectively. In Fig. 3, the green circles mark the initial contact point on Ω_A ; the blue asterisks indicate the current point C; and the dashed circles are the osculating circles at the two respective instants. As shown in Figure 3.2, the normal vector \mathbf{e}_N (and thus ω_T and its direction) of the ellipse Ω_A changes with the contact point.

The computation procedure given in Table 3.1 can be illustrated as follows:

- 1) As derived in (3.6), the osculating circle is a function of geometry. The effect of Ω_A shape on the radius ρ_A is graphed as a function of ψ (or the local angle measured from the major axis characterizing the point on Ω_A) in Figure 3.2. Unlike a circle ($b/a=1$), different points on the ellipse Ω_A have different sizes of osculating circles.

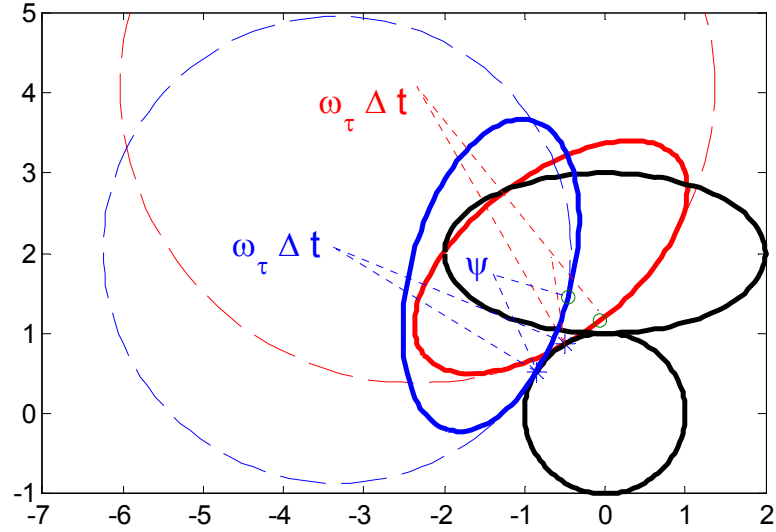


Figure 3.2 Snapshots illustrating the formulation.

- 2) At $t = \Delta t$ (=1 second), Ω_A (red) rotates by $\omega\Delta t$ with $r_A(0)$, and thus the distance increment $\Delta s = r_A(0)\omega\Delta t$. Then, the contact point on Ω_A can be found by calculating $\psi(=\Delta\psi)$ from (3.9):

$$\Delta s = \int_0^{\Delta\psi} \left| \frac{d\mathbf{P}_A}{d\psi} \right| d\psi .$$

- 3) Similarly, at $t = 2\Delta t$ (=2 seconds), Ω_A (blue) rotates an additional $\omega\Delta t$ from previous contact point with $\rho_A(\Delta\psi)$, and thus the next $\Delta s = \rho_A(\Delta\psi)\omega\Delta t$ and ψ can be obtained again from (3.9) with the lower bound of the integration being $\Delta\psi$.
- 4) The computed distance s is given in Figure 3.4 for different b/a ratios of Ω_A . In Figure 3.4, $\psi = 0$ corresponds to the orientation when the major axis of Ω_A is horizontal as shown in Figure 3.2. For circle, s increases linearly because r_A is a constant, while for the elliptic, s increases nonlinearly with r_A .

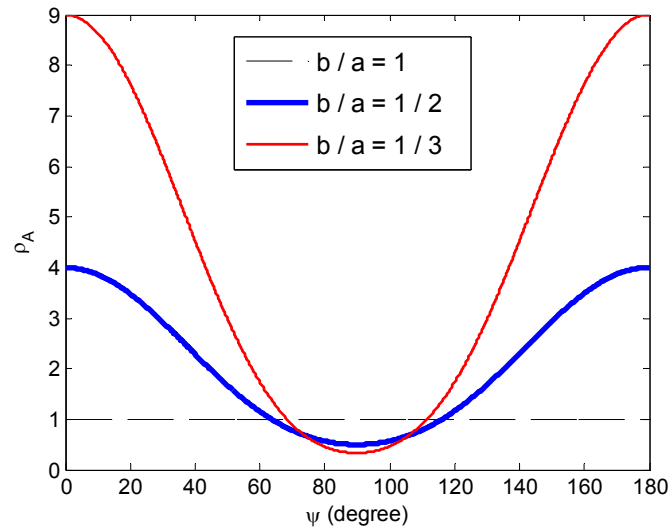


Figure 3.3 Effect of shapes on the osculating circle.

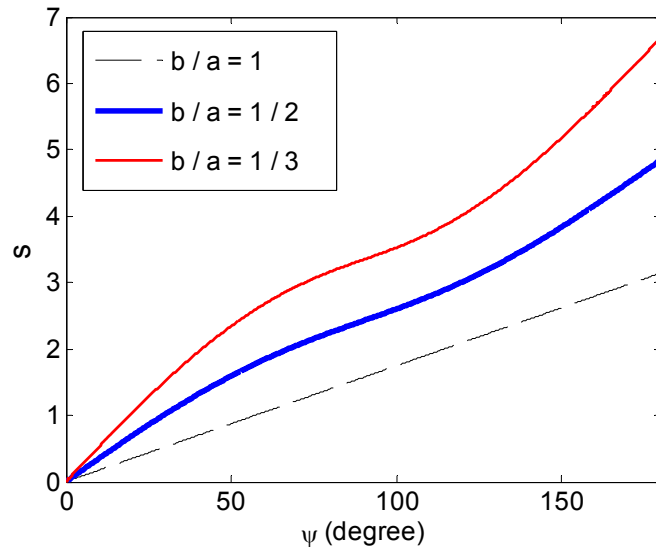


Figure 3.4 Ellipse – cylinder contact.

Because of no slippage, the contact point moves at the same distance on Ω_A and Ω_B . From (3.8b), $\tilde{\varphi}_c$ can be solved. Note that $\tilde{\theta}_c$ and $\tilde{\varphi}_c$ are in different local coordinate frames, which must be represented in the same world frame using (3.1) to obtain the position and orientation of Ω_A .

Example 3.1.2 Effect of Sliding on Contact Kinematics

The effect of sliding can be explained using (3.8a). Note that when $v_r = \omega r_A$, $s = 0$; the contact becomes pure sliding. As shown in Figure 3.3, $\min(r_A)$ occurs at $\psi = 90^\circ$. For simplicity, we choose for this illustrative example $v_r = \omega \cdot \min(r_A) = 0.1309\text{mm/s}$ so that the contact becomes pure sliding at the contact points that have the minimal rotation radius. The results simulating the effect of sliding on the same contact pair in Figure 3.2 (thick solid black ellipse and circle) are given in Figure 3.5 and Figure 3.6.

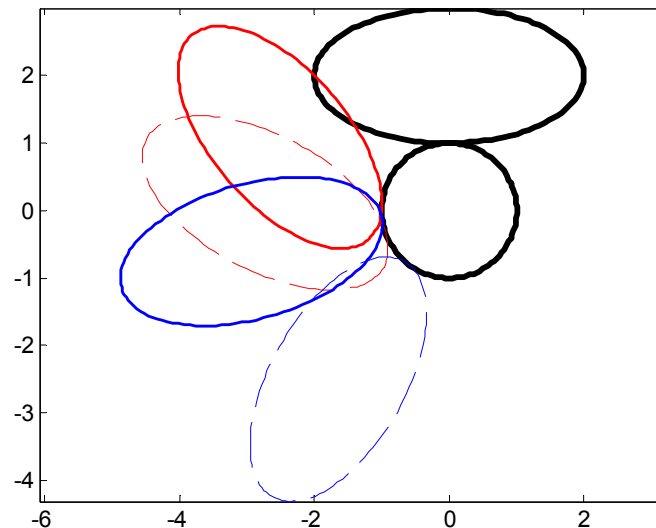


Figure 3.5 Effect of sliding on contact kinematics.

Figure 3.5 compares the two consecutive snapshots with sliding contact (thin-line ellipses) against those obtained without slippage (dash-line ellipses). In Figure 3.5, ellipses of the same color appear at the same instance: black ($t = 0$), red ($t = \Delta t = 1$ s) and blue ($t = 2\Delta t = 2$ s). As compared in Figure 3.5, rolling without slippage moves more than sliding contact as expected.

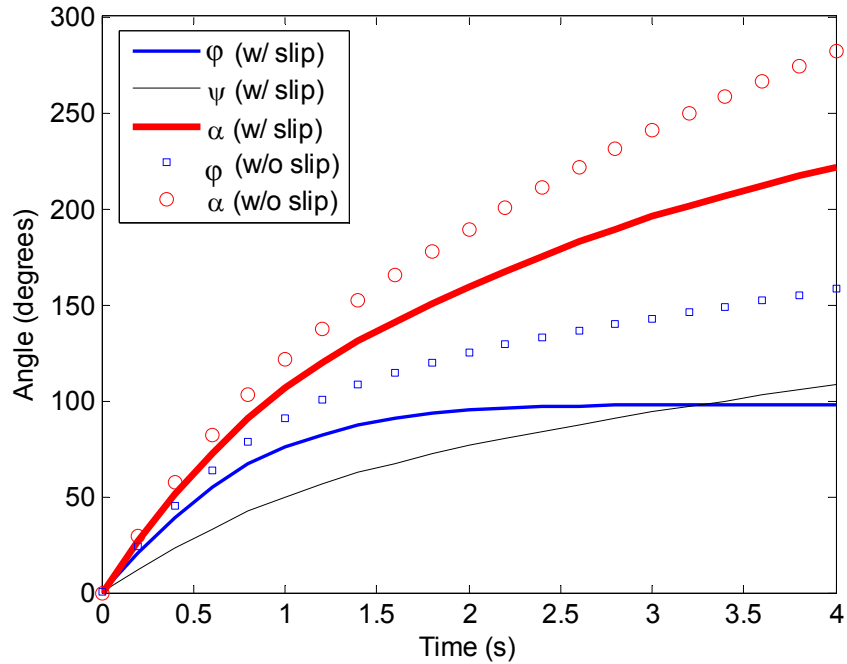


Figure 3.6 Effect of sliding on orientation.

Figure 3.6 compares the angular displacement φ and the orientation α of the elliptical Ω_A rolling on the circular Ω_B with and without slippage. The non-slip rolling has a larger φ and α . In Figure 3.6, the angle ψ is only a geometrical function of Ω_A , and is independent of the contact conditions. The φ and ψ curves intersect at $\varphi = \psi = 90^\circ$ for rolling with $v_r = \omega \min(r_A)$. In other words, this instantaneous contact point does not move (and stay at the same position on Ω_B no matter how fast Ω_A rotates). This result can be explained with the aid of (3.8a) and Figure 3.3 showing $s = 0$ when $v_r = \omega r_A$ and $\min(r_A)$ at $\psi = 90^\circ$ respectively.

Example 3.1.3 Contact between Convex / Concave Ellipses

As an illustration, the orientation (or the rotation angle of the minor axis) of Ω_A and the distance between the two centroids for the four cases are computed and the results are compared in Figure 3.7 and Figure 3.8. The values used in the simulation are

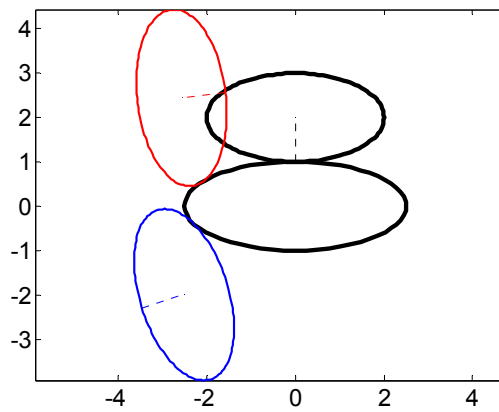
summarized in Table 3.3, where a_i and b_i are the major and minor radii of the ellipses. Some observations highlighting the differences between the commonly seen engineering joints, Cases 2(a) and 2(b), and the more general bio joints, Cases 1(a) and 1(b), can be summarized as follows:

- 1) The orientation of Ω_A changes nonlinearly for the cases of elliptical contact and linearly for those of circular contact. In addition, the inclination range of a bio joint depends on the aspect ratio b_i/a_i .
- 2) Unlike a concentric (cylindrical or ball-socket) joint that has negligible clearance between the contacting elements, an elliptical convex-concave contact of a bio joint could have a limited range of orientation movement.
- 3) As compared in Figure 3.8(a), the orientation of an elliptical convex-convex joint may be approximated by a circular convex-convex joint within a limited range. The validity of the orientation approximation depends on the specific aspect ratios b_i/a_i of the contact pair; see for example, Fig. 10 where the circular convex-convex approximation does not work.
- 4) Unlike the circular convex-convex joint where the center of Ω_A remains a constant distance from that of Ω_B as shown in Case 2(a) and 2(b) in Figure 3.7 and Figure 3.8(b), the center of Ω_A changes nonlinearly for the cases of an elliptical joint.

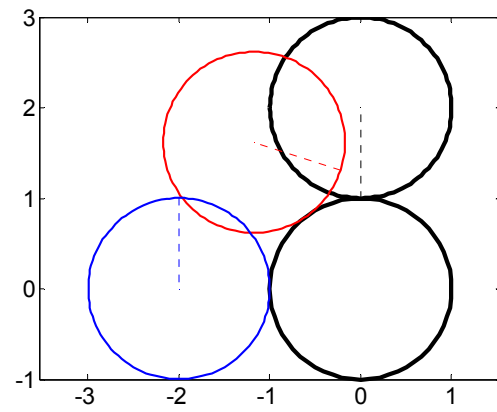
Table 3.3 Dimension of Ω_A and Ω_B .

Case	Ω_A (convex)		Ω_B	
	b_1/a_1	a_1 (cm)	b_2/a_2	a_2 (cm)
1(a) and 1(b)	0.5	2	0.4	2.5
2(a) and 2(b)	1	1	1	1

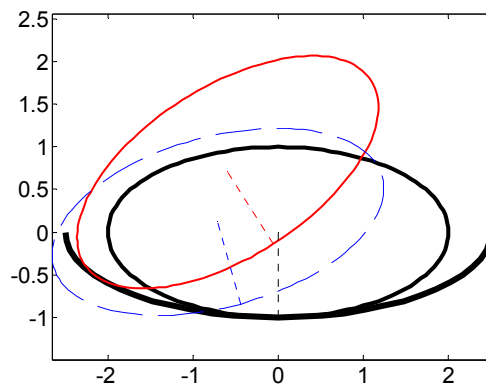
Case (a): Ω_B is convex; and Cases (b): Ω_B is concave. ($\omega = \pi / 6$ rad/s).



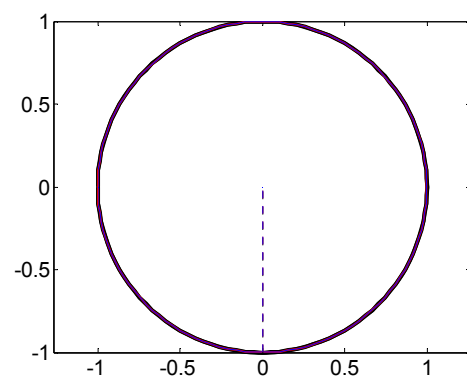
Case 1(a): Ω_B is convex.



Case 2(a) : Ω_B is convex.

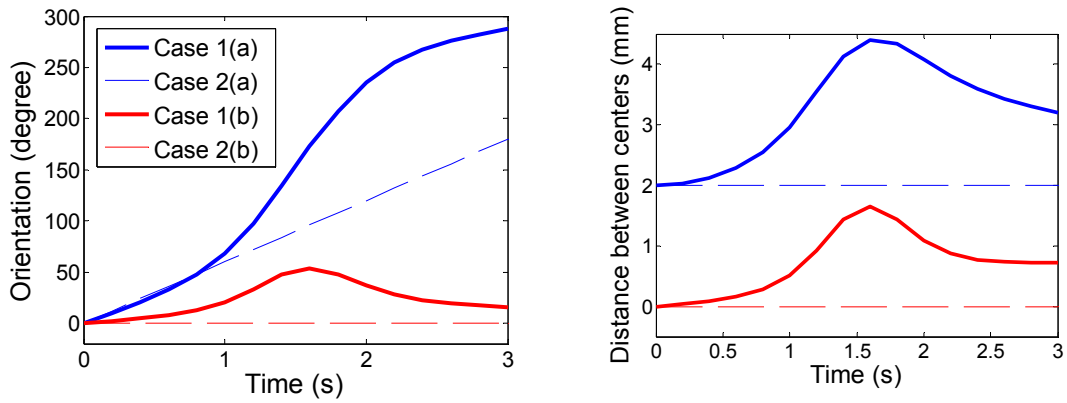


Case 1(b): Ω_B is concave



Case 2(b): concentric cylinders

Figure 3.7 Snapshots illustrating the effect of shape.



(a) Orientation.

(b) Distance.

Figure 3.8 Effect of Ω_B on Ω_A position / orientation.

3.1.2 Human Knee Kinematics

With MRI data, a model can be built to provide a good understanding of the kinematics and kinetics of a bio-joint (consisting of non-uniform shaped contact parts), and estimate its contact locations, rolling/sliding velocities and forces/torques involved.

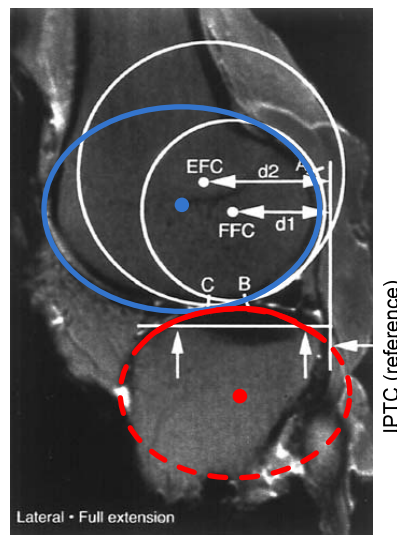


Figure 3.9 MRI of a cadaver knee.

Figure 3.9 shows a lateral sagittal MRI of an unloaded cadaver knee [26], where the two white circles are approximated geometries for the femoral articular surfaces. Data are presented as positions of the extension facet center (EFC) and flexion facet center (FFC) in Figure 3.9, where the contact is modeled as a point between a circle and a plane. To provide a continuous differentiable function, a more general bio-joint representation based on elliptical geometries is proposed in Figure 3.1 to characterize the observed data for analyzing the contact kinematics and kinetics, where Ω_A and Ω_B are two bodies with surfaces Ω_A and Ω_B respectively; and the angular velocity ω describes the motion of Ω_A rolling on Ω_B at the instantaneous contact point C.

In [26], two circles, each of which rolls on a different flat facet, were used for the sagittal section of the medial tibiofemoral compartment but for the lateral tibiofemoral compartment, two circles roll on the same flat facet. In this paper, the simulations focus on the lateral part as it has a larger displacement than the medial part. The following three models are compared:

Model 1: Two sequential circles roll a flat plane [26].

Model 2: One ellipse rolls on a flat plane.

Model 3: One ellipse rolls on another ellipse.

The dimensions of the approximated circles and ellipses (Figure 3.1) are listed in Table 3.4. With the contact location defined as a horizontal distance of C measured from the IPTC in Figure 3.9, results are given as a function of the flexion angle θ in Figure 3.10 for comparing three models against published data. Figure 3.11 simulates (on the basis of Model 3) the snap-shot trajectory of the lower leg as it rotates from its initially

full extension, and its corresponding (rolling/sliding) displacements, velocities as well as the s_{roll}/s_{slide} ratio.

Table 3.4 Geometry approximation.

Circles [26]		Ellipse (green dash)	
$r_1 = 21\text{mm}$	$r_2 = 32\text{mm}$	$r_{maj} = 25.3\text{mm}$	$r_{min} = 21.1\text{mm}$
Ellipse (blue)		Ellipse (red)	
$r_{maj} = 33.6\text{mm}$	$r_{min} = 23\text{mm}$	$r_{maj} = 28.8\text{mm}$	$r_{min} = 18.8\text{mm}$
Initial contact position = 31mm			
Angular velocity $\omega = 1.57 \text{ rad/s}$			

Observations in Figure 3.10 and Figure 3.11 are discussed as follows:

- 1) For Model 1, the s_{roll}/s_{slide} ratio is given as 1.7. As the sliding velocity of each rolling circle is assumed constant, the contact point is a linear function of θ . The overall result, however, is not a smooth curve (Figure 3.10) due to the transition from circles r_2 to r_1 .

The difference between the 2-circle model and experimental results can be observed when $\theta > 90^\circ$. This is because the rotational axis of the circle is tilted by a small angle; when projected on the camera plane, the tilted circle is essentially as an ellipse.

- 2) Based on the above observation, we model bio-joints using elliptical surfaces as they offer a more realistic characterization than a multi-circle model, and are mathematically differentiable.

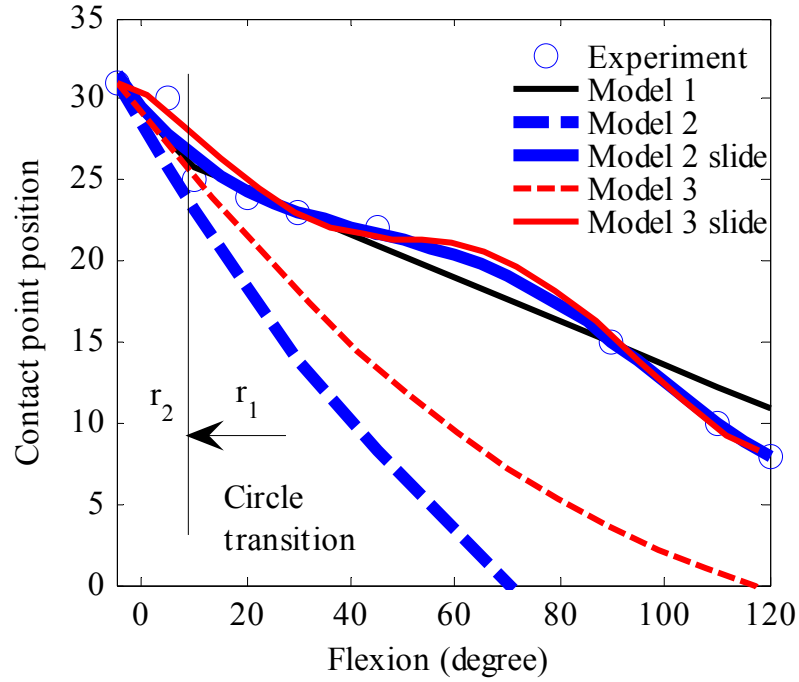


Figure 3.10 Comparison of current contact point C.

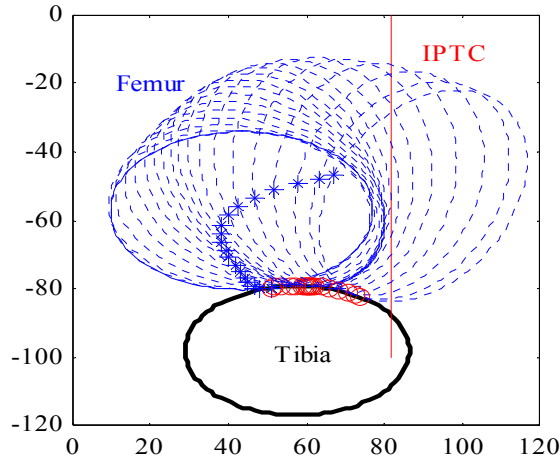
Figure 3.10 compares Models 2 and 3 against published data. With only rolling, Model 2 (that simplifies the tibial condyle as a planar surface) results in some negative contact positions; this is intuitively incorrect as the knee joint does not lose contact. Given the close match between Model 3 (when considering both sliding and rolling in the joint kinematics) and the experiment data, Model 3 with sliding is used for the subsequent analysis.

- 3) The displacements, $s_{roll}(\theta)$ and $s_{slide}(\theta)$, normalized to the major radius of the femoral condyle, are given by (3.10a) and (3.10b) respectively, and their ratio is plotted in Figure 3.11(b):

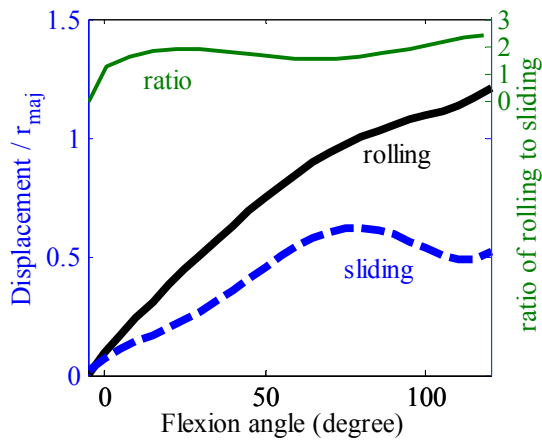
$$s_{roll}(\theta) / r_{maj} = 0.093\theta^5 - 0.409\theta^4 + 0.57\theta^3 - 0.448\theta^2 + 0.926\theta \quad (3.10a)$$

$$s_{slide}(\theta) / r_{maj} = 0.334\theta^5 - 1.518\theta^4 + 2.12\theta^3 - 0.996\theta^2 + 0.513\theta \quad (3.10b)$$

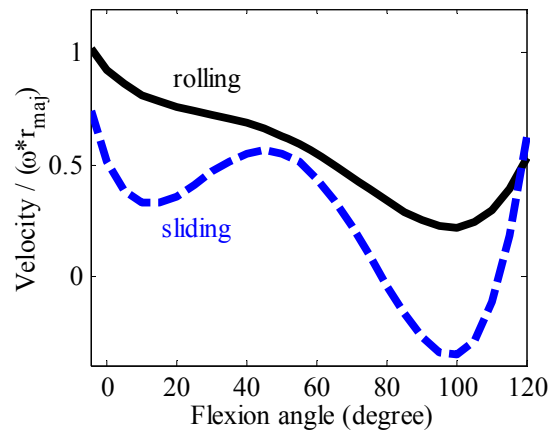
The $s_{\text{roll}}/s_{\text{slide}}$ ratio is not a constant, but its average value of 1.69 closely agrees with the experimental observation [26] of 1.7. Figure 3.11(c) graphs v_{slide} by differentiating (3.10); negative v_{slide} means sliding forward instead of backward.



(a) Snapshots of knee rotation.



(b) Rolling and sliding displacements.



(c) Rolling and sliding velocities.

Figure 3.11 Rolling and sliding velocities of the current contact point (Model 3).

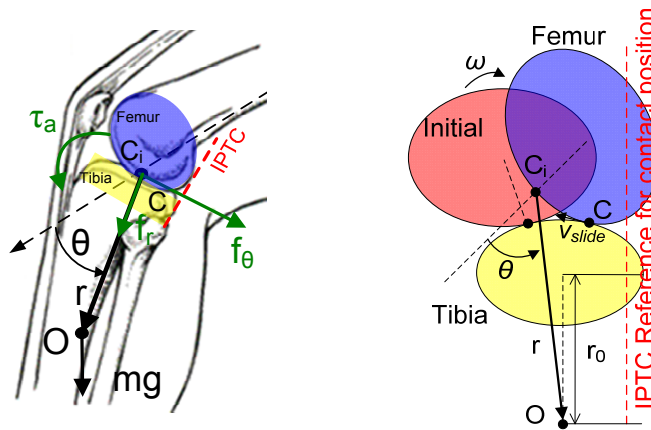
3.2 Formulation of Dynamics

The calf dynamics (relative to the upper leg) are given by (3.11):

$$m\mathbf{a} = \mathbf{f}_g + \mathbf{f}_\theta + \mathbf{f}_r + \mathbf{f}_e \quad (3.11a)$$

$$(J\ddot{\theta} + 2mr\dot{r}\dot{\theta})\mathbf{k} = \boldsymbol{\tau}_g + \boldsymbol{\tau}_a + \boldsymbol{\tau}_e \text{ where } \mathbf{k} = \mathbf{e}_r \times \mathbf{e}_\theta \quad (3.11b)$$

In (3.11a), m is the calf mass; \mathbf{f}_g is the gravity force; and \mathbf{f}_r and \mathbf{f}_θ are the resultant forces exerted by the surrounding bones and tissues (muscle and ligament) in \mathbf{e}_r and \mathbf{e}_θ directions respectively. Within a bio-joint, bones primarily support compressive forces; and soft tissues can only exert tensile forces. For example, \mathbf{f}_r represents the force from the tissues if tensile force dominates, or otherwise from the bones. With rehabilitation applications in mind, we include \mathbf{f}_e to account for the force exerted by an external device (such as an exoskeleton) and reaction from the ground. On the left hand side of (3.11b), the first term accounts for the moment-of-inertia J (about the initial contact point C_i) due to the leg rotation while the second term describes the interaction between $\dot{\theta}$ and \dot{r} due to



(a) Tibia rotation.

(b) Schematics illustration.

Figure 3.12 Coordinates illustrating the knee joint rotation.

the variation in r . In (3.11b), all the torques are computed about C_i : τ_g and τ_e denote the torques due to the gravity and external device respectively; and τ_a is a net torque accounting for \mathbf{f}_r , \mathbf{f}_θ , and tissue contraction within the knee.

The vector equations (3.11) can be recast into three scalar equations (3.12) from which f_r , f_θ and τ_a can be solved:

$$m(\ddot{r} - r\dot{\theta}^2) = f_g \sin \theta + f_r + f_{er}(\theta) \quad (3.12a)$$

$$m(2\dot{r}\dot{\theta} + r\ddot{\theta}) = f_g \cos \theta + f_\theta + f_{e\theta}(\theta) \quad (3.12b)$$

$$J\ddot{\theta} + 2mr\dot{\theta} = \tau_g + \tau_a + \tau_e(\theta) \quad (3.12c)$$

Due to the kinematic constraint imposed by the contact, the human knee joint embodies two DOFs, rotation and translation for its planar motion. To investigate the effects of a planar exoskeleton on human knee joints, we compare two different models in predicting the forces and moments acting on the knee; namely,

- pin joint engineering approximation, and
- bio joint knee (Model 3).

The exoskeleton consists of a revolute (pin) joint between two rigid links attached to the lower and upper legs with pin joints. This design has three-DOF from its three pin-joints and thus has one redundancy. For a nonzero flexion angle, there are two possible solutions. However, only one solution is physically feasible.

For clarity and ease of illustration, the following assumptions are made; 1) the human subject sits with the upper leg held static and horizontal and the lower link rotates with the tibia from its initial state (full extension); and 2) the lower link is attached at O with the revolute joint centered at the initial contact point C_i (Figure 3.12). Numerical

values used in this study are given in Table 3.5 [62] and from Figure 3.12(b) and Figure 3.11 (a),

$$r(\theta) = 1.078\theta^4 - 11.184\theta^3 + 26.542\theta^2 - 0.825\theta + 263.59 \quad (3.13)$$

(3.13) and its derivatives are graphed in Figure 3.13. Figure 3.14 shows the link kinematics (solid lines) as the tibia rotates, where dash lines simulate the knee as a pin joint (commonly assumed in exoskeleton designs) for comparison.

Table 3.5 Physical parameters of human's lower leg.

	Human		Exoskeleton
	Length (m)	Mass (kg)	Length (m)
Upper leg	0.40	7.02	0.40
Lower leg/foot	0.37/0.27	2.44/1.18	0.37
r_0 (m)	0.2453		

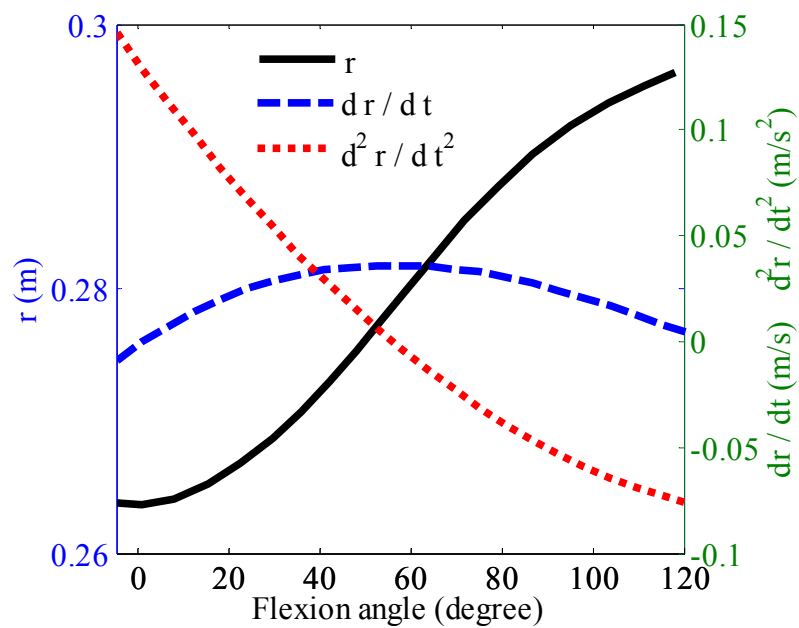


Figure 3.13 Kinematics of the tibia mass-center.

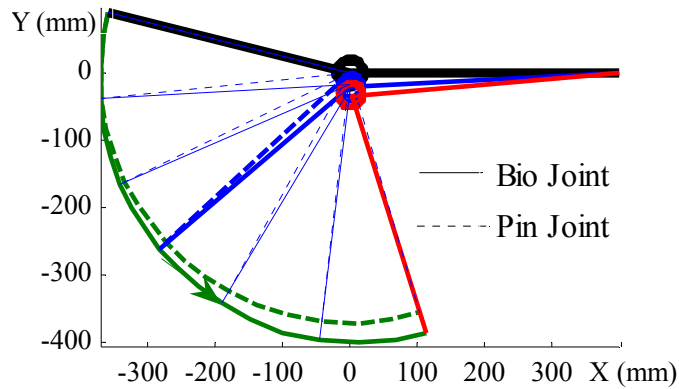


Figure 3.14 Comparing snapshots of an exoskeleton between two knee joint models.

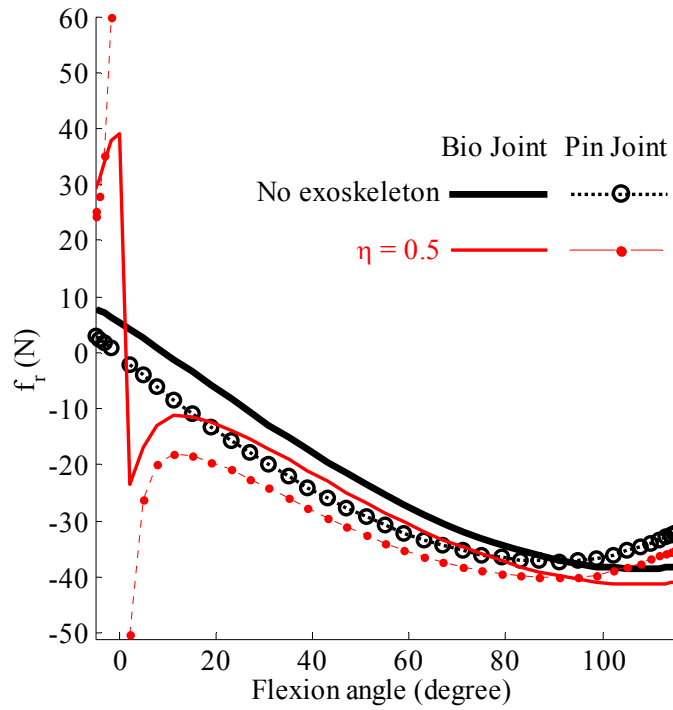
To account for the exoskeleton mass in the kinetic study, the two links are assumed to have the same mass-to-length ratio η of 0.5. Unlike the condition with no exoskeleton where the human leg is an open-chain mechanism, the leg and exoskeleton form a closed kinematic chain that has a significant effect on the internal joint forces and torque of the knee. Figure 3.15(a, b, c) are calculated results from (3.12) showing the internal forces and torque in the knee as the tibia accelerates from the initial static state ($\theta = -5^\circ$) to $\theta = 20^\circ$ for 0.5 second, then maintains at an angular velocity for 1 second to $\theta = 95^\circ$, and finally decelerates to the final static state $\theta = 115^\circ$ in another 0.5 second. Throughout the trajectory, the foot is off the ground and thus, there is no ground reaction. In Figure 3.15 where the thick and thin lines are results of the bio joint and pin joint models respectively, the internal forces and torque for a condition with no exoskeleton are plotted as a basis for comparison.

Several observations can be made from Figure 3.13 to Figure 3.15:

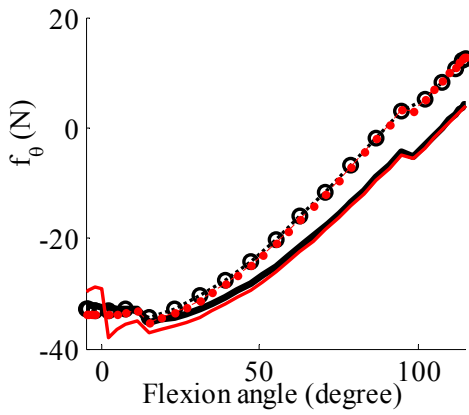
- 1) The sign of the force f_r in Figure 3.15(a) can be explained as follows. During the initial flexion ($\theta < 0$), f_r is positive since the force is primarily supported by the

femur, but becomes negative as the retraction force from the soft tissues gradually plays a more dominant role as the knee rotates downward.

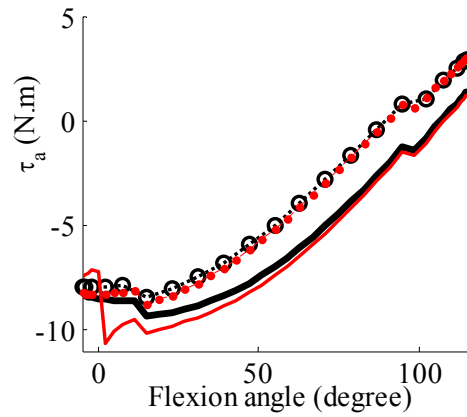
- 2) The distance r increases as much as 30mm (Figure 3.13). For the same work done, this increase in r tends to reduce f_r in the knee. As the pin joint approximation assumes a constant r and neglects the joint geometry, the effect of the $r(\theta)$ variation on the attaching point (Figure 3.14) and on the forces/torque (Figure 3.15) cannot be accounted for. As compared to the bio joint model in Figure 3.15(a), the pin joint approximation overestimates $|f_r|$ in the range ($0^\circ < \theta < 90^\circ$) and underestimates as θ approaches its rotation limit.
- 3) Near $\theta=0^\circ$, the exoskeleton loses one DOF along the \mathbf{e}_r direction causing a finite change in f_r as well as f_θ and τ_a as shown in Figure 3.15. Human knee (that can roll and slide) is more tolerant than a pin-joint to a singularity along \mathbf{e}_r as illustrated in Figure 3.15(a). However, these internal forces and torque increase with the mass-to-length ratio η of the exoskeleton. An increase in η from 0.5kg/m to 1kg/m implies that f_r (at $\theta=0^-$, $\theta=0^+$) would increase from (39N, -24N) to (73N, -51N). The pin joint approximation, which neglects the $r(\theta)$ variation, cannot capture the finite change in f_r and also grossly underestimates the singularity effect on f_θ and τ_a .
- 4) The trapezoidal-velocity θ trajectory (commonly used in robotics) has an effect on the tangential force f_θ and moment τ_a . As seen in Figure 3.15 (b) and Figure 3.15 (c), the two sudden changes at $\theta=20^\circ$ and $\theta=95^\circ$ (on the simulated f_θ and τ_a) are reactions from the soft tissues in order to meet the acceleration changes specified in the θ trajectory.



(a) Pin-joint knee approximation overestimates f_r in the range $-5^\circ < \theta < 90^\circ$ and underestimated in $\theta > 90^\circ$ as compared to the bio-joint knee model.



(b) Tangential force f_θ .



(c) Moment τ_a .

Figure 3.15 Force and torque comparison between two knee joint models (with/without exoskeleton).

3.3 Summary

In this chapter, a general method for mathematical modeling a bio-joint has been introduced, which provides a better understanding on the interaction between natural joints and artificial mechanisms for design and control of rehabilitation exoskeletons. With the aid of published MRI data, the ellipsoid-based bio-joint model has been shown to offer a physically more accurate account of both rolling and sliding motion within bio-joint than a geometrically simple pin-joint approximation or methods based on multiple circles and lines. The bio-joint model shows that the sliding-rolling displacement ratio is not a constant but has an average value consistent with published measurements and its mathematically differentiable property facilitates the analysis of rolling/sliding velocity. Finally, the effects of a planar exoskeleton on a human knee joint have been numerically illustrated by comparing results of two different knee models (pin-joint approximation and bio-joint model derived from published MRI data). A single-DOF pin-joint approximation (that oversimplifies the knee joint geometry) cannot account for the effect of the translational variation on the attaching point of the exoskeleton, and on the internal forces and torque in the knee. While a detailed exoskeleton design to accommodate joint flexibility of a knee is beyond the scope of this chapter, some intuitive insights presented here are potentially useful considerations for future design of rehabilitation exoskeletons.

CHAPTER IV

MODEL AND ANALYSIS OF A BIO STRUCTURE

This chapter employs the CBM subject to a BJC to investigate the carcass musculoskeletal deformation under wing manipulation to facilitate the deboning of chicken breast meat. As briefly discussed in Section 1.1, the breast-meat removal operation consists of two major cuts as illustrated in Figure 1.1(b). The first cut, notably the most difficult to automate, is a cut through the shoulder joint severing the two main ligaments (A and C). Once the two ligaments have been cut, the second cut continues the incision from the back of the shoulder down through the third ligament B, and along the scapula bone. After the knife exits at the base of the scapula the breast-meat can be removed. This is accomplished by a robot which pulls and twists on both wings before removing the wings and breast meat from the carcass.

Figure 4.1 shows the automated wing manipulation (AWM) system developed at Georgia Tech [46] for tensioning the ligaments/tendon of a chicken front-half for subsequent harvesting of the chicken breast meat, where the AWM with a 6 DOF force/torque sensor is mounted on an ABB robot arm. As the AWM system pulls or twists the chicken wing, significant deformations on the shoulder were observed. This gives rise to significant errors in locating the shoulder joint (and thus the blade) resulting in low yield/quality of deboned breast meat. In order to predict the chicken carcass

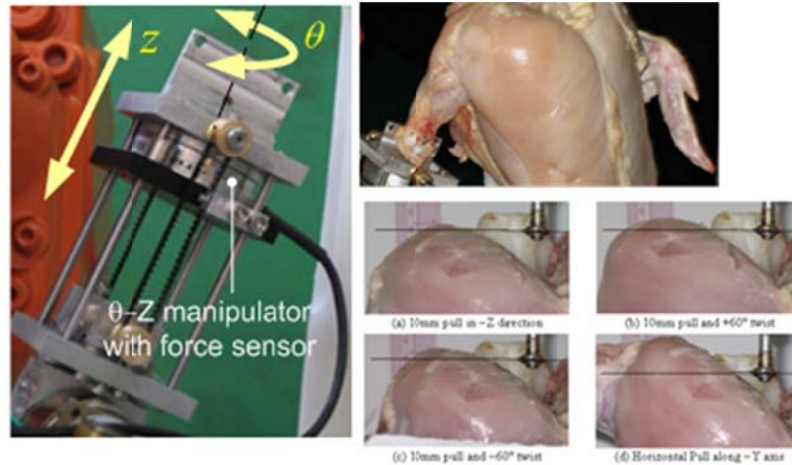


Figure 4.1 The effect of wing manipulation on shoulder location.

deformation under wing manipulation, a musculoskeletal model that can be implemented on the mechanical meat harvester to guide the cutting blade is needed.

Figure 4.2 illustrates the problem to be solved in this chapter: predict the carcass shoulder position for the given wing manipulation motions which include both pulling displacement and twisting angle. The clavicle, which is modeled as a 3-D compliant beam, plays as a key role in affecting the shoulder position. The pulling displacement and twisting angle, which result in joint motions and ligament deformation provide boundary constraints on the clavicle. After the coordinate systems are introduced for the carcass in Section 4.1.1, the joint motions are captured as BJC in Section 4.1.2 and the beam model is formulated for the clavicle in Section 4.1.3. Then, the constitutive relation for the ligaments will be formulated in Section 4.1.4. Due to lack of available material properties, experiments on clavicles and ligaments will be presented in Section 4.2. Finally, the illustrative example of wing manipulation will be given in Section 4.3.

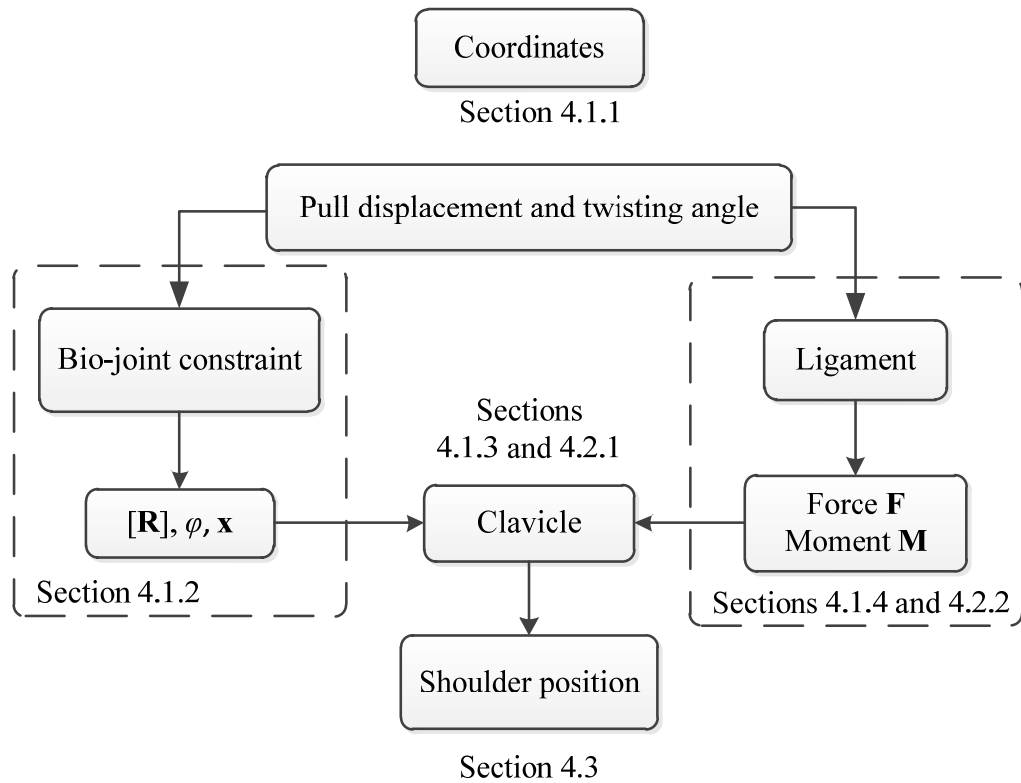


Figure 4.2 Flow chart of bio structure modeling.

In summary, this chapter offers the followings:

- 1) A framework of a musculoskeletal model is provided by a compliant beam model for bones and an exponential model for tendon/ligaments.
- 2) Numerical verification is presented for the compliant beam model. The soft-tissue model is validated by experiments and values of its coefficients are determined.

This musculoskeletal model has been used to investigate the effects of natural product size variation on the bio-structural deformation. This analysis will contribute to the future wing manipulator design and related controller implementation.

4.1 Formulation of Bio Structure Model

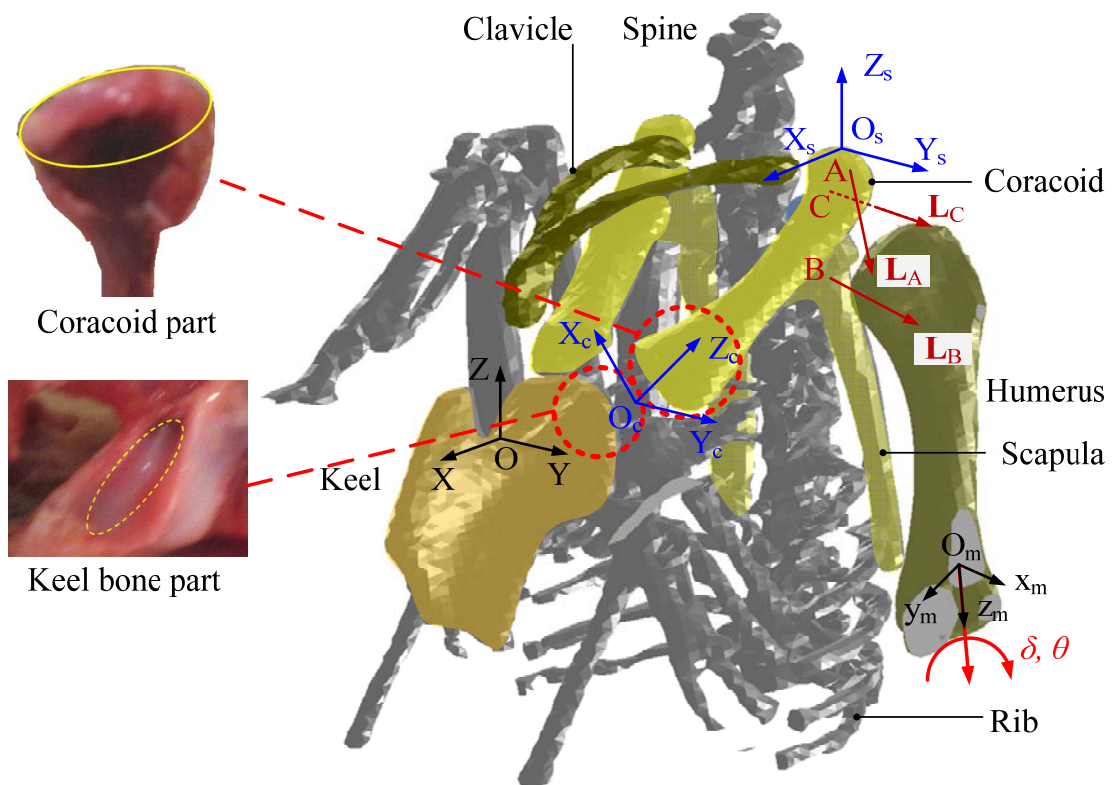
Figure 1.1(a) illustrates the bio-structure consisting of the shoulder bones and three ligaments (indicated as A, B, C) connecting the humerus to the three shoulder bones; coracoid, clavicle and scapula. The shoulder joint has three rotational DOFs and due to the deformability of the connective tissues; it is possible to attain limited translational motion of the humerus relative to the fixed carcass.

In this section, the following assumptions are made:

- A1) The carcass is properly loaded on the cone such that the symmetric plane of the carcass coincides with that of the cone. Additionally, the rib cage does not rotate on the cone. Thus, the rib cage and keel bones are treated as rigid bodies with respect to the cone.
- A2) The coracoid-keel and shoulder joints can be characterized as contacts between two ellipsoids, thus can be modeled as BJC on the flexible clavicle. Material property of the clavicle is isotropic and linear elastically.
- A3) All the ligaments/tendons within a bird carcass are of the same material and structure so that their deformation behavior can be described by one general characteristic exponential relation [63]. The soft tissue material is anisotropic and incompressible; this assumption is based on the knowledge of the high percentage of water content within the soft tissue and its longitudinal fiber bundle structure.

4.1.1 Coordinates

To describe the pull δ and twist θ motions of the humerus, the kinematics is defined in Figure 4.3. The reference coordinate system O is set on the keel bone where the prong plugs in. The X and Z axes (of frame O) are on the symmetric plane of the carcass; the Z axis points upwards while the X axis is the direction that the cone moves toward. The frames, O_c and O_s , are the local coordinate systems at the coracoid-keel and the shoulder joints, respectively. The Z_c axis is the longitudinal axis of the coracoid; X_c is the normal to the plane defined by the two intersecting axes of the coracoids. As shown in Figure 4.3, $O_c O_s$ is in the direction of the Z_c axis, and defines the length of the



(A. Coracohumeral, B. Scapulohumeral, C. Interfibrous ligaments)

Figure 4.3 Ligament-skeletal structure of a chicken carcass.

coracoid. The $X_s Y_s Z_s$ and XYZ are parallel and related only by a transitional transformation. A local coordinate manipulating frame O_m is attached at the other end of the humerus with its z_m -axis pointing toward and along the humerus longitudinal axis. In Figure 4.3, the attachment points of the ligaments on the coracoid and scapula are denoted as points A, B and C, correspondingly; and the lengths and directions are characterized by the vectors \mathbf{L}_A , \mathbf{L}_B and \mathbf{L}_C in the referenced frame O.

It is of particular interest here how the tripod-like structure of the shoulder (coracoid, clavicle and scapula) deforms with the two joints; namely, the joint between the coracoid and keel bone, and the shoulder joint. Because of the flexibility in the clavicle and joints, manipulating the wing for cutting could result in a significant displacement of the shoulder. Since the bases of the clavicle is attached to the shoulders, which displace and rotate with the coracoid-keel joint and are subjected to the tendon forces, results of the BJC serves as boundary conditions for the CBM in analyzing the deformation of the tripod-like structure to predict shoulder displacement under wing manipulation.

4.1.2 Bio Joint Constraint on Clavicle

In the bio joint model, O_c is defined as the geometric center of the ellipse that models the portion of the coracoid as shown in Figure 4.3. The coordinate transformation from O to O_c involves two rotations (about Y by θ_y followed by about X_c by θ_x) and a transition (O to O_s), and is given by:

$$\mathbf{x}_{O_c} = [\mathbf{R}] \mathbf{x}_O + \mathbf{p}_{co} \quad (4.1)$$

where \mathbf{R} is a rotational matrix, \mathbf{p}_{co} is the position vector from O_c to O.

Figure 4.3 shows the ellipses approximating the contact parts within the coracoid-keel joint. Dimensions of the joints and bones are listed in Table 4.1. We illustrate numerically the effect of the coracoid-keel joint rotation (characterized by the rotational variables θ_x and θ_y) on the position changes of the tripod-like structure. The simulations are based on typical dimensions experimentally measured from commercial broilers (meat chickens). As shown in Figure 4.4 and Figure 4.5, the contact pair making up part of the tripod-like shoulder structure of the chicken can be modeled as either ellipsoids or an elliptical cylinder. Specific values of the 3D ellipsoid principal axis lengths used in the simulations are given in Table 4.1.

When tensioning the ligaments and tendon for the first cut in deboning the chicken breast meat, the humerus is pulled downward, the position/orientation of the tripod-like structure changes as a result of the joint rotations (θ_x and θ_y), the nominal

Table 4.1 Dimensions of coracoid-keel joint and bones.

Coracoid-keel joint (mm)		Shoulder joint (mm)	
Coracoid	9.2, 3.1, 2.3	Coracoid	2.6, 6.6, ∞
Keel	10.2, 4.1, 1.9	Humerus	9.3, 7.0, 5.6
Bone	Length (mm)	Position	Value
Coracoid	38.3	O_c (mm)*	(-15.0 -10 20.4)
Humerus	80.7	θ_x	$\pi/12$
Scapula	75.0	θ_y	$\pi/4$
Sliding velocity between the two parts in bio joint =1mm/s			

* O_c 's coordinates are presented in the world frame O.

values of which are given in Table 4.1. To offer intuitive insights to the effect of $\Delta\theta_x$ and $\Delta\theta_y$ (deviations from the nominal values) on the predictions of shoulder positions (with respect to the reference coordinate system O), we compare in Figure 4.4 and Figure 4.5 the results calculated using both the bio joint model and the ball joint approximation. To quantify the difference, we define the following percentage error:

$$\%Error = 100\% \times (\Delta d_e / \Delta d_{bio})$$

where Δd_{bio} is the position deviation from its nominal value as predicted by the bio joint model; and Δd_e is the difference between the results predicted by the two models. In Figure 4.4 and Figure 4.5, the percentage errors near the nominal position ($\Delta\theta_x = \Delta\theta_y = 0$) are not calculated to avoid the undefined problem of dividing zero with zero.

Some observations can be made from Figure 4.4 and Figure 4.5:

- 1) In Figure 4.4, the error decreases as the rotation angle becomes larger. This is because of the error definition and the nonlinear effect of the bio joint model; in other words, Δd_{bio} increases at a faster rate than Δd_e .
- 2) In general, the shoulder deforms nonlinearly from its nominal position even in small angle rotation.
- 3) The shoulder joint is possible to attain limited translational motion of the humerus relative to the fixed carcass (in addition to the three rotational freedoms) due to the deformability of the connective tissues. The ball joint approximation, which assumes a fixed center at O_c , does not account the transitional motion as can be visualized in Case 2(b) in Figure 3.8. Hence, the ball-socket approximation predicts a linear relation in small angle rotation about the nominal position. The significantly large Δd_e error (over 40%) implies that the ball joint approximation

is inadequate to characterize the CK joint and its associated bio-skeleton kinematics. The bio joint model with two 3D ellipsoids provides a means to account for the transitional motion of O_c within the clearance in the joint.

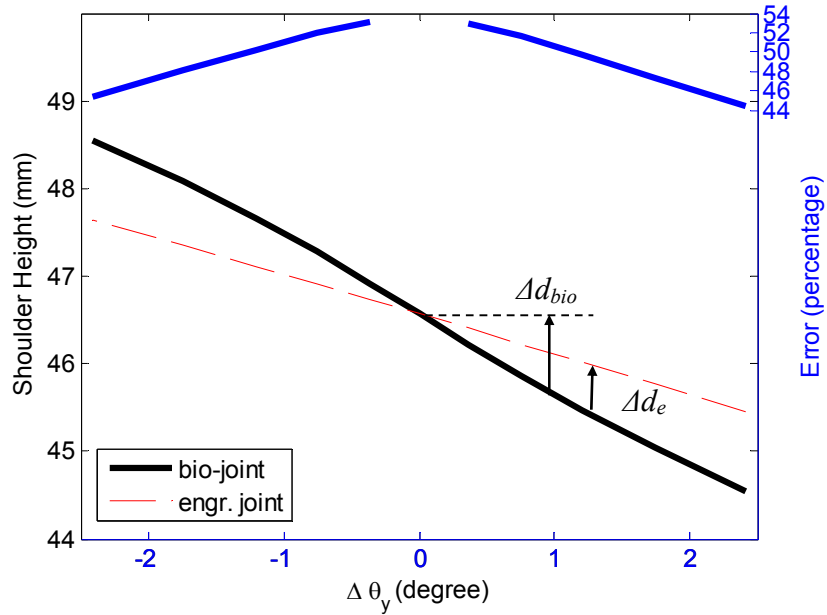


Figure 4.4 Change of shoulder height due to $\Delta\theta_y$.

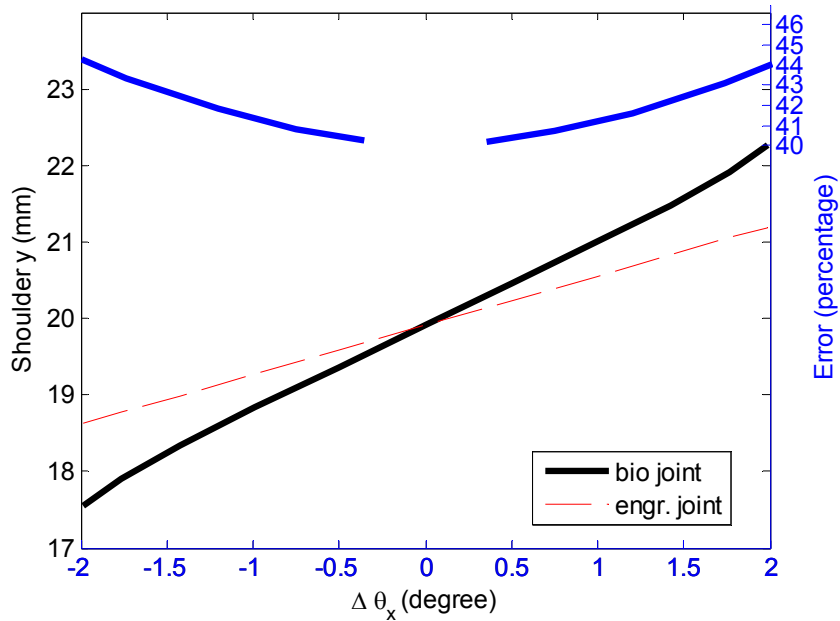


Figure 4.5 Change of shoulder position due to $\Delta\theta_x$.

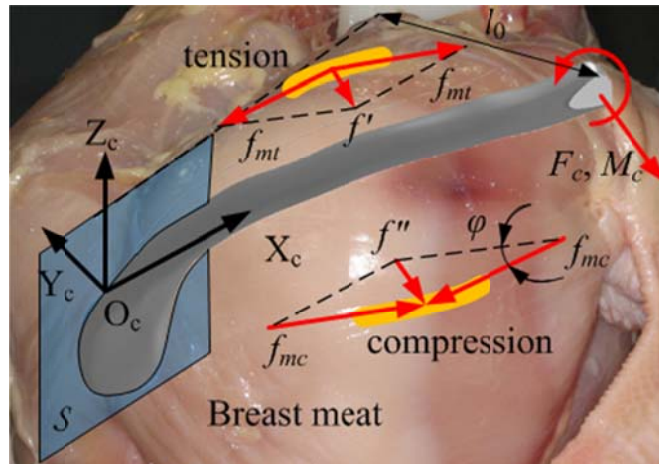
4.1.3 Clavicle Model

Section 4.1.2 provides the relationship between the coracoid rotation ($\Delta\theta_x, \Delta\theta_y$) and the shoulder displacement. This in turn provides a means to relate the rotational matrix \mathbf{R} to absolute position \mathbf{x}_0 of the shoulder (where the clavicle is attached). Hence, the boundary conditions for (2.26) are given by

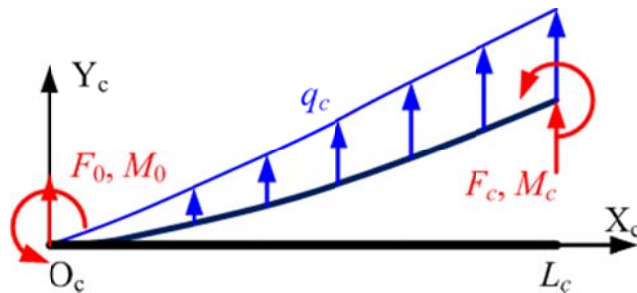
$$\begin{aligned} s = 0 & \quad R_{11} = 1, R_{12} = 0, R_{13} = 0, \varphi = 0, x_1 = x_1^{(0)}, x_2 = x_2^{(0)}, x_3 = x_3^{(0)} \\ s = 1 & \quad F_1, F_2, F_3, M_1, M_2, M_3 \end{aligned}$$

Because of the V-shape geometry of the clavicle, Figure 4.6(a) shows one half of the clavicle which is separated by the symmetric plane S (OXZ in Figure 4.3). Then this tiny clavicle bone is modeled as a cantilever beam mounted at point O_c (with axis X_c pointing along the bone axis and Z_c being the same as Z). The clavicle is subjected to force F_c and moment M_c from the shoulder as well as the distributed force from the surrounding breast meat. In Figure 4.6(a), two meat elements along the fiber direction are presented on both sides of the clavicle. As the end of the clavicle is pulled/twisted by F_c and M_c , one element is in tension f_{mt} and the other is in compression f_{mc} , resulting in an effective distributed force $q_c (= f' + f'')$ along the bone, where $f' \approx \varphi_m f_{mt}$ and $f'' \approx \varphi_m f_{mc}$. The angle φ_m is defined as the slope angle change per fiber length, which is very small for smooth breast meat surfaces. Certain assumptions are made in the following formulation:

- A4) The bone material is assumed to be isotropic and linear elastic, because of its small dimension and limited deflection during the wing manipulation.
- A5) The bone deformation in the X_c and Z_c directions is negligible compared to deflection in Y_c , because the bone is relatively rigid in the longitudinal axis and



(a) Local coordinate and loadings for one half of clavicle.



(b) Compliant beam formulation.

Figure 4.6 Clavicle deformation.

the clavicle tip (point O_c) can move in plane S to compromise possible vertical deflections due to the shoulder deformation.

- A6) The outer surface of breast meat is stress free initially, and will deform under wing manipulation as much as an elastic foundation of linear springs. Specifically, the distributed force is proportional to the deformation displacement. The value of φ_m is assumed to be 0.005.

Figure 4.6(b) shows the free body diagram of the clavicle, where the initial length is L_c . For simplicity, the subscript “c” in the coordinates X_c and Y_c is neglected, and the governing equation of the compliant beam model is given by

$$EIy'' = -M_0 + F_0x + \int_0^x (x - \xi)q_c d\xi \quad (4.2a)$$

where the double primes refer to the second derivative with respect to x , the force F_0 and moment M_0 at $x = 0$ can be obtained at equilibrium:

$$F_0 = -\int_0^{L_c} q_c d\xi - F_c$$

$$M_0 = -\int_0^{L_c} \xi q_c d\xi - F_c L_c - M_c$$

Then (4.2a) can be rewritten as

$$EIy'' = \int_{L_c}^x (x - \xi)q_c d\xi + F_c(L_c - x) + M_c \quad (4.2b)$$

and the third and fourth order derivatives are obtained as

$$EIy''' = \int_{L_c}^x q_c d\xi - F_c \quad (4.2c)$$

$$EIy'''' = q_c \quad (4.2d)$$

If denoting $\mathbf{Y}=[y \ y' \ y'' \ y''']^T$, the above equations can be combined into a compact form:

$$\mathbf{Y}' = \mathbf{F} \quad (4.3)$$

with

$$\mathbf{F} = \begin{bmatrix} \mathbf{0} & \mathbf{I}_{3 \times 3} \\ q_c / EI & \mathbf{0}^T \end{bmatrix}$$

The boundary conditions are determined from the cantilever constraint and (4.12b,c):

$$y(0) = 0, y'(0) = 0 \quad (4.4a,b)$$

$$EIy''(L_c) = M_c, EIy'''(L_c) = -F_c \quad (4.4c,d)$$

This boundary value problem (BVP) can be readily solved by SMs.

Closed form solution

The boundary value problem is first recast into an IVP (4.12d) with initial conditions given in (4.14a,b) and (4.14e,f):

$$EIy''(0) = \int_0^{L_c} \xi q_c d\xi + F_c L_c + M_c \quad (4.4e)$$

$$EIy'''(0) = -\int_0^{L_c} q_c d\xi - F_c \quad (4.4f)$$

Based on assumption A6) of an elastic foundation, the functional form of q_c is taken as

$$q_c = k_m y \quad (4.5)$$

where k_m is an effective elastic constant. Substituting (4.15) into (4.12d), the general solution for $EIy'''' = k_m y$ is

$$y = A_1 e^{\lambda x} + A_2 e^{-\lambda x} + A_3 \cos \lambda x + A_4 \sin \lambda x \quad (4.6)$$

where $\lambda = (k_m / EI)^{1/4}$ and A_i 's ($i = 1, 2, 3$ and 4) are coefficients to be determined by the initial conditions at $x=0$. By substituting (4.15) and (4.16) into (4.4a,b,e,f), four algebraic equations of $\mathbf{A} = [A_1 A_2 A_3 A_4]^T$ can be obtained and written in a matrix form of

$$\mathbf{M}_A \mathbf{A} = \mathbf{b}_A \quad (4.7)$$

where \mathbf{b}_A and \mathbf{M}_A are given as

$$\mathbf{b}_A = [0 \quad 0 \quad -F_c \quad F_c L_c + M_c]^T$$

$$\mathbf{M}_A = \begin{bmatrix} 1 & 1 & 1 & 0 \\ \lambda & -\lambda & 0 & \lambda \\ EI\lambda^3 & -EI\lambda^3 & 0 & -EI\lambda^3 \\ EI\lambda^2 & EI\lambda^2 & -EI\lambda^2 & 0 \end{bmatrix} + k_m \begin{bmatrix} \mathbf{0}^T \\ \mathbf{0}^T \\ \boldsymbol{\alpha}^T \\ \boldsymbol{\beta}^T \end{bmatrix}$$

with

$$\boldsymbol{\alpha} = \frac{1}{\lambda} [-1 + e^{\lambda L_c} \quad 1 - e^{-\lambda L_c} \quad \sin \lambda L_c \quad 1 - \cos \lambda L_c]^T$$

$$\mathbf{\beta} = \frac{1}{\lambda^2} \begin{bmatrix} 1 + e^{\lambda L_c} (-1 + \lambda L_c) \\ 1 - e^{-\lambda L_c} (1 + \lambda L_c) \\ -1 + \cos \lambda L_c + \lambda L_c \sin \lambda L_c \\ -\lambda L_c \cos \lambda L_c + \sin \lambda L_c \end{bmatrix}$$

Then the closed form solution can be obtained by solving A_i 's from (4.7) and substituting them into (4.6). On the other hand, if the functional form of q_c is taken as (4.5'),

$$q_c = k_m x \quad (4.5')$$

The closed form solution is given as follows:

$$y = -\frac{k_m}{120EI} x^5 + \frac{k_m L_c^2 + 2F_c}{12EI} x^3 + \frac{3M_c + 3f_c L_c - k_m L_c^3}{6EI} x^2 \quad (4.6')$$

It will be shown that as the loadings increase, the solution (4.5) can be approximated by (4.6') which is much easier for further investigation on dimension effects.

The elastic foundation assumption for modeling the breast meat in this work is employed as a lumped parameter approach. But the numerical value of k_m can be estimated based on theoretical derivation and experiment data. This starts with the stress-strain relation of meat:

$$\sigma_m = E_m \varepsilon_m \quad (4.8)$$

where E_m is the elastic modulus of meat, σ_m and ε_m are longitudinal stress and strain along the fiber direction. Denoting the minor axis length of the clavicle cross section as $2b$, one half of the shoulder width as l_0 , and the Poisson ratio as $\nu = 0.5$, the distributed load on the clavicle q_c and strain in the lateral direction ε'_m can be expressed as

$$q_c = \varphi_m \sigma_m \cdot 2b \quad (4.9)$$

$$\varepsilon'_m = \frac{y}{l_0} = \nu \varepsilon_m \quad (4.10)$$

Based on (4.5), (4.7), (4.8) and (4.9), the equivalent elastic constant can be estimated as

$$k_m = \frac{2\varphi_m b E_m}{\nu l_0} \quad (4.11)$$

4.1.4 Soft Tissue Mechanics

Figure 4.7 shows the schematic structure of the ligament or tendon, where the soft tissue is divided into fiber bundles on hierarchy levels [64]. Since the concepts of stress and strain are based on local deformation, the force-extension relations of ligaments and tendons with various sizes are readily obtained through integration if the characteristic relation of each collagen is available. This general characteristic relation is very helpful in modeling different ligaments/tendons within one bird as well as in a large sample of birds by accounting for the variable size.

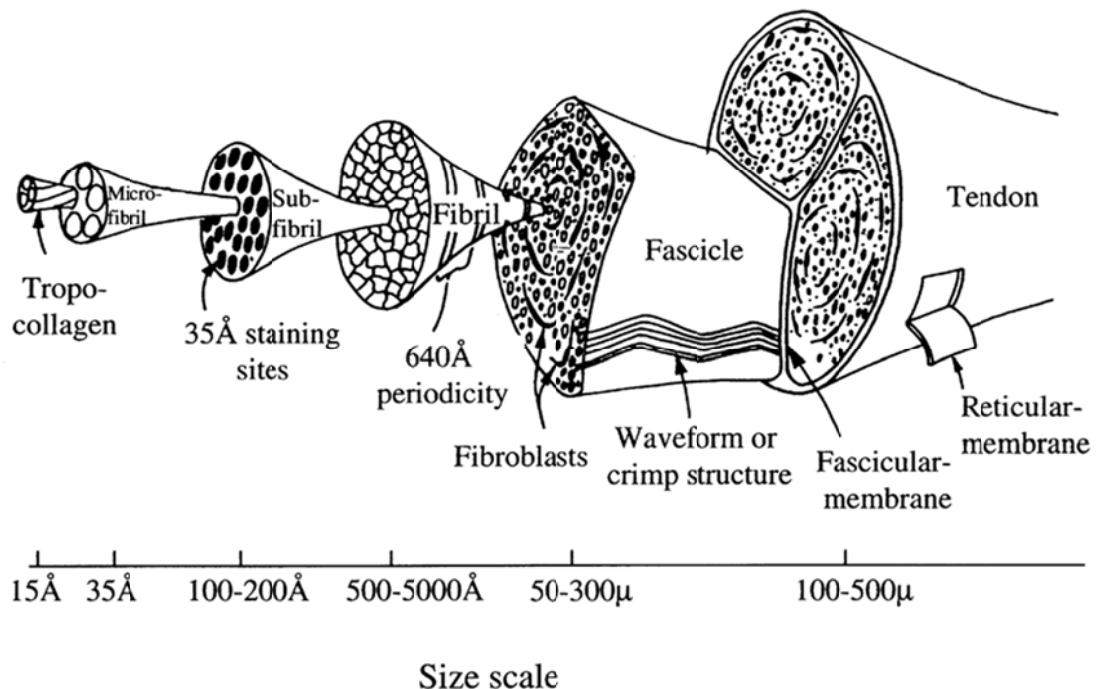


Figure 4.7 Structural hierachy of ligament or tendon.

Based on assumption A3), the characteristic relation is given by

$$\sigma = k_2 e^{k_1 \varepsilon} \quad (4.12)$$

where σ is the stress; ε is the longitudinal strain of the ligament under uni-axial extension; and k_1 and k_2 are constants to be determined experimentally. Equation (4.12) can be transformed into the following linear logarithmic form for determining k_1 and k_2 using the linear regression method:

$$\log \sigma = k_1 \varepsilon + \log k_2 \quad (4.13)$$

Because of the incompressible assumption, the volume will not change before and after loading. Denoting the initial cross section area as A_0 , the current cross section area can be obtained by

$$A = A_0 / (1 + \varepsilon) \quad (4.14)$$

Since $\sigma = f / A$, $\varepsilon = \Delta / L_0$, where Δ is the stretch and L_0 is the initial length, the relation between the stretch Δ and the tensile force f acting on the ligament is given by

$$f = \frac{A_0}{1 + \Delta / L_0} k_1 e^{k_2 \Delta / L_0} \quad (4.15)$$

It is noted that the elastic modulus E of the clavicle and the two parameters, k_1 and k_2 , for soft tissues in (4.6) and (4.15) are unknown to be determined experimentally.

4.2 Experimental Investigation

Since the material properties of the clavicle bone and the ligament are not available, the clavicle elastic modulus in (4.6) and the parameters in the characteristic equation (4.15) for ligaments were determined from two sets of experiments. Although only one or two parameters are determined by the simple pulling tests, the resulting

models are valid for nonlinear deformation analysis of the bio structure. Specifically, the nonlinear deformation of the clavicle results from its nonlinear curved geometry even though linear elastic property is assumed when only the elastic modulus E is measured. On the other hand, the nonlinear deformation of the ligament comes from its nonlinear material property, where two parameters k_1 and k_2 are to be determined.

4.2.1 Elastic modulus of clavicle

This section presents experimental determination of the elastic modulus of clavicle. Figure 4.8 shows an experimental setup up based on a commercial linear motor driven stage, where a clavicle bone is mounted on the linear slider while its tip is rigidly tied to a fixed screw by a metal string. The height can be adjusted by means of the screw for different specimens to maintain the string horizontally. As the linear slider pulls in the right direction, the clavicle will deflect as a cantilever beam. Since the metal string is much stiffer than the flexible clavicle, the elongation in the string is negligible compared to the bone deflection. So the displacement recorded from the slider can be regarded as the clavicle tip deflection. Based on the previous analysis, the vertical displacement of the clavicle is less than 7.9 mm, and the metal string length is 60 mm, so the rotation of the string is within $\tan^{-1}7.9/60 \approx 7.5^\circ$, leading to the assumption that the applying force on the clavicle tip is horizontal. At equilibrium, this applying force can be measured from the input voltage to the linear motor, which will be covered later in this section.

The pulling force of the linear motor is calibrated by an electric spring with one end fixed and the other end mounted on the slider as shown in Figure 4.9. The calibration curve of the electric spring is given by (4.16):

$$F = \begin{cases} 1.82V^2 - 0.27V + 0.09 & \text{if } V \leq 1 \\ 3.37V - 1.73 & \text{if } V > 1 \end{cases} \quad (4.16)$$

The curve exhibits a linear force-voltage relationship when V is larger than 1 volt. Because of the static friction which is estimated as 1.73N, the nonlinear relation noticeably dominates for the voltage less than 1 volt. In the experiment, the linear motor pulls the clavicle with a ramping current input. The force can be calculated from the input current using (4.16) while the clavicle tip deflection is measured by the encoder on the motor.

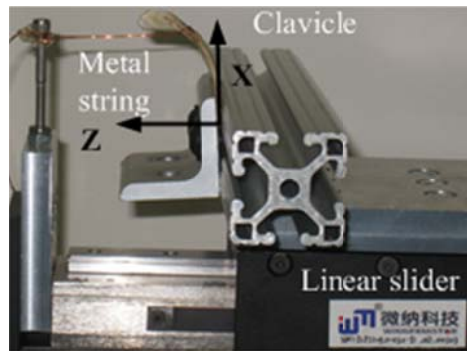


Figure 4.8 Experiment setup with a calibrated linear motor.

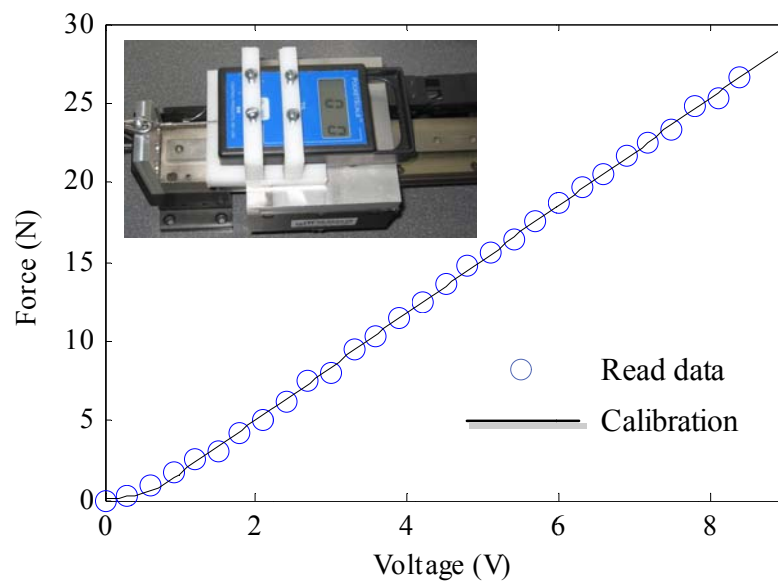
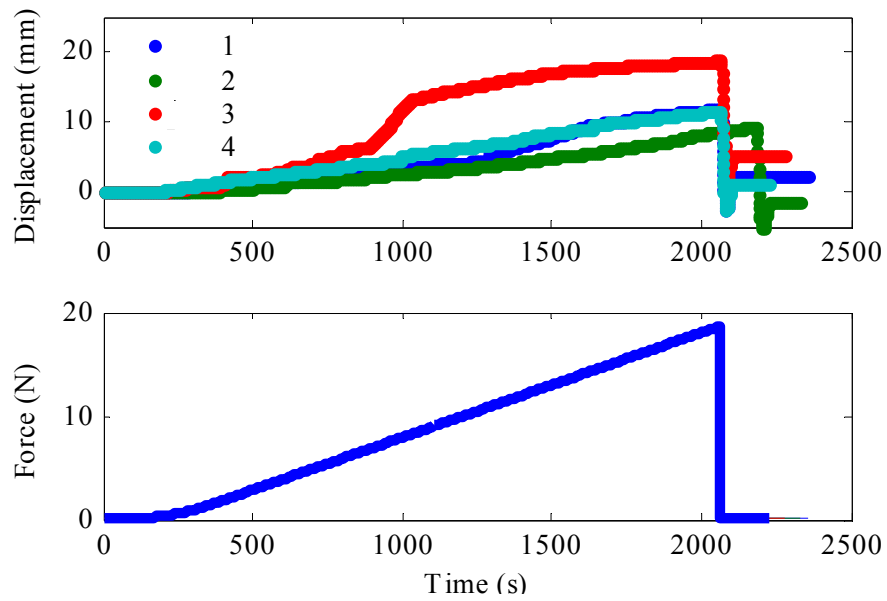


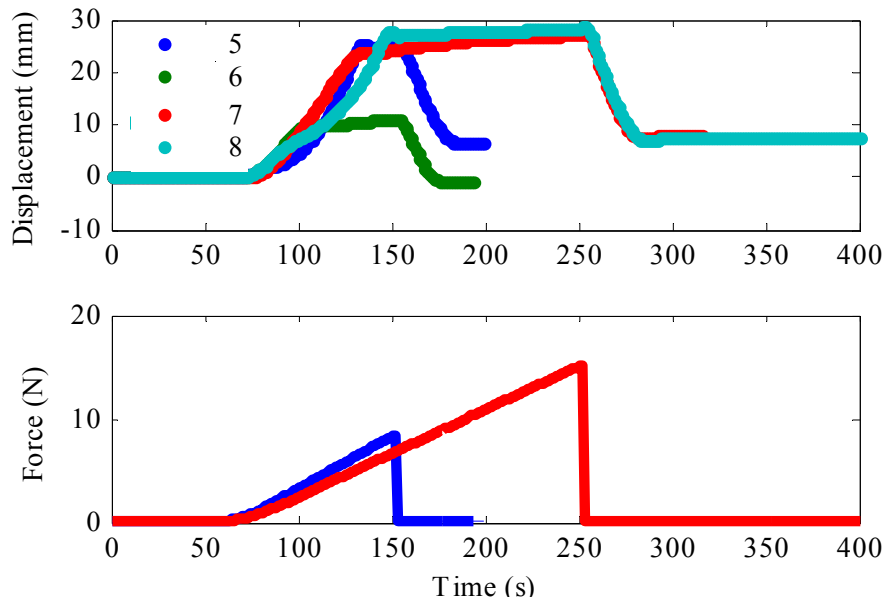
Figure 4.9 Calibration of the linear motor on the force-voltage relation.

Figure 4.10 shows the pulling deflection displacement and force profiles for two groups of samples. Due to the handling of the carcasses, some of the samples were broken before/during preparation. So two groups of samples are presented: samples 1 ~ 4 are intact clavicles; while sample 5~8 are half clavicles. As can be seen in Figure 4.10(a), all samples (1~4) deforms within the strength; while the horizontal parts in Figure 4.10(b) indicate the clavicles are broken and the breaking strength is estimated as about 6N.

Figure 4.11 and Figure 4.12 compare relations between the pulling force and the tip deflection from simulation and experiment. The elastic modulus for all eight samples can be obtained with average value of 2.7816 ± 1.1803 GPa. Errors can be introduced by defects occur in the sample preparation. Figure 4.12 also shows that the clavicles broke progressively so that the elastic modulus changed nonlinearly with increasing pulling force.

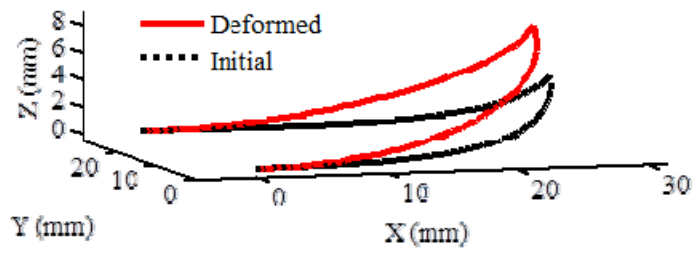


(a) Full clavicles.

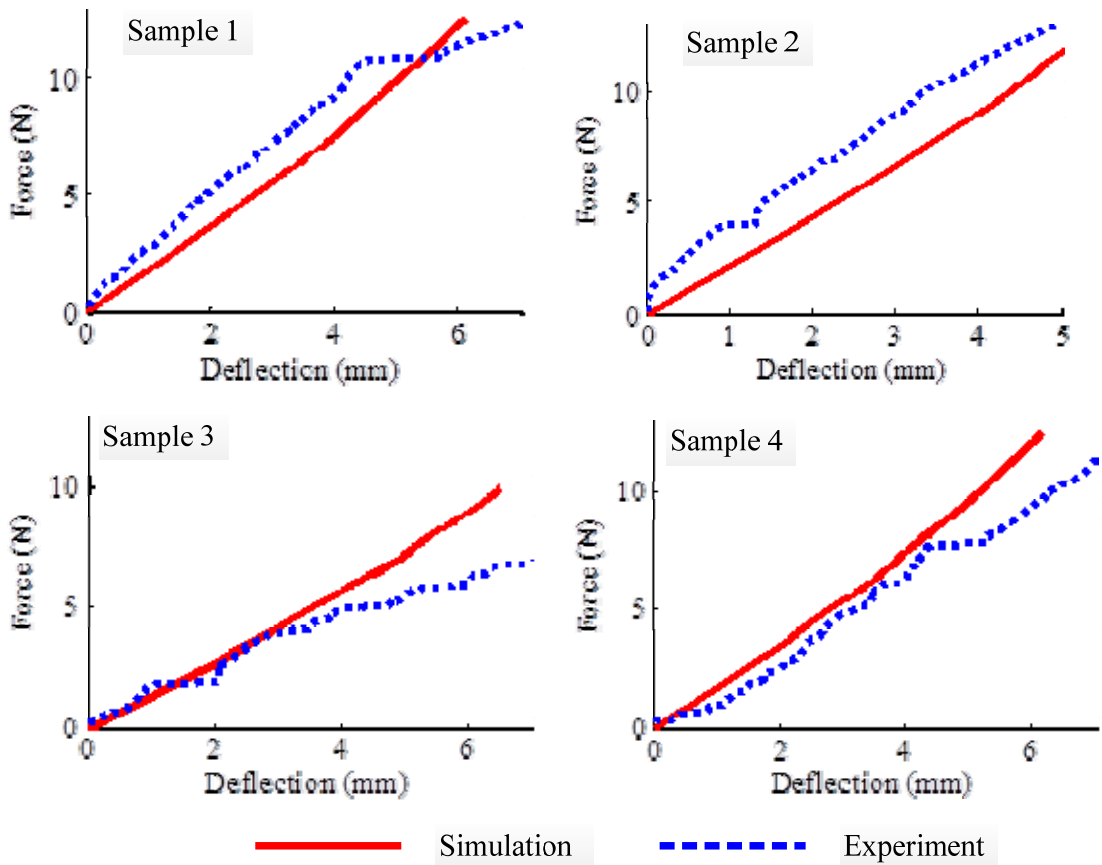


(b) Half clavicles.

Figure 4.10 Relation between pulling force and deflection on clavicles.

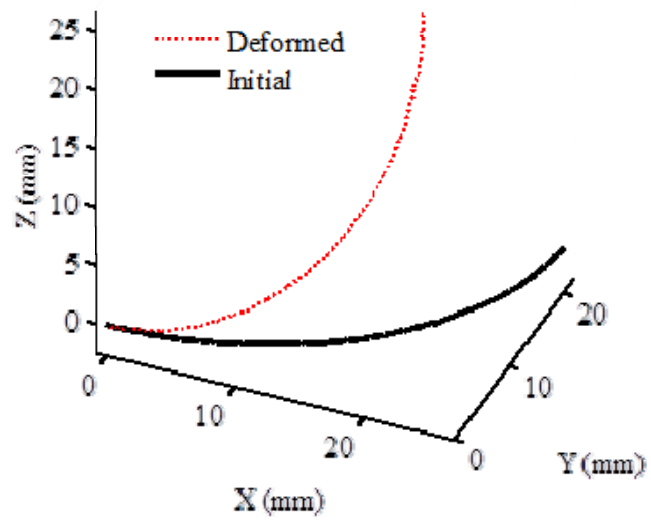


(a) Initial and deformed shapes

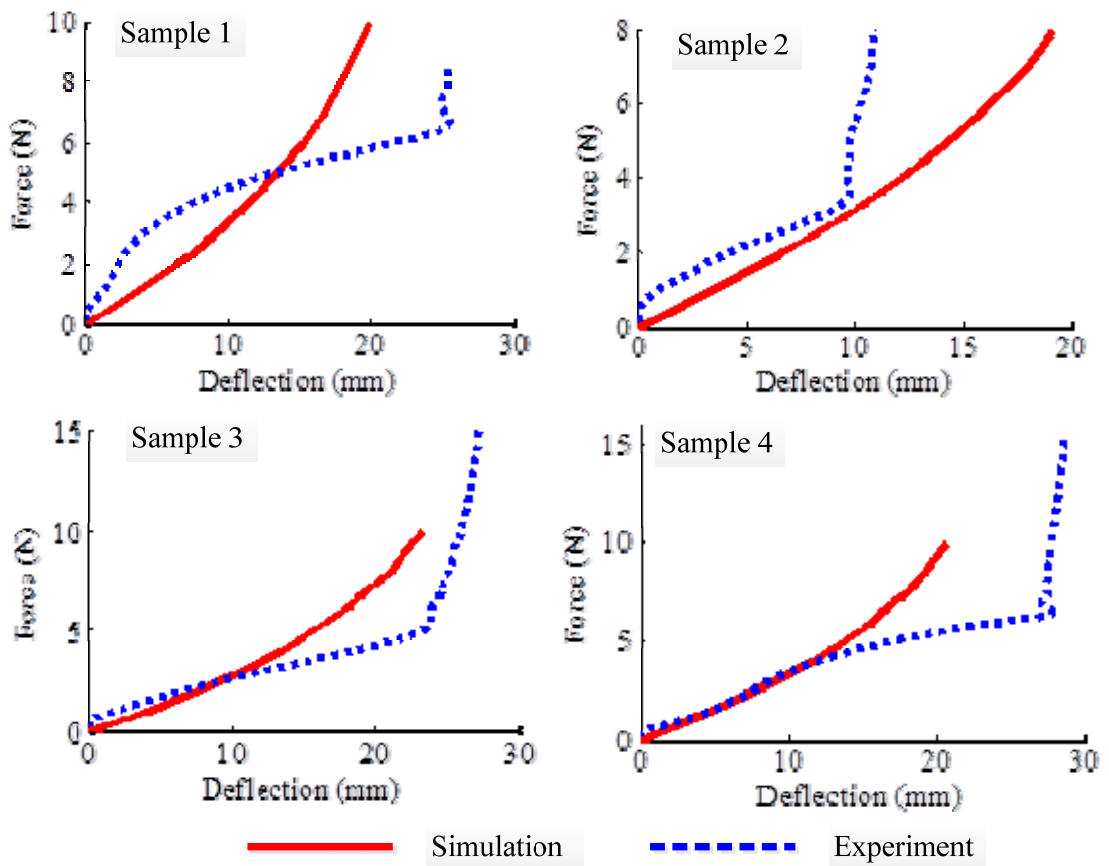


(b) Comparison of simulation and experiment

Figure 4.11 Tests on samples of full clavicles.



(a) Initial and deformed shapes



(b) Comparison of simulation and experiment

Figure 4.12 Tests on samples of half clavicles.

4.2.2 Ligament mechanics

To determine the manipulating trajectory and appropriate forces for presenting the ligaments to the cut, the ligament mechanics are modeled as a non-linear spring in the form suggested by (4.15) and validated against published data [46]. As shown in Figure 4.14(a), the coracohumeral ligament was chosen as the test sample due to its size, location, and ease of singulation. The other major ligaments are in locations difficult to remove without damaging the ligament itself. In an effort not to alter the ligament characteristics, the ligament was not separated from either the humerus or the coracoid. By retaining the bone connection on both sides of the ligament, it is possible to apply a tension load to the sample without the problems that arise due to clamping of free ends of the ligament. Experimental data are obtained from uniaxial extension at constant pulling

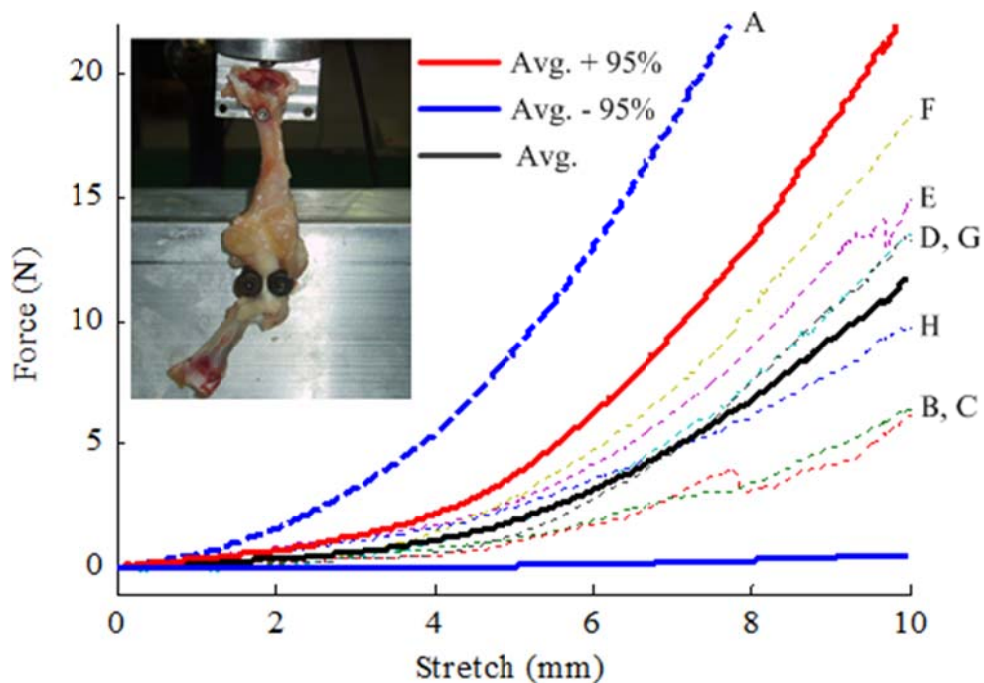


Figure 4.13 Uniaxial extension of ligaments [46].

velocity of 0.5mm/s on eight samples [46]: the cross section area is regarded as an ellipse and the dimensions (Table 4.2) are measured by a caliper; the ABB robot pulls the humerus at a very low constant speed of 0.5mm/s, so the tested sample can be regarded as quasi-static; the stretch is obtained from the multiplication of the pulling speed and the time, and the applying tensile force is measured by the force sensor. Figure 4.14(a) shows the experiment results of stretch and tensile force. Since the data of Sample A do not fall in the 95% confidence interval, this data is rejected and the average values together with $\pm 95\%$ variation are calculated based on the other seven samples. It is clear that data from biological objects have a very large variation (up to 50%) and the calculated results based on seven samples are

$$k_1 = 9.9246 \pm 1.9776, k_2 = 0.0027 \pm 0.0019$$

Table 4.2 Force sensor and sample dimensions.

ATI Mini 40 – US-5-10				
Maximum (N, N·m)		$F_{x,y} = 22.24$	$F_z = 44.48$	$T_{x,y,z} = 112.98$
Resolution (N, N·m)		$F_{x,y} = 0.0014$	$F_z = 0.0028$	$T_{x,y,z} = 0.0035$
Sample	A	B	C	D
A_0 (mm ²)	73.22	83.99	60.30	80.49
L_0 (mm)	20.60	22.06	18.69	21.59
Sample	E	F	G	H
A_0 (mm ²)	104.5	73.80	81.02	70.15
L_0 (mm)	24.60	20.70	21.67	20.16

*Average $A_0 = 69.04$ mm², $L_0 = 20$ mm.

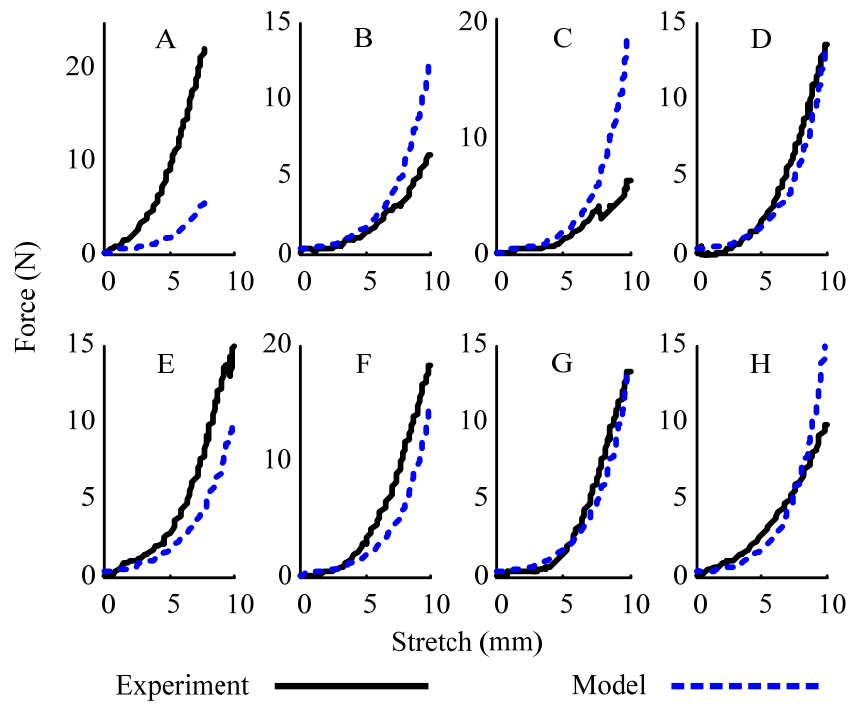
Figure 4.14(a) compares the force and stretch relations obtained from experiment and the proposed model (4.15) with nominal values $k_1 = 9.4377$ and $k_2 = 0.0025$. Given the large variations in Table 4.2 and Figure 4.13 among samples, the proposed ligament model agrees well with experimental data over a relatively large range of strain (about 0.5). The outlier of the first sample could be due to some unknown causes in the original data as indicated in Figure 4.13. One explanation would be that the bird was injured on the shoulder and the ligament become stiffer; similar things could have happened to samples E and F. Deviations in the sample B and C are due to the local damages of the fiber bundles during the extension. It is valuable to point out that models formulated with scalable variables, such as length or cross section area, can be accurately developed for a specific natural product by relating these scalable variables to its overall size or weight proportionally. Figure 4.14(b) compares the root mean square error in the applying force, with average value for the Sample B~H being about 1.6 N.

4.3 Illustrative Application to Wing Manipulation

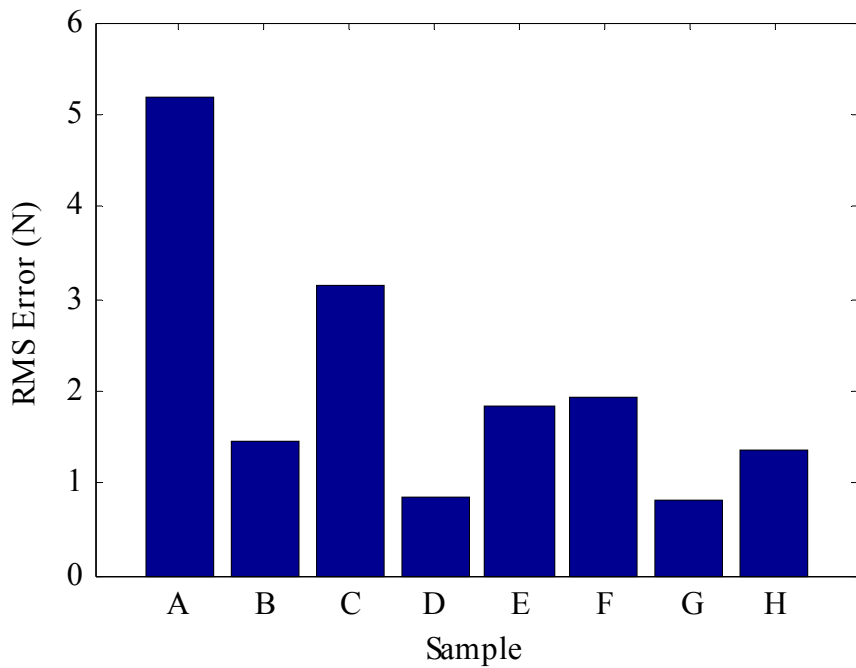
Applications of the proposed musculoskeletal model are illustrated using two wing manipulation examples:

Pulling $\delta = 10\text{mm}$ along the direction of $0.5Y-0.866Z$ defined in the reference frame OXYZ as shown in Figure 4.3.

Twisting $\theta = 90^\circ$ around the humerus longitudinal axis z_m .



(a) Comparison between experiment and analysis results.



(b) Comparison of root mean square error.

Figure 4.14 Ligament / tendon characteristic relation.

Table 4.3 lists the positions of all three ligaments and tendon, which are measured from a scanned geometry of a real chicken front-half. Since the ligaments/tendon are along different directions, the manipulator displacement is projected along L_i ($i = A, B$ and C) for estimating their individual elongations. The ligament forces f_i can then be calculated from (4.15); and their resulting force F_c and moment M_c can be applied to (4.6) to determine the shoulder displacements in the reference frame. As indicated from the simulation results, the pulling manipulation significantly tensions the ligaments A and C affecting the shoulder position in all directions, while the twisting motion mainly tensions ligament B and displaces the shoulder on the XY plane.

Table 4.3 Measured data and simulation results.

Ligaments	Attachment point	Vector L_i (mm)		Cross-section area A (mm ²)
A	-58.85, 19.72, 31.03	-7.23, 12.46, -19.02		69.04
B	-58.36, 14.81, 22.97	-7.8, 18.09, -5.46		50.68
C	-60.56, 16.14, -0.42	-3.59, 13.05, -0.77		22.29
<u>Pulling</u> $\delta = 10\text{mm}$	Ligament forces (N)	$f_A = 5.3$	$f_B = 2.1$	$f_C = 1.6$
	loadings on shoulder	$F_c = 6.2\text{N}$	$M_c = -0.011\text{N}\cdot\text{mm}$	
	Shoulder disp. (mm)	$u_X = 0.9$	$u_Y = 2.6$	$u_Z = 8.7$
<u>Twisting</u> $\theta = 90^\circ$	Ligament force (N)	$f_A = 0$	$f_B = 3.44$	$f_C = 0$
	loadings on shoulder	$F_c = 1.2\text{N}$	$M_c = -0.017\text{N}\cdot\text{mm}$	
	Shoulder disp. (mm)	$u_X = 0.5$	$u_Y = 1.4$	$u_Z = 0$

The wing manipulation tensions the ligaments and tendon to facilitate the cutting process. Once the stress within the soft tissues reaches a critical value, it is anticipated to be easily severed. Correspondingly there exists a critical strain from (4.12). Under assumption A3) in Section 4.1, this critical stress or strain would be the same for different birds because it is the mechanical property of soft tissues. However, (4.15) indicates that the applying force would be dependent on the cross-section area of soft tissues, A_0 , which is assumed to be proportional to the square of the overall bird feature dimension, such as the half shoulder width l_0 . As a result, if a bird size is 10% larger than the reference model size, the required force will become 21% larger.

On the other hand, the shoulder will displace and imprecise cut will occur due to error of blade insertion location as the wing is manipulated. Given the desired manipulating force, (4.6') can be used to predict the shoulder displacement. It is noted that x is proportional to l_0 , area moment of inertia I is on the order of l_0^4 . By analyzing each of the coefficients of F_c , M_c and k_m , it is found that they are proportional to $1/l_0$, $1/l_0^2$ and $1/l_0$, respectively, indicating that: effects of the meat deformation is independent on the bird dimension. However, the effects of the external loadings are dependent on the dimension variation: if the bird is 10% larger than the reference model size, the same pulling force will give rise to 11% reduction in shoulder displacement, while the same twisting moment will cause 23% reduction in displacement.

4.4 Summary

This chapter has discussed a dimension-based method to characterize bone and soft tissue deformation by accounting for the large size variation of natural products. A

compliant beam model is formulated for the clavicle bone deformation and a closed-form solution is obtained by assuming elastic foundation of breast meat. The solution is verified by the numerical MSM and an approximated polynomial solution is adopted for estimation of size variation effects on bone deformation. Analysis justifies this approach by showing that the approximation error vanishes as the external loadings increase. An exponential characteristic relation is used to capture highly nonlinear elastic property of soft tissues. Given the large variation of force profiles among specimens, the proposed model agrees well with experiment results. Finally, the musculoskeletal model is applied in wing manipulation to analyze the effects of size variation on required manipulating force and shoulder deformation. This musculoskeletal model can be potentially used to develop design criteria to automate the process of de-boning chicken breast-meat. While this chapter is written in the context of poultry meat de-boning, the method can be used in other bio-tissues, joints, and systems.

CHAPTER V

DESIGN OF COMPLIANT MECHANISM FOR A FLEXONIC MOBILE NODE

The 3-D deformation of a flexible beam subjected to generalized constraints was formulated in Chapters II and III, and extended to the analysis of a bio structure presented in Chapter IV. This chapter will apply the modeling method leading to the development of a bio-inspired compliant mechanism for a flexonic mobile node (FMN). In operation, the FMN utilizes large deflection and buckling of a compliant beam enabling it to flexibly negotiate different kinds of obstacles (such as abrupt angle changes) commonly encountered in complex civil structures.

In this chapter, the design concept, modeling analysis and experimental validation of an FMN for maneuvering on ferromagnetic surfaces are presented. The remainder of this chapter starts with the design concept of a novel magnet-wheeled FMN to achieve two important functions (sensor attachment and corner negotiation) with a simple mechanism. Then, a normalized 2D quasi-static compliant beam model is formulated from the 3-D beam model to reduce the design criteria. Illustrative examples will be given to exploit beam buckling for SHM applications, the work starts from a conventional viewpoint of the load-displacement relation, and then evolves to the displacement-displacement relations. As will be shown, these forward and inverse models

provide the essential basis for the design and control of a FMN. Experimental validation will be performed on a prototype FMN developed at Georgia Tech [5]. Finally, functions requiring 3-D beam deformation will be simulated and discussed.

5.1 Design Concept

Figure 5.1 illustrates the design concept of an FMN consisting of four independently driven magnetic wheels housed in two assemblies (front and rear) connected by a compliant beam. Unlike a rigid car frame with a fixed distance between the front and rear axles, the front axle of an FMN can be bent relatively to its rear axle by deforming the compliant beam (with both of its ends fixed on the two rigid bodies at P_0 and P_1). This enables the FMN not only to function as an agile locomotion but also a sensor loader. It can be easily noticed that definitions of coordinate frames here are the same as in Figure 2.3. It is recalled that the local coordinate frames, “xyz” and “ $\zeta\eta\zeta$ ” (each with a subscript indicating its location along the beam path-length), are defined in the un-deformed and deformed configurations respectively. The nodal displacements u_s , v_s and w_s are along x_s , y_s and z_s axis directions respectively. When the beam cross section is rectangular, all the coordinates follow the right-hand rule with x_s and ζ_s assigned along the neutral axis of the beam, and z_s and ζ_s normal to the beam surface.

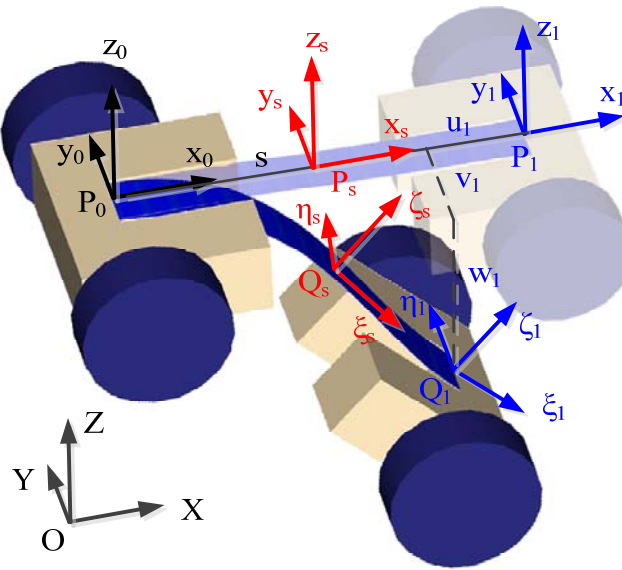


Figure 5.1 Design concept of an FMN.

With the specific SHM application in mind, this FMN is designed for field tests on the steel bridge on Georgia Tech campus as shown in Figure 5.2. Since the width of the bridge columns is about 140 mm, this dimension limits the overall FMN width and the compliant beam width. Besides, the motor output torque must be large enough to deform the compliant for different functions.

The first function is to attach/detach an accelerometer (mounted on a platform in the middle of the flexible beam) on/from the surface to be measured as shown in Figure 5.3. During the car-moving operation, the compliant beam is normally straight as shown in Figure 5.3(a). When a measurement is to be made, the two axles are driven towards each other to buckle the compliant beam as shown in Figure 5.3(b) allowing the accelerometer to be pressed against the surface to be measured.



Figure 5.2 A steel bridge on Georgia Tech campus.

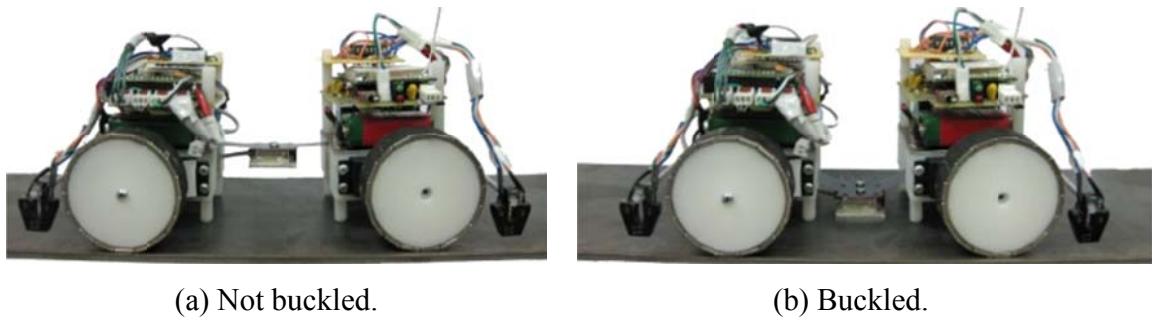
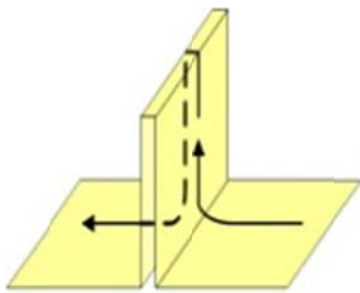


Figure 5.3 The compliant beam buckling.

The second function is to provide a means to overcome obstacles when navigating on a structure. Among the challenging obstacles is the crossing of a reinforcing ridge of small dimensions. As illustrated in Figure 5.4, the magnetic wheel must negotiate sharp corners. Magnetic forces at the corner greatly decrease when negotiating a concave corner, but increase (because of multiple contacts) when moving up or down a convex corner. Unlike a traditional design with a fixed distance between the front and rear

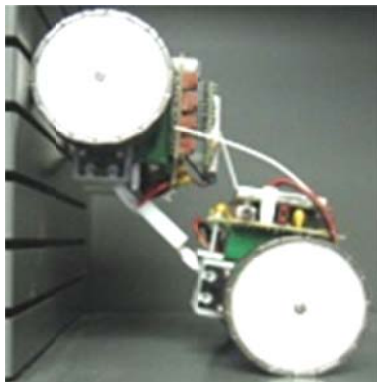
wheels, the compliant beam of the FMN can be shortened by buckling and thus can be designed to offer additional contact forces as needed by bending the connecting beam. Other challenges include a change in direction onto different surfaces as shown in Figure 5.5 and Figure 5.6, which require the compliant beam to twist in addition to bending. The ability to combine twist and bend enables the car to change directions across multiple orthogonal planes. Figure 5.5 shows an example where the car moves from the first plane by bending to the second plane, and immediately to the third plane by twisting since the second plane is too narrow to accommodate the whole car.



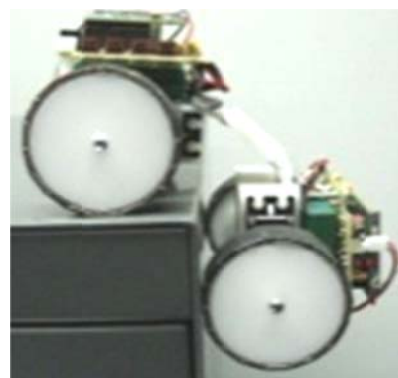
(a) Ridge.



(b) Crossing a ridge.



(c) Concave corner.



(d) Convex corner.

Figure 5.4 Compliant beam bending.

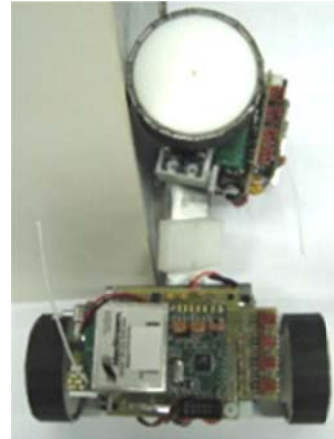
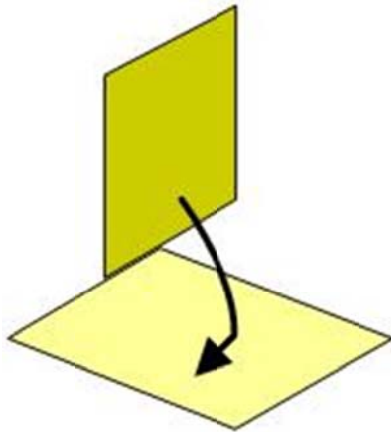


Figure 5.5 Twisting for a 90° direction change.

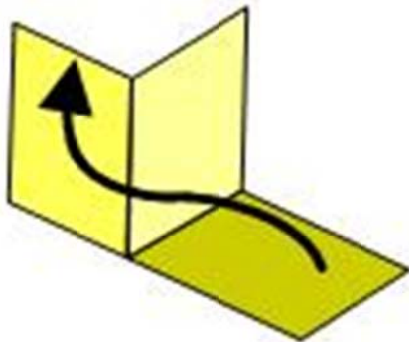


Figure 5.6 Twist / bend for direction change on different surfaces.

The functions illustrated in Figure 5.3 to Figure 5.6 require an appropriate loading specification to realize the bending and/or twisting in addition to the boundary conditions in formulating a compliant beam model to be discussed in the next section. It has been shown in Chapter II that the beam dimensions (cross section and beam length) explicitly appear in the constitutive equations, which characterize the beam load-deformation relations. So the next section will analyze the beam deformation when performing the two functions, sensor attachment and corner negotiation. Based on the analysis results, the beam dimension will be determined.

5.2 Compliant Beam Design


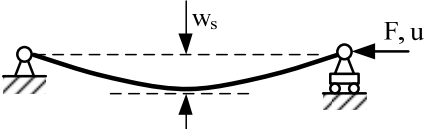
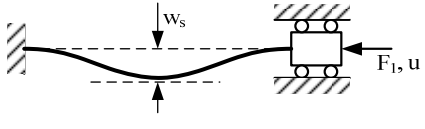
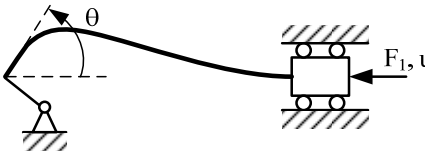
Following the formulation presented in Chapter II, appropriate boundary conditions must be specified to solve (2.24) for the thirteen unknowns in \mathbf{X} that are physically relevant. Table 5.1 summarizes four typical boundary conditions, which are also commonly specified for analyzing columns. For a cantilever (Type 1) where the slope and displacements are zeros at the fixed end, the forces and moments at the free end must be specified. For a beam with both ends constrained with pin-joints (Type 2), the displacement constraints cannot sustain any moment; $\mathbf{M} = 0$ but \mathbf{F} must be specified. As will be illustrated, Types 3 and 4 are specified for sensor attachment and for negotiating a convex corner, respectively. Type 3 is similar to Type 2 but can resist nonzero moments while maintaining zero slopes at both ends. In Type 4, a nonzero moment can be exerted against an offset pinned end. Unlike buckling analyses where the critical load causing a column to buckle is of particular concern, the models developed here relax several commonly made ideal-beam assumptions (such as mass-less and small deflection) for practical FMN applications.

The two basic functions of FMN have been simulated for design purposes:

- 1) The first function attaches/detaches an accelerometer on/from the surface to be measured. The compliant beam is normally straight. When preparing a measurement, the front axle is driven towards the rear axle buckling the compliant beam to press the accelerometer against the surface to be measured.
- 2) The second function provides a means to overcome obstacles when moving on a structure. Among the challenges is the ability to negotiate sharp corners. Magnetic forces at the corner greatly decrease when negotiating a convex corner, but

increase (because of multiple contacts) when moving up or down a concave corner.

Table 5.1 Boundary conditions for generalized constraints.

Type	$s = 0$	$s = 1$
 <p>1. Cantilever</p>	$R_{11} = 1, R_{12} = 0, R_{13} = 0,$ $\varphi = 0,$ $x_1 = x_1^{(0)}, x_2 = x_2^{(0)}, x_3 = x_3^{(0)}$	$F_1, F_2, F_3,$ M_1, M_2, M_3
 <p>2. Both ends pinned</p>	$x_1 = x_1^{(0)}, x_2 = x_2^{(0)}, x_3 = x_3^{(0)}$ $M_1 = M_2 = M_3 = 0$	$x_3 = x_3^{(0)};$ $F_1, F_2, F_3;$ $M_1 = M_2 = M_3 = 0$
 <p>3. Slide against a fixed end</p>	$R_{11}=1, R_{12} = R_{13} = \varphi = 0;$ $x_1 = x_1^{(0)}, x_2 = x_2^{(0)}, x_3 = x_3^{(0)}$	$R_{11}=1, R_{12} = R_{13} = 0;$ $x_2 = x_2^{(0)}, x_3 = x_3^{(0)};$ F_1
 <p>4. Slide against an offset pinned end</p>	$R_{11}=1, R_{12} = R_{13} = \varphi = 0;$ $x_2 = x_2^{(0)}, x_3 = x_3^{(0)};$ F_1	$x_1, x_2, x_3;$ M_1, M_2, M_3

For design purposes, the following normalized variables are applied to the beam equations (2.24):

$$F_i = \tilde{F}_i \frac{EI_2}{L^2}, \quad M_i = \tilde{M}_i \frac{EI_2}{L}, \quad q_{Fi} = \tilde{q}_{Fi} \frac{EI_2}{L^3}, \quad q_{Mi} = \tilde{q}_{Mi} \frac{EI_2}{L^2},$$

$$k_i^{(0)} = \tilde{k}_i^{(0)} \frac{1}{L}, \quad \kappa_i = \tilde{\kappa}_i \frac{1}{L} \quad \text{and} \quad x_i = \tilde{x}_i L$$

where L is the beam length. Then (2.24) is recast and the differentiation is carried out with respect to the normalized path length, $\tilde{s} = s / L$.

$$\tilde{F}'_1 = -\tilde{q}_{F1} \quad (5.1a)$$

$$\tilde{F}'_2 = -\tilde{q}_{F2} \quad (5.1b)$$

$$\tilde{F}'_3 = -\tilde{q}_{F3} \quad (5.1c)$$

$$\tilde{M}'_1 = -\tilde{q}_{M1} - (1 + \varepsilon)(R_{12}\tilde{F}_3 - R_{13}\tilde{F}_2) \quad (5.1d)$$

$$\tilde{M}'_2 = -\tilde{q}_{M2} - (1 + \varepsilon)(R_{13}\tilde{F}_1 - R_{11}\tilde{F}_3) \quad (5.1e)$$

$$\tilde{M}'_3 = -\tilde{q}_{M3} - (1 + \varepsilon)(R_{11}\tilde{F}_2 - R_{12}\tilde{F}_1) \quad (5.1f)$$

$$R'_{11} = \tilde{\kappa}_3 R_{21} - \tilde{\kappa}_2 R_{31} \quad (5.1g)$$

$$R'_{12} = \tilde{\kappa}_3 R_{22} - \tilde{\kappa}_2 R_{32} \quad (5.1h)$$

$$R'_{13} = \tilde{\kappa}_3 R_{23} - \tilde{\kappa}_2 R_{33} \quad (5.1i)$$

$$\varphi' = \tilde{\kappa}_1 + \tilde{\kappa}_2 \frac{R_{13}R_{32} - R_{12}R_{33}}{1 + R_{11}} + \tilde{\kappa}_3 \frac{R_{12}R_{23} - R_{13}R_{22}}{1 + R_{11}} \quad (5.1j)$$

$$\tilde{x}'_1 = (1 + \varepsilon)R_{11} \quad (5.1k)$$

$$\tilde{x}'_2 = (1 + \varepsilon)R_{12} \quad (5.1l)$$

$$\tilde{x}'_3 = (1 + \varepsilon)R_{13} \quad (5.1m)$$

where the longitudinal strain ε and curvatures $\mathbf{K}^{(e)}$ are calculated as follows

$$\tilde{\varepsilon} = \frac{I_2}{AL^2}(\tilde{F}_1 R_{11} + \tilde{F}_2 R_{12} + \tilde{F}_3 R_{13}) \quad (5.2)$$

$$\tilde{\kappa}_1 = \tilde{k}_1^{(0)} + \frac{EI_2}{GI_1}(\tilde{M}_1 R_{11} + \tilde{M}_2 R_{12} + \tilde{M}_3 R_{13}) \quad (5.3a)$$

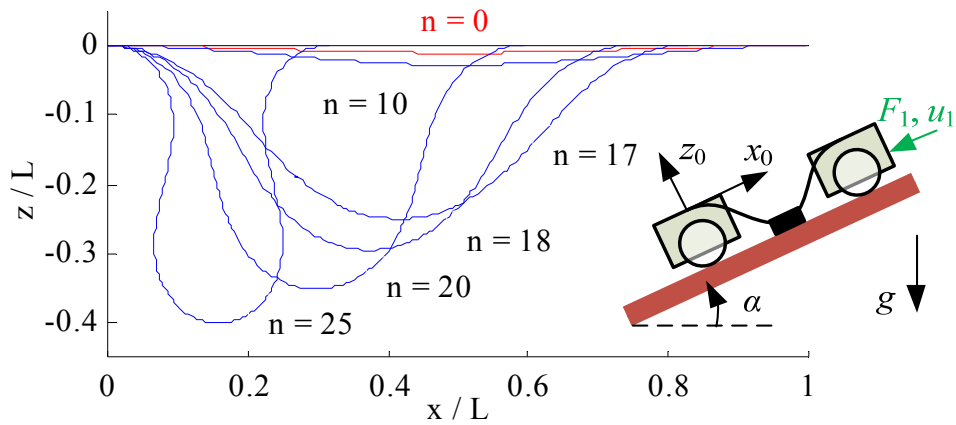
$$\tilde{\kappa}_2 = \tilde{k}_2^{(0)} + \tilde{M}_1 R_{21} + \tilde{M}_2 R_{22} + \tilde{M}_3 R_{33} \quad (5.3b)$$

$$\tilde{\kappa}_3 = \tilde{k}_3^{(0)} + \frac{I_2}{I_3}(\tilde{M}_1 R_{31} + \tilde{M}_2 R_{32} + \tilde{M}_3 R_{33}) \quad (5.3c)$$

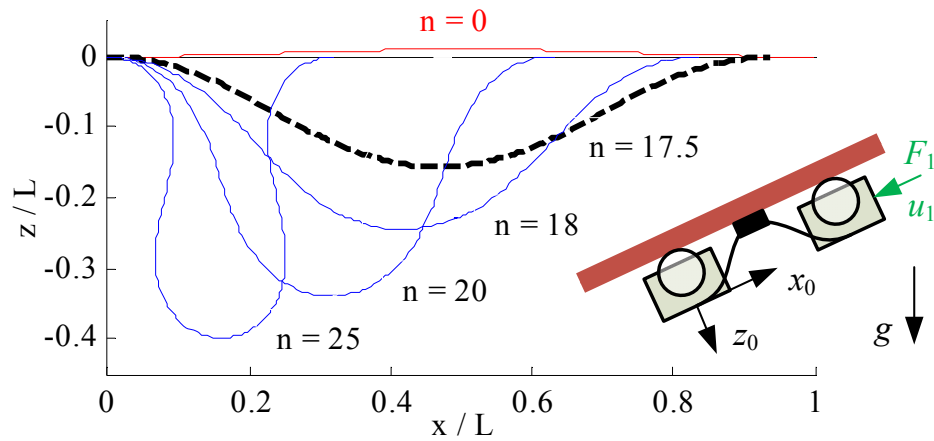
Numerical simulations using MSM (Appendix B) were performed, where computation time (especially when there is buckling) depends on the number of segments, N , and initial values for the iterative process. The MSM computation involves a $13(N+1) \times 13(N+1)$ matrix inverse. To reduce computation time, the beam is equally divided into three segments ($N = 3$, $m = 4$ in Figure B.1) with the beam cross-sectional area presented as a piecewise linear function of path length. As given in Table 5.1, some of the initial values are zeros. The remaining nonzero initial values are determined by physics. Consider a cantilever as an illustration, the values of F_1 and F_3 at $s = 0$ can be obtained from equilibrium; and M_2 can be chosen as the multiplication of the forces by a characteristic length (such as one half of the beam length).

5.2.1 Sensor attachment

In modeling the sensor attachment on a plane, the rear axle is treated as a fixed end, and the front axle acts as a slider subjected to a uni-axial loading F_1 as shown in Figure 5.7. In addition, it is assumed that the compliant beam is constrained to bend only in the $-z$ direction. For a given wheel radius, the uni-axial loading F_1 required to move the sensor to its desired displacement w_s (at $s = l/2$) depends on whether the direction of



(a) Case 1, $\alpha = 0$.



(b) Case 2, $\alpha = 0$.

Figure 5.7 Effect of gravity.

the sensor displacement is in the same or opposite to that of the gravitational force as compared in Figure 5.7. Unlike Case 1 where the weights of the sensor and beam facilitate the sensor attaching, the beam must compensate for these weights in Case 2. To explain the effect of the gravity, we normalize a force F to the critical buckling force for a beam subjected to both ends fixed [9] as follows:

$$n = F \left(\frac{4L^2}{\pi^2 EI_2} \right) \quad (5.4)$$

In the following simulation, the normalized gravity of the sensor which can be obtained by replacing $F = mg$ in (5.4) is 0.8. With Type 3 boundary conditions, the deformed shape (or w as a function of path length s) and $u_1 = x_1 - x_1^{(0)}$ can be computed by solving the BVP (2.26) by specifying F_1 . The results for the two cases (with $\alpha = 0$) are compared in Figure 5.7 and Figure 5.8 where the input force n varies from 0 to 25.

Some observations are discussed as follows:

Figure 5.7(a) and Figure 5.8(a) show that the beam deforms continuously as the normalized force increases in Case 1.

Although the carrying mass (normalized gravitation force 0.8) is relatively light causing negligible deformation under its own weight (red curves in Figure 5.7, $F_1=0$), this little weight however has a significant buckling effect on the beam in Case 2. As illustrated in Figure 5.7(b) and Figure 5.8(a), both the displacements (u_1 and w_s) in Case 2 do not change until the normalized force exceeds a critical value n_c at which the beam buckles drastically to a new shape (black dash curve in Figure 5.8b) without any intermediate shapes. The values of u_1 and w_s (corresponding to n_c for $\alpha = 0^\circ, 45^\circ, 90^\circ$) are summarized in Table 5.2 which also shows the effects of sensor weights on these values. These critical values that cause buckling to set off in Case 2 decreases (requiring less compensation against gravity) as α increases. For the same reason, a heavier weight tends to give rise to a larger critical value for $\alpha < 45^\circ$. On other hand, a smaller critical value for a lighter weight for $\alpha > 45^\circ$ is observed as gravity facilitates buckling.

Table 5.2 Slope angle and critical values.

Sensor gravity (normalized)	α (degree)	n_c	u_1 / L	w_s / L
0.8	0	17.5	-0.0624	0.1559
	45	16.9	-0.0612	0.1543
	90	15.5	-0.0002	0.0094
1.6	0	18.3	-0.0999	0.1948
	45	17.3	-0.1069	0.2009
	90	15.1	-0.00005	0.0001

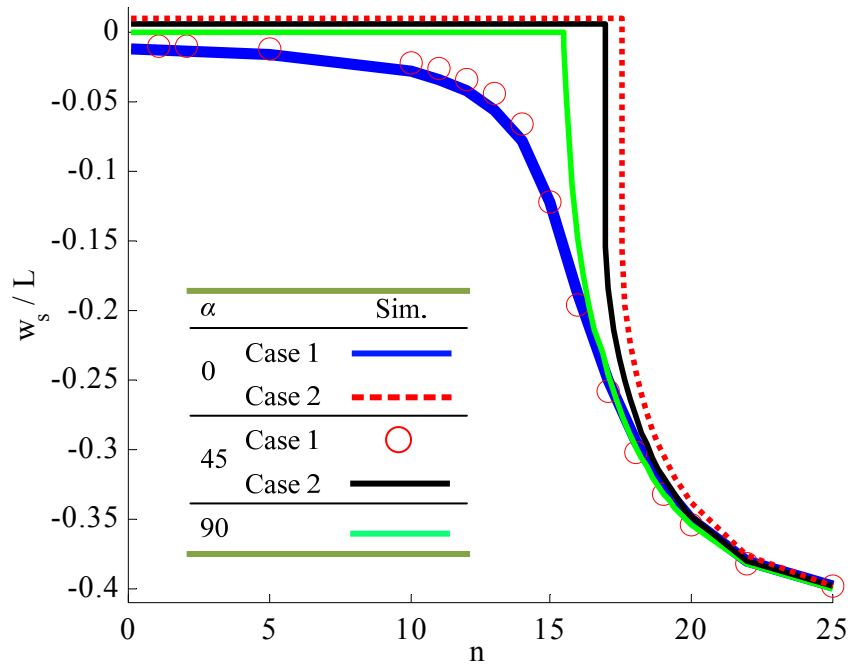
For $\alpha = 90^\circ$, the theoretical value of 16 given in [9] for a weightless beam is somewhat larger than n_c of 15.5. The beam model given in (5.1) accounts for the gravity along $-x$, which contributes to the onset of buckling.

The values of w_s for different α values converge to the case $\alpha = 90^\circ$ for large F_1 when the gravity becomes negligible. This is also true for u_1 because of the monotonous relation between w_s and u_1 as shown in Figure 5.8(b). The maximum normalized force required is $n = 25$, from which the required motor torque can be estimated by multiplying F_1 computed from (5.4) by the wheel radius r_w .

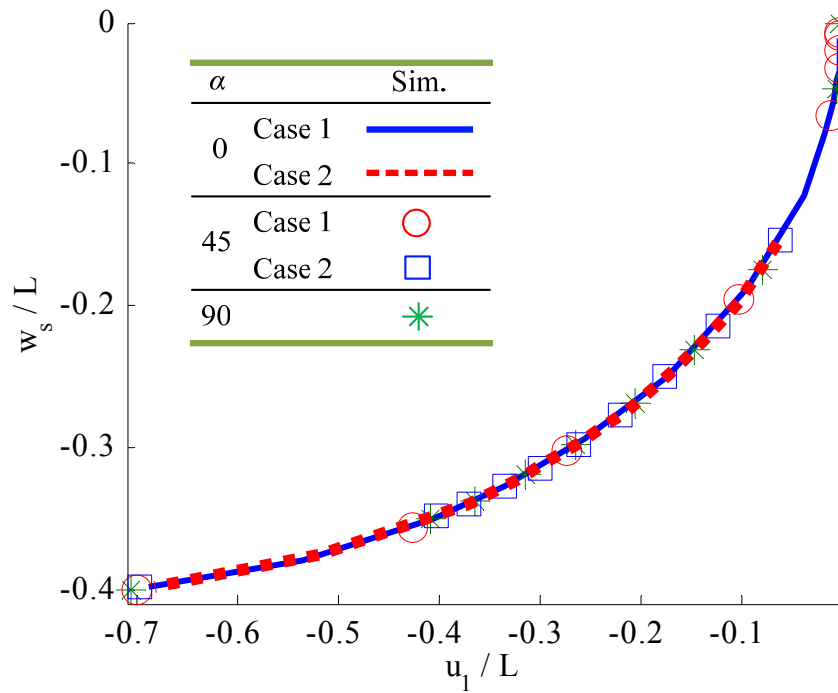
The inverse model that computes u_1 for a specified w_s for attaching the sensor is given by curve-fitting the data in Figure 5.8(b) for different α 's in both cases:

$$\frac{u_1}{L} = 18\left(\frac{w_s}{L}\right)^3 + 5.3\left(\frac{w_s}{L}\right)^2 - 0.85\frac{w_s}{L} \quad (5.5)$$

This result is due to the light weight of the combined beam and sensor. For detaching a sensor, the command becomes $-u_1$ for a reversed process.



(a) Relation between force n and displacement w_s/L .



(b) Relation between u_1 and w_s .

Figure 5.8 Relationship between normalized force and displacements.

The input displacement u_1 is a preferable manipulating variable for controlling the compliant beam of the FMN but not the input force F_1 . This can be explained by Figure 5.8 showing plots of the two manipulating variables (F_1 and u_1) and the sensor displacement w_s . As illustrated in Figure 5.8(a), the relationship between F_1 and w_s is not only highly nonlinear but also depends on α . On the other hand, the relationship between w_s and u_1 is monotonically smooth and independent of α as shown in Figure 5.8(b). Besides, for the feedback control purpose, displacements can be measured by simple encoders while forces are hard to obtain without expensive force sensors.

5.2.2 Convex corner negotiation

Figure 5.9 shows the free body diagram of the front assembly (mass m_1 at mass center C_1 and wheel radius r_w) at an instant crossing a convex corner A. The reference OXYZ is defined such that X is on the plane where the FMN initially locates and points

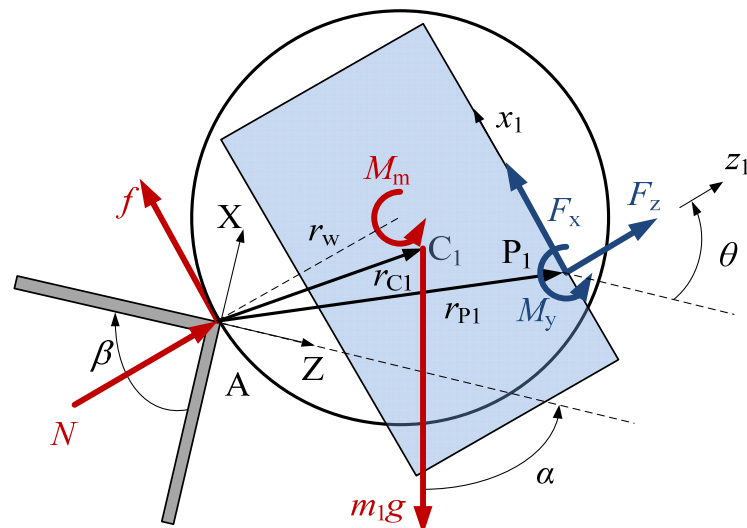


Figure 5.9 Convex corner negotiation.

in the moving direction before crossing the corner; and Z is normal to the plane. In Figure 5.9, α is the angle between Z and the gravity; N is the reaction force; and $f (= \mu N)$ is the friction; μ is the coefficient of friction between the wheel and surface; and τ_m is the torque provided by the motors.

The following assumptions are made in this discussion:

- 1) The wheels are designed with magnets such that they attach on the steel surfaces as the FMN moves.
- 2) The motor torque satisfies the non-slip condition: $\tau_m = f r_w \leq \mu N(\theta) r_w$
- 3) The moment due to the magnets is small as compared to that due to gravity, and thus neglected in the analysis.

The following discussion considers the worst scenario where the wheel has a point contact at the corner. The strategy for an FMN to negotiate a convex corner comprises three steps:

Step 1: The rear axle exerts the forces/torque (\mathbf{F} , \mathbf{M}) through the compliant beam to rotate the front axle about A.

Step 2: As soon as the front axle crosses over the corner ($\theta = \beta$ where β is the corner angle), the two assemblies move together.

Step 3: Once the rear axle arrives at the corner, the front axle pulls it over via the compliant beam.

The following details Step 1 as this initiation dictates the success of the corner negotiation. Figure 5.10 shows the beam deformations as the front assembly crosses the corner. As will be shown, the other steps follow similar principles.

To rotate the front assembly over the corner, the following condition with respect to A must be satisfied:

$$M_r \mathbf{E}_2 + \mathbf{r}_{C_1} \times m_1 \mathbf{g} \geq 0 \quad (5.6)$$

where M_r is the required moment in \mathbf{E}_2 to compensate for the torque due to gravity.

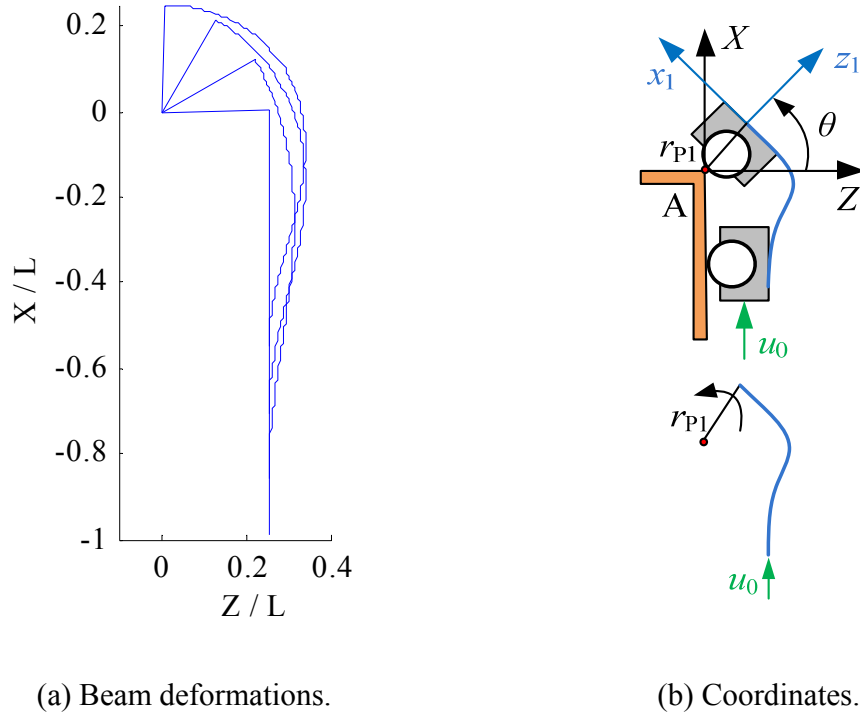


Figure 5.10 Simulation of corner negotiation.

The required moment can be calculated from the following equation with computed values shown in Figure 5.11 for different α values:

$$M_r \mathbf{E}_2 = \mathbf{r}_{P_1} \times (F_x \mathbf{E}_1 + F_y \mathbf{E}_2 + F_z \mathbf{E}_3) + M_y \mathbf{E}_2$$

For negative α , M_r can be obtained from the mirror images of Figure 5.11. Since the compliant beam attaches the front assembly at P_1 ,

$$\mathbf{F} = -[F_x \quad F_y \quad F_z]^T, \quad \mathbf{M} = -[M_x \quad M_y \quad M_z]^T \quad (5.7a,b)$$

The boundary conditions (M_2 , u and w) for negotiating a convex corner, which take the form of Type 4 in Table 5.1, can be obtained from (5.8) and (5.9):

$$M_2 = -\mathbf{E}_2 \cdot \mathbf{r}_{P_1} \times (F_1 \mathbf{E}_1 + F_2 \mathbf{E}_2 + F_3 \mathbf{E}_3) - M_r \quad (5.8)$$

$$\begin{bmatrix} x_1 & x_2 & x_3 \end{bmatrix}_{s=0} = \begin{bmatrix} x_1^{(0)} & x_2^{(0)} & x_3^{(0)} \end{bmatrix}_{s=0} + \begin{bmatrix} \mathbf{E}_1 & \mathbf{E}_2 & \mathbf{E}_3 \end{bmatrix} \begin{bmatrix} \cos \theta & 0 & -\sin \theta \\ 0 & 1 & 0 \\ \sin \theta & 0 & \cos \theta \end{bmatrix} \mathbf{r}_{P_i} \quad (5.9)$$

Solving (5.1) with (5.8) and (5.9) as constraints using MSM, the simulation results are given in Figure 5.12 showing the highly nonlinear relationship between θ and the applied force (for α equal to 0, $\pm\pi/4$, $\pm\pi/2$). The larger the α , the larger force required for a desired rotation angle and the maximum normalized force is about 4.5 (smaller than the maximum force of 25 for sensor attachment).

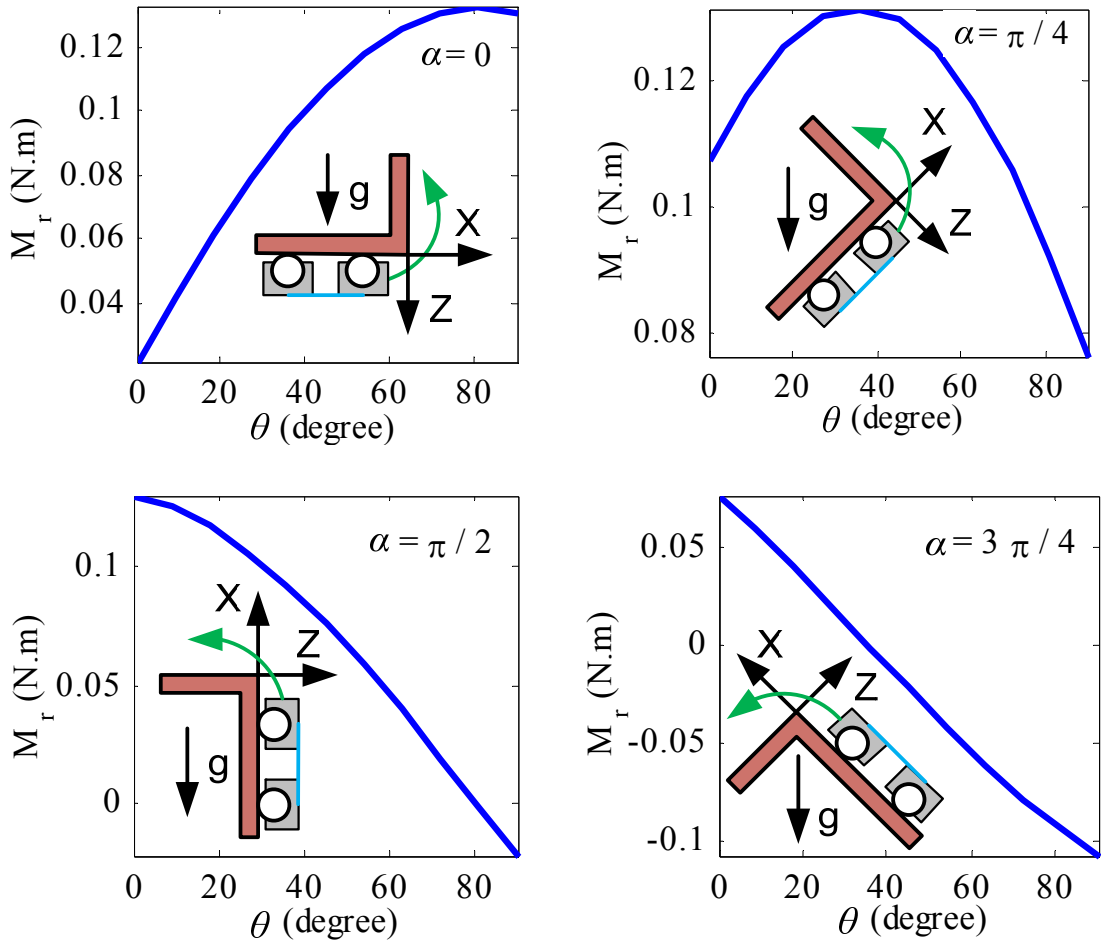


Figure 5.11 Relation between rotation angle θ and required moment M_r .

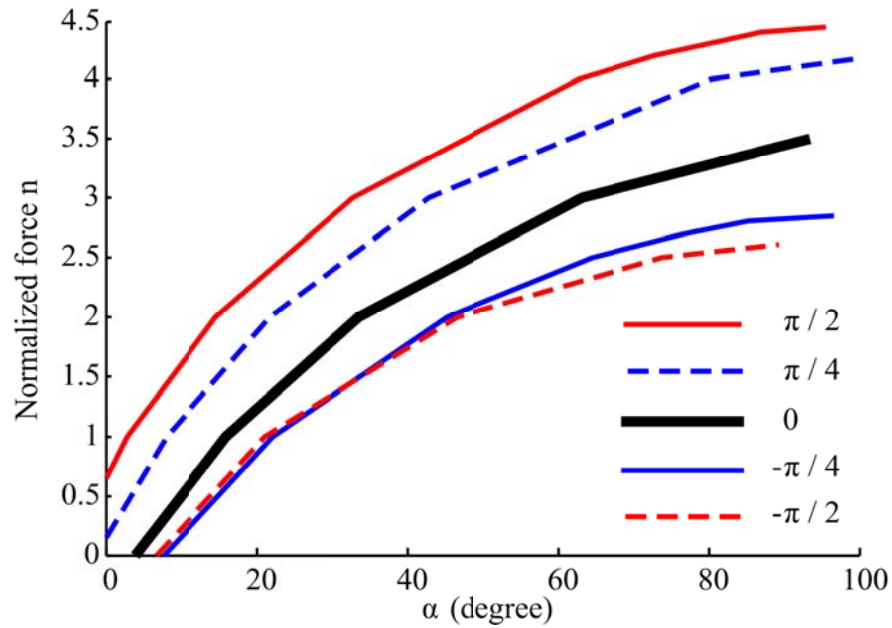


Figure 5.12 Relation between rotation angle α and normalized force n .

5.3 Experiments and Model Validation

Based on the previous analysis, the geometry of a compliant beam is designed and a prototype FMN has been fabricated as shown in Figure 5.13(a). It has two (front and rear) wheel-assemblies, each of which has a pair of magnetic wheels (independently driven by electric motors), a microprocessor-based pulse width modulation controller, and wireless communication circuits. The overall weight of the FMN is 1kg contributed primarily by the magnets, motors and batteries.

As illustrated in Figure 5.13(b), the main body of FMN consists two U-shaped structural frames on which the motors and electronics are housed and a spring steel (0.254mm thick) laminate including a compliant beam (shaded in gray). The non-shaded portions are fastened by screws onto the U-shaped frames. The accelerometer (50 grams) is pinned in the middle of the beam by screws (at locations shaded in black).

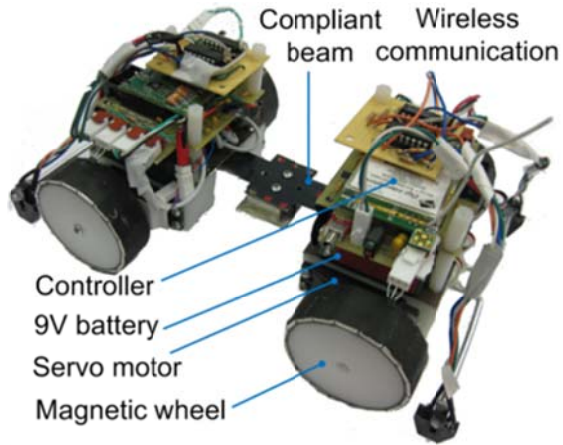
Specifications of the spring steel laminate are given in Figure 5.13(c) and Table 5.3. The beam has non-uniform cross-sections; thus A and I are functions of s .

Table 5.3 Mechanical properties and thickness of the spring steel laminate.

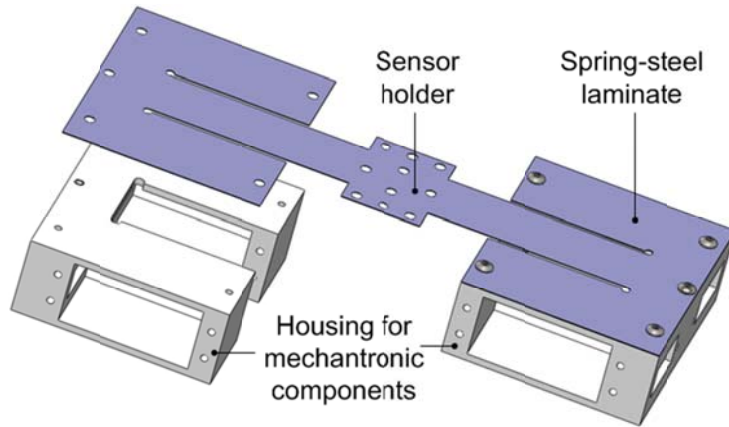
Elastic modulus E (GPa)	207	Density ρ (g / cm ³)	7.63
Shear modulus G (GPa)	79.3	Thickness h (mm)	0.254
Poisson ratio ν	0.3		

In the following, four examples are provided:

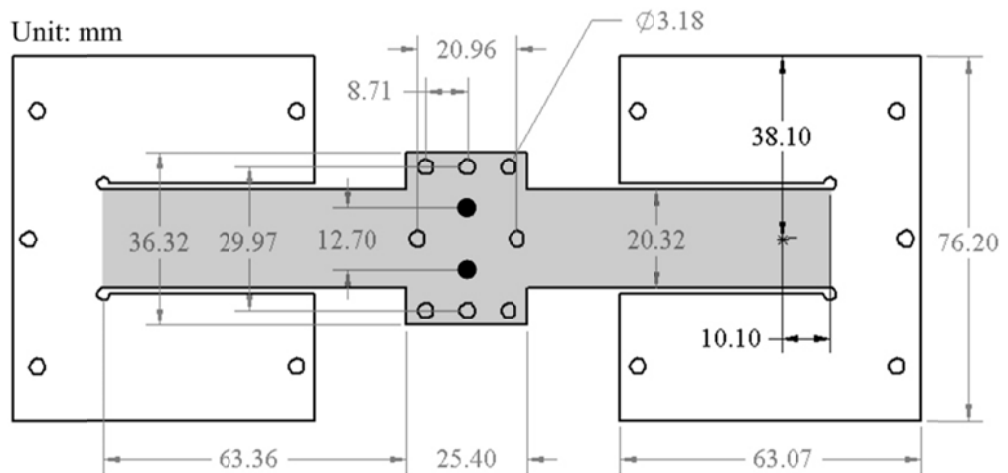
- 1) The first example is to validate the compliant beam model adopting the Euler beam assumption, where shears in cross sections are neglected. However, as can be noticed in Figure 5.13, a non-uniform beam shape has been designed for the application of sensor attachment with multiple screw holes in the sensor holder. The changes in cross sectional areas could potentially introduce shear deformation. So the simulation results will be compared against an cantilever experiment and FEM.
- 2) The second and third examples validate the analysis results of the compliant beam in sensor attachment and convex corner negotiation presented in Section 5.2. Simulation results are compared with experiment data collected from video images processing.



(a) Overview.



(b) CAD Model.



(c) Spring steel laminate.

Figure 5.13 Prototype FMN.

- 3) The last example of modal analysis shows the advantage of this FMN design over the previous MSN designed with rigid configuration in data collection for SHM. Vibration data of a laboratory steel frame are collected by both mobile sensors and their results from fast Fourier transform are compared against those predicted by FEM.

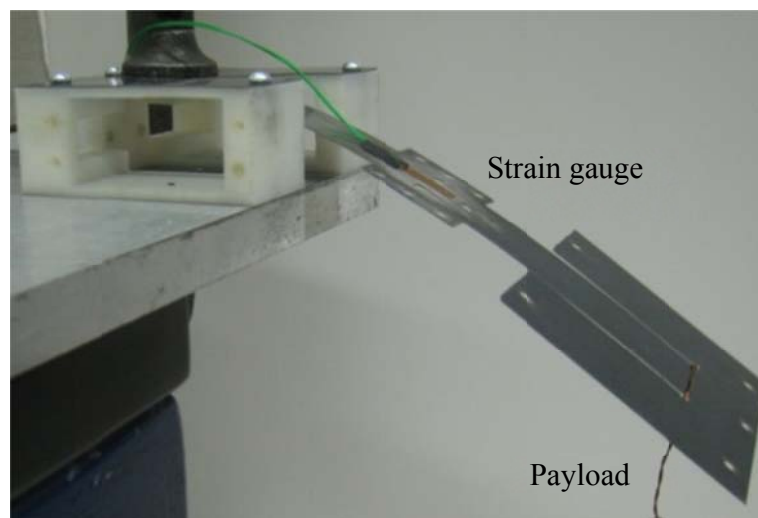
5.3.1 Validation of the beam model

Figure 5.14(a) shows the experimental setup to examine the validity of the beam model, where the spring-steel laminate on one of two housing structures (Figure 5.13(b)) was clamped as a cantilever, and thus has Type 1 constraints (Table 5.1). The remaining U-shaped portion (non-shaded in Figure 5.13(c)) in the spring-steel laminate serves as a load at the end of the compliant beam (that has a non-uniform shape and thus non-uniform distributed weight). As the mass center of this U-shaped portion is located at 10.1mm from the free end of the beam (Figure 5.13(c)), the weight of this U-shaped portion also contributes to a lateral force F_U and a moment M_U in addition to the external payload m_p at the free end of the beam. As a result, the values of \mathbf{F} and \mathbf{M} in the boundary conditions are given by

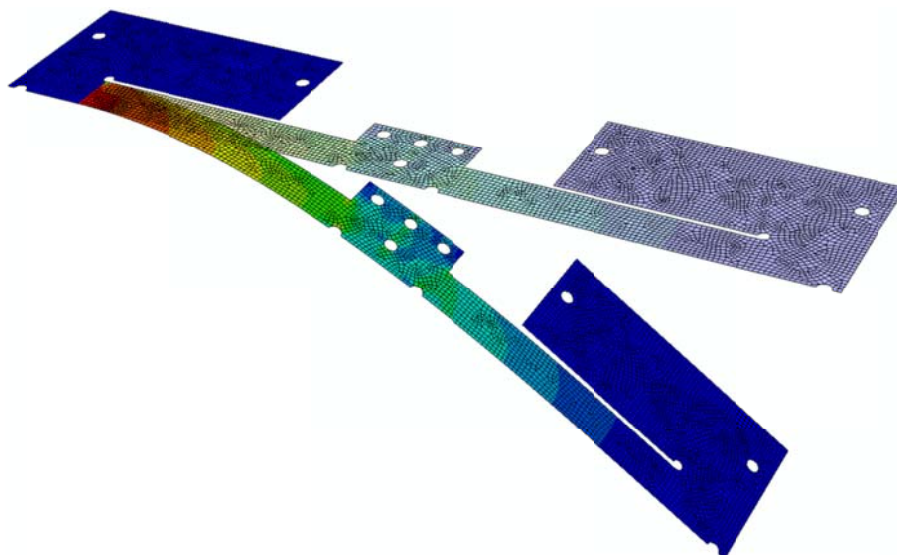
$$F_1=0, F_2=0, F_3=F_U+m_p g, M_1=0, M_2=M_U, M_3=0 \quad (5.10)$$

In this experiment, a strain gauge (with negligible weight as compared to the beam) was attached on the upper surface at the middle of the beam. To provide an alternative basis for comparisons, a numerical model was built in Abaqus using 6319 shell elements (S4R type). In FE analysis, only one-half of the beam is simulated because of symmetry, and the external load is applied at one coupling element so that F_U

is uniformly distributed over the cross section at the beam tip. All computations were performed on a computer with a 2.99 GHz CPU and 4.00GB memory; the FEM took about 365 seconds while the beam model (3-segment MSM) requires only 95 seconds. The analytical results are compared against those of FEM and experiments in Figure 5.15 and described as follows. The two beam models are uniform width of 20.32mm and non-uniform shape (that accounts for the geometry of the sensor holder).



(a) Experiment setup.

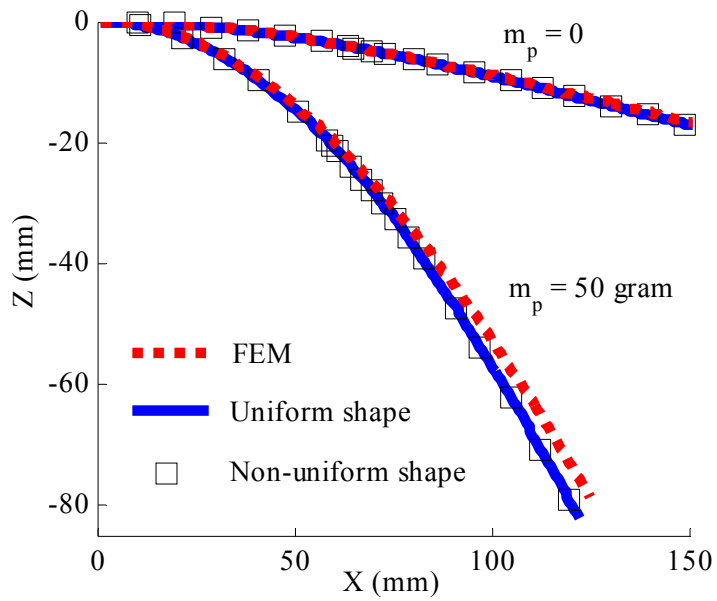


(b) Finite element analysis.

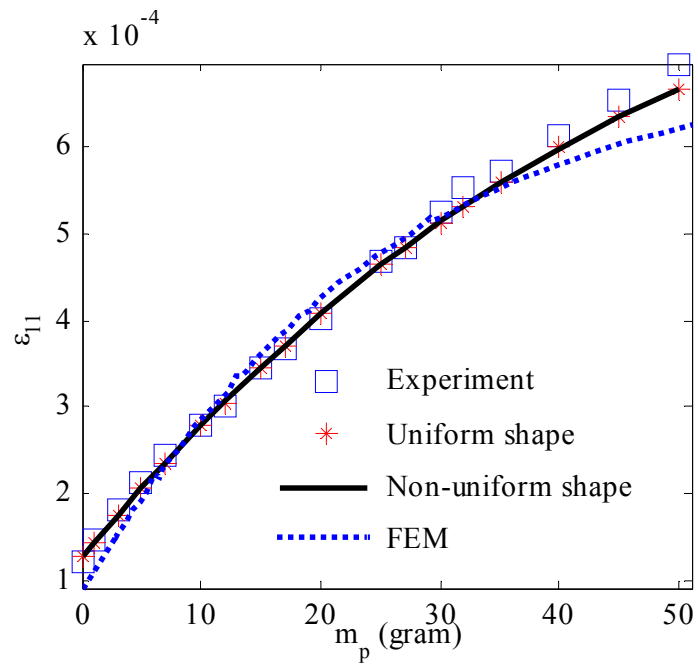
Figure 5.14 Validation of the beam model.

The results are discussed as follows:

- 1) Figure 5.15(a) shows that the FEM computed beam-shapes and the uniform/non-uniform beam models closely agree with each other for two different loadings; external payload $m_p = 0$ and 50 gram exerted at the beam tip. It is noted that the ten-hole area takes up to 8% of that of the sensor holder, which was compensated for by a function characterizing the change in beam widths; thus the results from two beam models, uniform and non-uniform shapes, do not differ significantly in this specific application.
- 2) Figure 5.15 (b) shows that the strain ε_{11} increases monotonically with payload. The beam model agrees well with the experimental measurements. Some discrepancies at large payloads are observed in FEM possibly due to the following local effects:
 - a. Because of FE meshes, the node at which strain information is extracted does not locate exactly at the middle of the beam.
 - b. Besides, the FEM model can capture the local stress concentration while the strain gauge is actually measuring the average strain over its area, and the stress concentration is not accounted in this beam model. When comparing this local information, the beam model matches with experiments but some discrepancy exists in the FEM.



(a) Comparison of deformed shapes.



(b) Comparison of upper-surface strains at the middle of the beam.

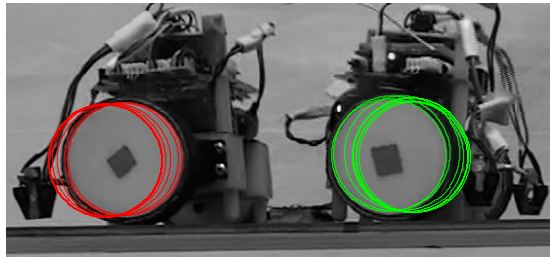
Figure 5.15 Model validation with FEM and experiment.

5.3.2 Effect of gravity on sensor attachment

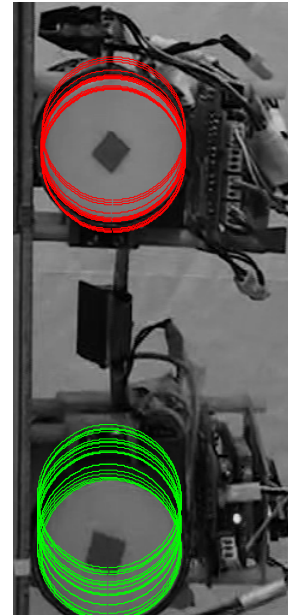
In this experiment, the sensor was attached on the plane by moving both axles towards each other to prevent slippage as shown in Figure 5.16(a-c). For comparing against analytical simulations where sensor attachments were modeled as a process of moving the front axle towards the fixed rear axle, the net displacement u_1 was obtained by measuring the distance change between the front and rear wheel centers from captured images. Figure 5.16(d) is a zoom-in comparison of Figure 5.8(b) showing good agreements between analyses and experiment results for $\alpha = 0, 45^\circ$ and 90° .

The results are discussed as follows:

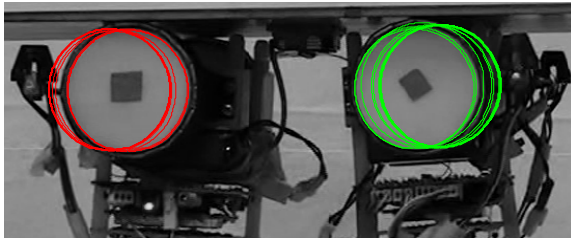
- 1) It is worth noting that the deviation in Case 2 for $\alpha = 0$ was a result due to the onset of buckling. Once the critical force is overcome, w_s / L jumps from zero to -0.1559 . This non-linear dynamic is essentially unstable. Thus, in Case 2, the required input displacement u_1 for $w_s / L > -0.1559$ is of the same value ($u_1 / L = -0.06$) as that when buckling starts.
- 2) However, all the intermediate experiment data follows the continuous curve given by (5.5) which is independent of slope angle α , so the relation between u_1 and w_s obtained from static analysis is also valid for the dynamic process of Case 2.
- 3) This also justifies for the conclusion obtained from Figure 5.8 to control the compliant beam deformation by manipulating the input displacement u_1 rather than the input force F_1 .



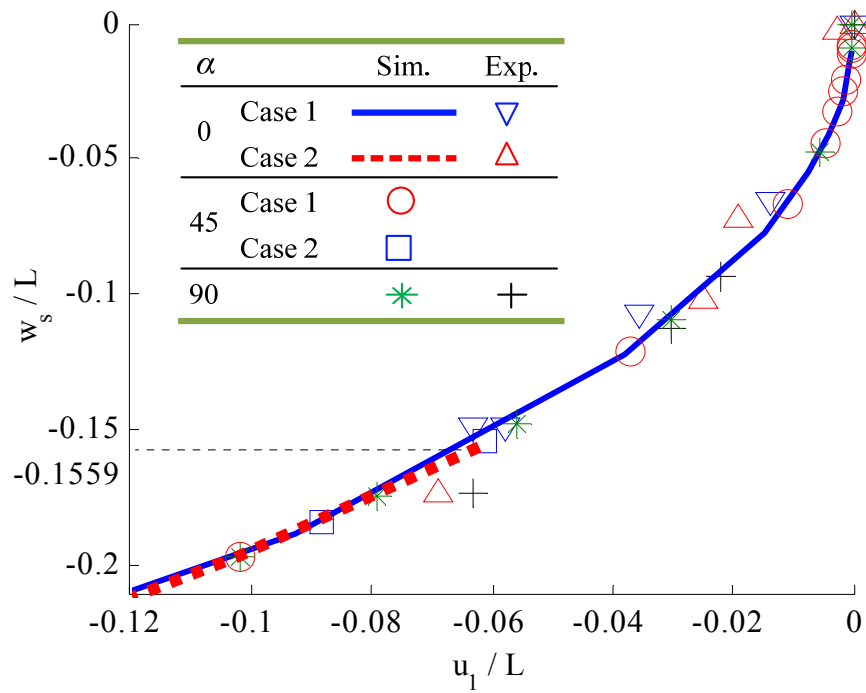
(a) Case 1: $\alpha = 0$.



(c) $\alpha = 90^\circ$.



(b) Case 2: $\alpha = 0$.



(d) Displacement comparison between simulation and experiment.

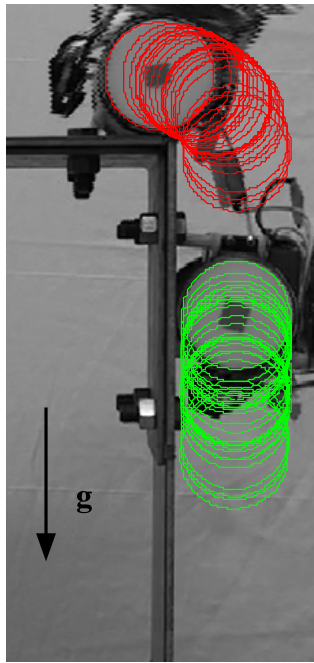
Figure 5.16 Validation of sensor attachment.

5.3.3 Validation of the corner negotiation

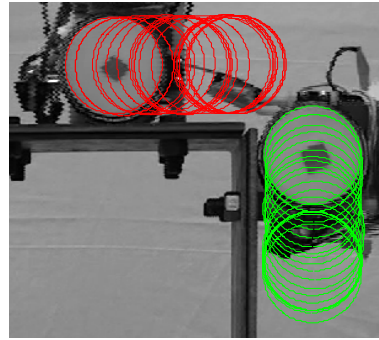
Figure 5.17(a-c) shows the three steps in negotiating a convex right corner, specifically pushing the front axle, both axles moving together and finally pulling the rear axle. Following the analysis before, the rotation angle α of the front axle is obtained by the orientation of the line connecting the front wheel center and the corner point, while the displacement u_0 of the rear axle is determined by the rear wheel center.

Observations are discussed as follows:

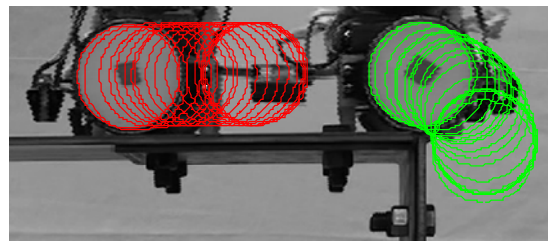
- 1) Although the relation between the applied force F_1 and the desired rotation angle α is nonlinear depending on the gravity direction, a highly linear relation $u_0 / L = 0.0051\alpha$ exists between u_0 and θ regardless of the gravity direction in simulation as shown in Figure 5.17(d). Experiment results also confirm with this linear relation.
 - a. It is noted that errors may come from the required torque that is calculated from the assembly mass and the distance from the corner to the mass center.
 - b. Another source of error can be the image processing of the video frames when detecting the front and rear axle locations by wheel centers, and determining the corner point by manually picking one pixel. Since the steel structure and the camcorder are fixed throughout the experiment, this corner point A is fixed in all the images while small vibration can exist in the steel structure because of the FMN dynamics.
- 2) It can also be seen that both the pushing and pulling process follows the same curve in experiment, implying the above analysis for the pushing process (Step 1) can be applied throughout the corner negotiation.



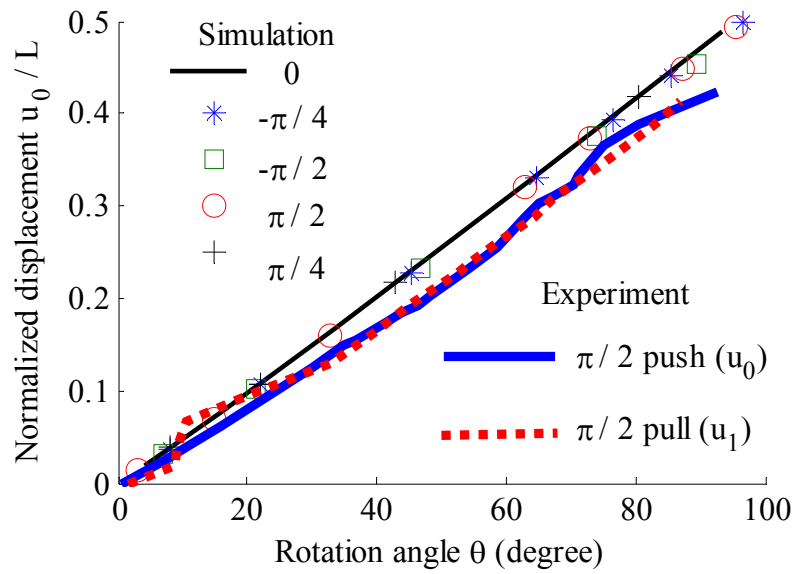
(a) Push the front axle.



(b) Move together.



(c) Pull the rear axle.



(d) Relation between rotation angle θ and displacement u_0/L .

Figure 5.17 Convex right corner negotiation.

5.3.4 Modal Analysis

In [65], a modal analysis of a frame structure (similar to Figure 5.18) was conducted with data collected from four mobile sensing nodes, where sensors were not in contact with the measuring surface. The modal analysis in [65] was limited to 50Hz due to the car dynamics of the mobile sensing node which essentially behaves as a low-pass filter. The interest here is to investigate the effect of sensor attachment on the modal analysis using impulse response studies. For this, vertical vibration data were obtained from both the 4-wheel magnetically driven FMN with a compliant beam, and the 3-wheel magnetic car of rigid configuration design [65] where the accelerometer (underneath the car) is not in contact with the surface. The accelerometer of the FMN is firmly pressed against the measured surface by the compliant beam and magnets as compared in Figure 5.19. As a basis for comparison, the fast Fourier transform results obtained from both measurements are compared against those predicted by FEM.

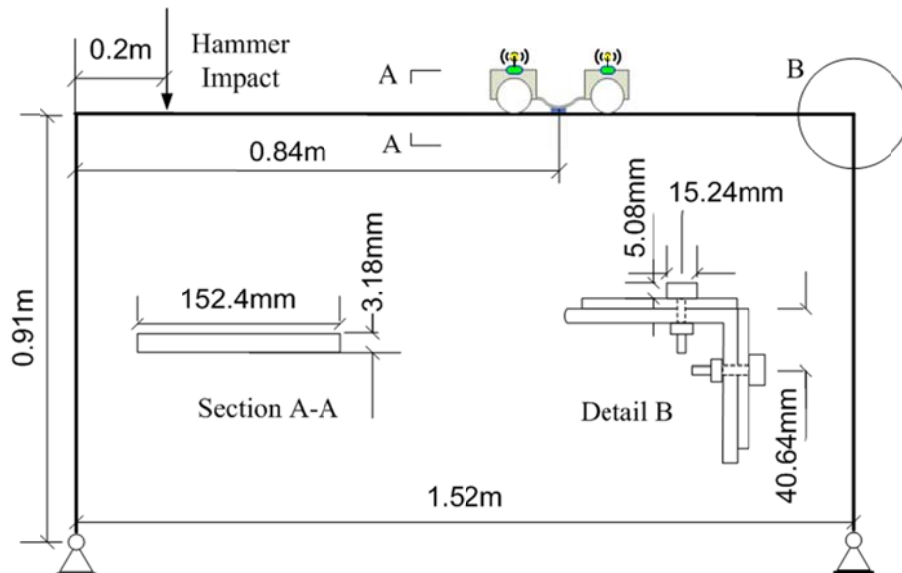
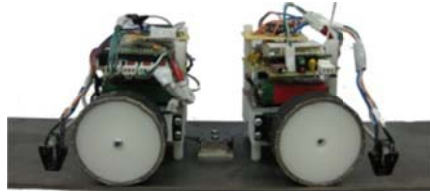
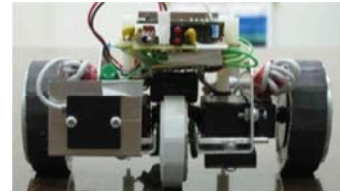


Figure 5.18 Steel frame structure.



(a) FMN.



(b) Single axle [65].

Figure 5.19 Comparison of FMN with rigid configuration design.

Table 5.4 Steel frame material properties and robot dimensions.

Material properties	Steel	Robot dimensions	
Elastic Modulus (GPa)	210	Length (cm)	20
Shear Modulus (GPa)	82	Width (cm)	14.7
Poisson ratio	0.28	Height (cm)	7.6
Density (kg/m ³)	7700	Weight (kg)	1

Sampling frequency = 500 Hz

Figure 5.18 shows a 2D laboratory steel portal frame structure (consisting of a beam and two column members) constructed for structural modal analyses. The beam is connected to the columns by bolted angle plates, and by hinge-connections at the column bases. Material properties for the frame structure are listed in Table 5.4 along with the dimensions in Figure 5.18. The two mobile cars are placed at the same position on the beam where vertical vibration data were collected after a hammer impact at a specified position. A sampling frequency of 500Hz is used for the data collection. The results comparing the vertical vibration data (in frequency domain) collected from the two cars are given in Figure 5.20 and Table 5.5.

Table 5.5 Comparison of frequencies.

FEM (Hz)	Compliant (Hz)	Single axle (Hz)
1.009		
4.626	4.5	4.7
10.757		
11.642	11.2	11.2
17.573	19.9	20.1
30.970	30.8	31.3
39.946		
40.679		
42.247	43.8	44.3
48.816	48.3	49.5
57.758	61.8	
79.232		
87.724	90.5	
94.619		
97.680	95.1	98.2
122.150		
123.130	123.3	124.2
146.640		

Some observations can be made from the results:

- 1) The dynamics of both magnetic cars has little influence on the vibration measurements in the lower-frequency range ($<50\text{Hz}$), and thus the results are closely matched with FEM results.
- 2) For this experiment configuration, the first vibration mode (horizontal) is not excited, so the lowest modal frequency is not identified. Also, since only one measuring point is considered in the experiment, some of the modal frequencies obtained from the FEM are not detected. Clearly, if this measuring point is at the zero vibration positions of certain modal shapes, the corresponding frequencies for these modal shapes cannot be captured at this point suggesting that multiple measuring points are necessary in practice.

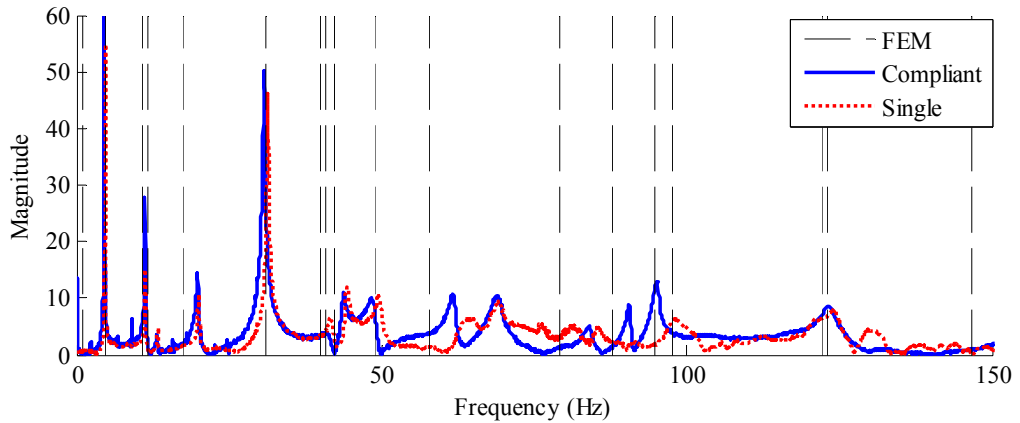
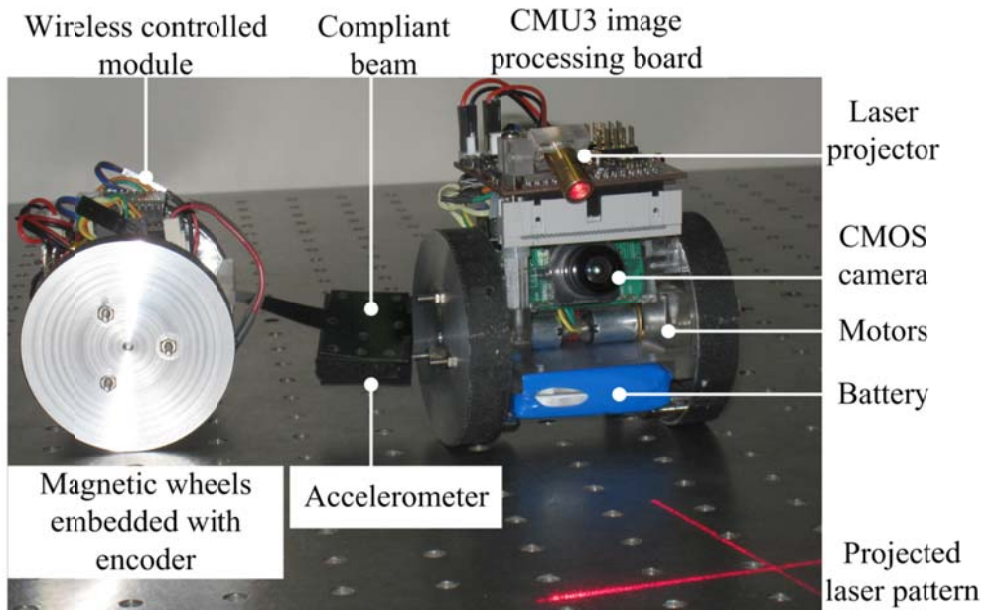


Figure 5.20 FFT of vertical vibration in the steel frame.

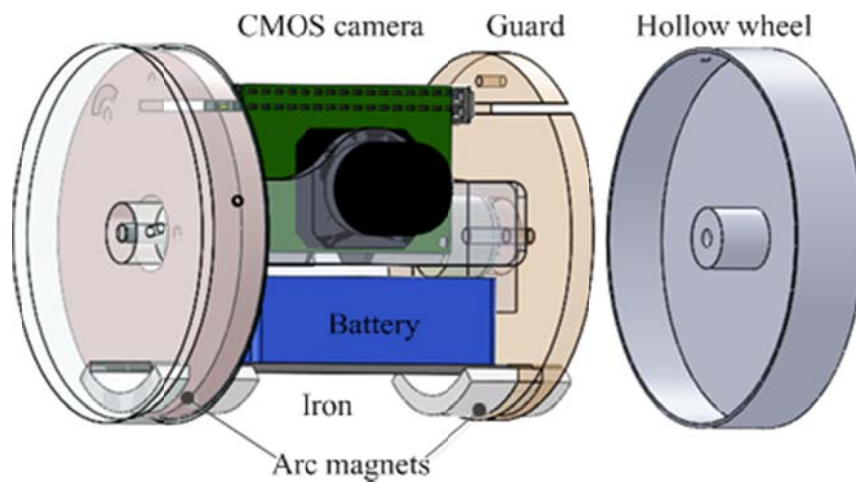
- 3) For frequencies larger than 50Hz, relatively sharp peaks can still be identified by the FMN because the accelerometer is firmly pressed against the steel frame structure eliminating the car dynamic effects on the measurements.

5.4 Applications with 3-D Deformation

Previous sections have designed the compliant mechanism and validated the beam model in experiment 2-D analysis. In the section, applications of FMN requiring 3-D deformation will be investigated in two illustrative examples, namely corner negotiation within limited space and environment monitoring. To facilitate the 3-D deformation, a modified FMN prototype equipped with a camera on the front axle is shown in Figure 5.21(a). The camera can capture terrain changes by monitoring distortion of the projected laser pattern. With this vision navigation system, the FMN is capable of detecting corner edges. Within each hollow wheel, a neodymium 90° arc magnet is fixed to the car body, hence does not rotate with the wheel (Figure 5.21b). Compared with design in Figure



(a) Overview.



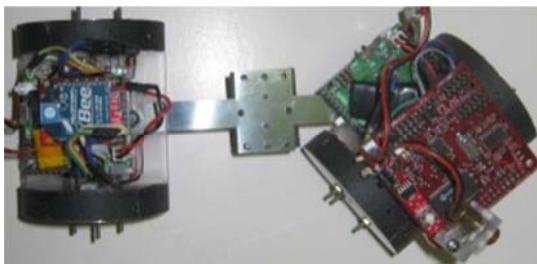
(b) CAD model.

Figure 5.21 Prototype of FMN with a camera.

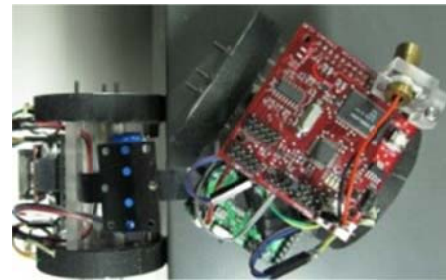
5.13(a) that 18 magnets are attached around each wheel, this configuration is featured with only one fixed magnet in each wheel and the light weight of 0.55 kg.

Besides, this modified FMN prototype is also featured with the front axle yawing as shown in Figure 5.22(a) and (b). To enable this DOF, the compliant beam is attached with the front axle via an on-off pin-joint. As shown in Figure 5.22(c), this pin joint is

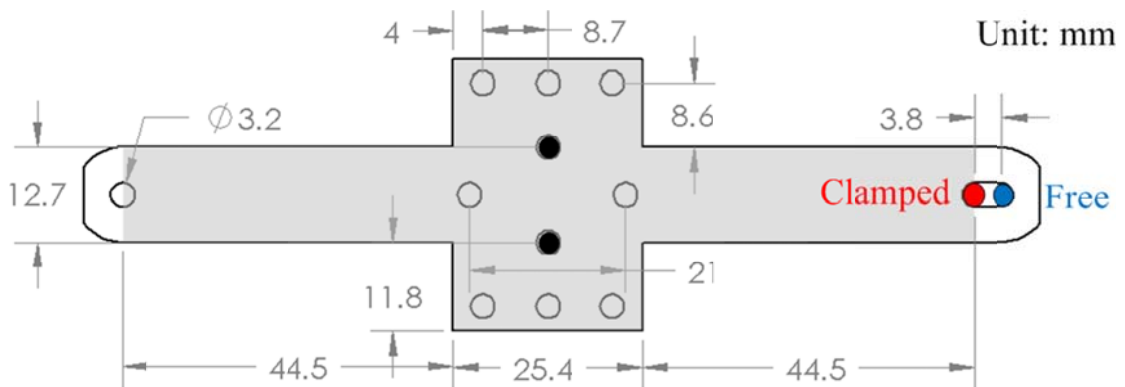
coupled with a linear slot, such that different boundary conditions are achievable based on the location of the pin axis (out of the paper) along the linear slot and the environment constraints. When the pin is located at the free location (blue), there is a gap between the front edge of the beam and back of the front assembly allowing free rotation between them like a regular pin joint. As the pin axis is at the clamped location (red), the front edge of the beam is pushed against the back of the front axle, rendering a locking state that is equivalent to fixed end boundary condition. Besides, an accelerometer is fixed on the beam at two holes marked as black, and the effective flexible portion of the beam is shaded.



(a) Turn on the same plane.



(b) Turn on another plane.



(c) Spring steel laminate.

Figure 5.22 Design of the compliant beam.

5.4.1 Corner Negotiation within limited space

Figure 5.23 shows an FMN at an instant crossing a convex corner A from Plane I to Plane II. Because of limited turning space, the FMN changes its initially aligned front and rear assemblies by turning the front assembly (mass m_1 at mass center C_1 and wheel radius r_w) and deforming the compliant beam. The reference XYZ is defined such that X is on the Plane I where the FMN initially locates and points in the moving direction before crossing the corner; and Z is normal to the plane. Similarly, X'Y'Z' is defined such that X' is along the final moving direction after crossing the corner; and Z' is normal to Plane II.

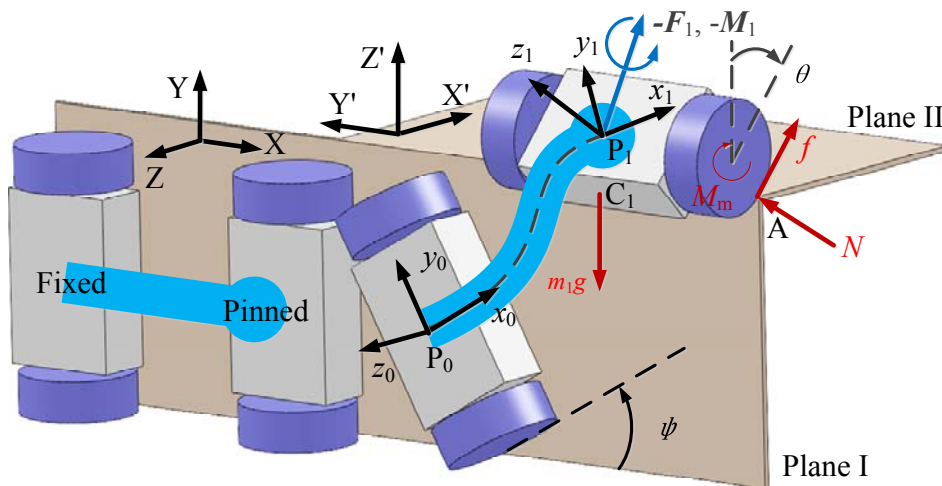


Figure 5.23 Turning within limited space.

The strategy for the FMN to negotiate a convex corner with limited turning space comprises three steps:

Step 1: The rear axle turns by ψ so that the front axle can approach the edge perpendicularly, where ψ is the angle between X and x_0 . Next the rear axle exerts forces/torque through the compliant beam to rotate the front axle about the corner A.

Step 2: The two assemblies move together as soon as the front axle crosses over the

corner.

Step 3: Finally, the front axle pulls it over via the compliant beam once the rear axle arrives at the corner.

As pointed out earlier, the mathematics illustrating Step 1 which dictates the success of the corner negotiation is further explained to gain intuitive insights.

For clarity, the following assumptions are made in this discussion:

- 1) The wheels are designed with magnets such that they attach on the steel surfaces as the FMN moves.
- 2) The motor torque M_m satisfies the non-slip condition:

$$M_m = f r_w \leq \mu N(\theta) r_w.$$

In Figure 5.23, N is the normal force; $f (= \mu N)$ is the friction; μ is the coefficient of friction between the wheel and surface; and M_m is the torque provided by the motors.

- 3) The moment due to the magnets is small as compared to that due to gravity and thus neglected in the analysis.

To rotate the front assembly over the corner, the inequality (5.11) with respect to the corner A must be satisfied:

$$|M_r \mathbf{E}_1 + \mathbf{r}_{C_1} \times m_1 \mathbf{g}| \geq 0 \quad (5.11)$$

where M_r is the required moment to compensate for the torque due to gravitational force and it is given by

$$M_r \mathbf{i}_{y'} = -\mathbf{r}_{P_1} \times \mathbf{F}_1 - \mathbf{M}_1$$

The boundary conditions for negotiating a convex corner, which take the form of Type 4 in Table 1, can be obtained from (5.12) and (5.13):

$$\mathbf{M}_1 = \mathbf{r}_{C_1} \times m_1 \mathbf{g} - \mathbf{r}_{P_1} \times \mathbf{F}_1 \quad (5.12)$$

$$\begin{aligned}
[x_1 \quad x_2 \quad x_3]_{s=1}^T &= [x_1^{(0)} \quad x_2^{(0)} \quad x_3^{(0)}]_{s=1}^T \\
&+ \begin{bmatrix} \cos \psi & \sin \psi & 0 \\ -\sin \psi & \cos \psi & 0 \\ 0 & 0 & 1 \end{bmatrix} \begin{bmatrix} 0 & 0 & 0 \\ 0 & 1 - \cos \theta & \sin \theta \\ 0 & -\sin \theta & 1 - \cos \theta \end{bmatrix} \mathbf{r}_P
\end{aligned} \tag{5.13}$$

Solving (5.1) with (5.12) and (5.13) as constraints using MSM, the results are given in Figure 5.24 and Figure 5.25 showing the deformed beam shapes and the highly nonlinear relationship between α and the applied force/displacement:

Figure 5.24 shows the snapshots of the deformed beam at different rotation angle θ , suggesting that large deformations of both bending and twisting occur on the beam. In simulating the corner negotiation, the rear axle pushes the front axle along the x_0 direction while maintaining ψ at a constant value of 30° so that the input force or displacement of the rear axle is along x_0 .

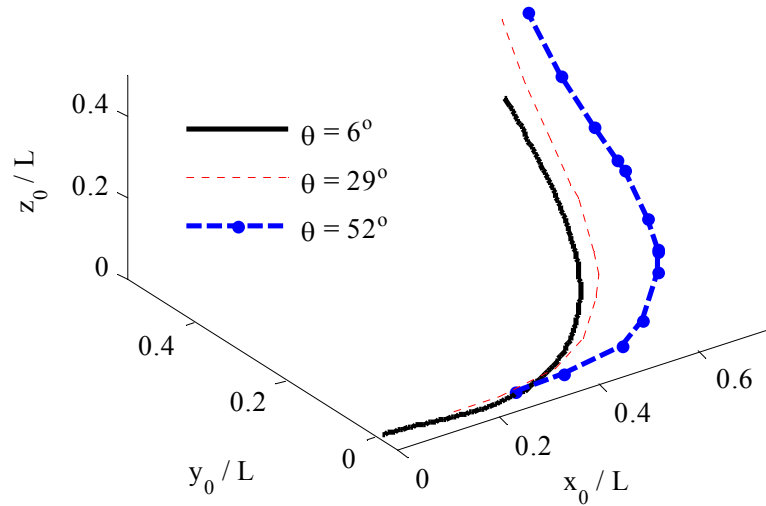


Figure 5.24 Snapshots of the deformed beam.

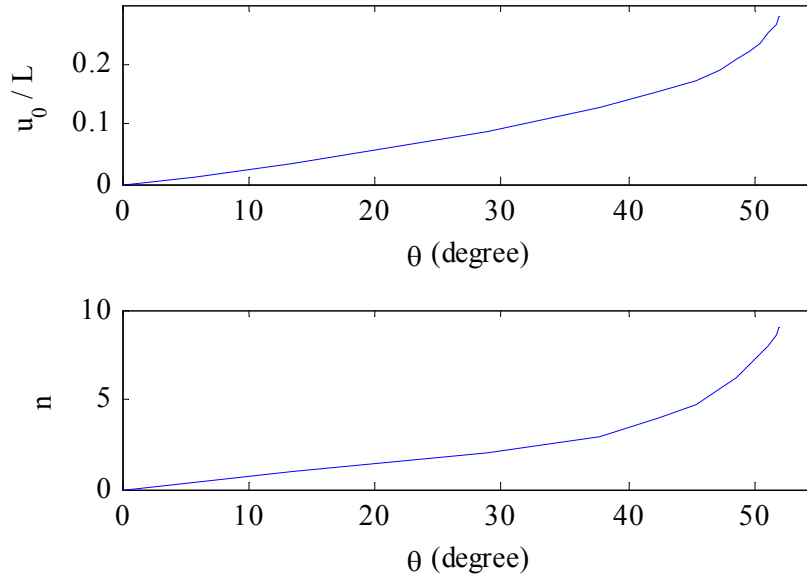


Figure 5.25 Normalized displacement and force.

In Figure 5.25, the normalized input force and displacement appear to be linear when $\theta \leq 45^\circ$. When $\theta > 45^\circ$, the inputs start to grow nonlinearly, implying certain geometry constraints may prevent the front axle to rotate further without extremely large forces. The displacement u_0 is given by:

$$\frac{u_0}{L} = \begin{cases} 0.0036\theta & \text{if } \theta \leq 45^\circ \\ 0.0016\theta^2 - 0.1431\theta + 3.3292 & \text{if } \theta > 45^\circ \end{cases} \quad (5.14)$$

In this way, the constant ψ strategy is invalid, or in other words, the rear axle should adaptively increase ψ as it approaches the edge in the perpendicular direction. This control strategy with variable ψ is worthy of investigation in the future.

Finally, the input-output relationship for corner negotiation within the limited space can be implemented as open-loop control in real time using (5.14). For closed-loop control, the displacement/orientation feedback can be achieved but requires additional sensors (such as rotary encoders or gyroscope) and will be left for future investigation.

5.4.2 Environment monitoring

As the FMN navigates on civil structures, it is necessary to monitor its surrounding environment to decide where the corners are and the location for placing the sensor for measurement. With implementing a camera on the front axle, it is desired to control the front axle yawing ψ and pitching θ as described with its rigid body attached frame $\{\mathbf{e}_{1f}, \mathbf{e}_{2f}, \mathbf{e}_{3f}\}$ in Figure 5.26. The front axle yawing can be controlled by the difference between the rotational speeds of its left and right wheels when releasing the pin joint on the front axle. On the other hand, as indicated in previous analysis the front axle yawing can be controlled by manipulating the compliant beam via the rear axle displacement u_0 . So this section will investigate the relation between u_0 and θ with different ψ .

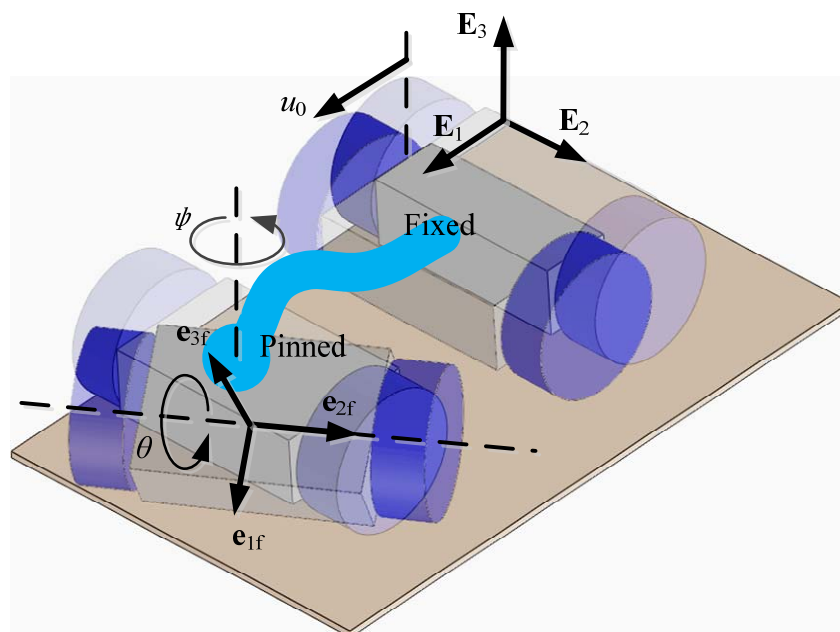


Figure 5.26 Front axle yawing and pitching.

Relation between the rigid body attached frame $\{\mathbf{e}_{1f}, \mathbf{e}_{2f}, \mathbf{e}_{3f}\}$ and the global reference frame is given by

$$\begin{Bmatrix} \mathbf{e}_{1f} \\ \mathbf{e}_{2f} \\ \mathbf{e}_{3f} \end{Bmatrix} = \mathbf{R}_\theta \mathbf{R}_\psi \begin{Bmatrix} \mathbf{E}_1 \\ \mathbf{E}_2 \\ \mathbf{E}_3 \end{Bmatrix} \quad (5.15)$$

where

$$\mathbf{R}_\psi = \begin{bmatrix} \cos \psi & \sin \psi & 0 \\ -\sin \psi & \cos \psi & 0 \\ 0 & 0 & 1 \end{bmatrix} \text{ and } \mathbf{R}_\theta = \begin{bmatrix} \cos \theta & 0 & -\sin \theta \\ 0 & 1 & 0 \\ \sin \theta & 0 & \cos \theta \end{bmatrix}$$

Then the position of the beam attaching point on the front axle is given by

$$\mathbf{x}_{p1} = x_t \mathbf{E}_i = r_w \theta \mathbf{e}_{1f} + \mathbf{r}_{p1}^T (\mathbf{R}_\theta \mathbf{R}_\psi - \mathbf{I}) + L \mathbf{E}_1$$

where the first term is the front axle forward motion because of pure rolling, the second term is due to the rigid body rotation with $\mathbf{r}_{p1} = [d_1 \ 0 \ d_3]^T$ being the beam attaching position on the front axle expressed in the frame $\{\mathbf{e}_{1f}, \mathbf{e}_{2f}, \mathbf{e}_{3f}\}$, and the third term is the initial straight beam length. Then the components of \mathbf{x}_{p1} in the global referenced frame can be expressed as

$$\begin{aligned} x_1 &= L + r\theta \cos \psi + [d_1(-1 + \cos \theta) + d_3 \sin \theta] \cos \psi \\ x_2 &= r\theta \sin \psi + [d_1(-1 + \cos \theta) + d_3 \sin \theta] \sin \psi \\ x_3 &= d_3(-1 + \cos \theta) - d_1 \sin \theta \end{aligned} \quad (5.16)$$

Different from previous analysis on corner negotiation, the front axle here is on a plane where the magnetic torque becomes dominant over the gravitational torque. Based on the equilibrium of the front axle in the \mathbf{e}_{2f} direction

$$\tau_m \mathbf{e}_{2f} = (r_w \mathbf{E}_3 + \mathbf{r}_{p1}) \times \mathbf{F} + \mathbf{M} \quad (5.17)$$

where $\tau_m = -k_\theta \theta$ is the magnetic torque with equivalent rotational spring constant k_θ ; \mathbf{F} ($= F_1 \mathbf{E}_1$) and \mathbf{M} ($= M_1 \mathbf{E}_1 + M_2 \mathbf{E}_2 + M_3 \mathbf{E}_3$) are respectively the force and moment exerted by the beam. From (5.15) and (5.17), the moment from the beam can be obtained as

$$\begin{aligned} M_1 &= k_\theta \theta \sin \psi \\ M_2 &= F_1 (r_w + d_z) - k_\theta \theta \cos \psi \\ M_3 &= 0 \end{aligned} \quad (5.18)$$

In the above, the pitching angle θ should be determined from the orientation of the beam attachment on the front axle. It is noted that $[\mathbf{R}]_1 = [R_{11} \ R_{12} \ R_{13}]$ in (2.16) is the tangential vector along the beam axis, and it lies in the plane of formed by \mathbf{e}_{1f} and \mathbf{e}_{2f} . Then \mathbf{e}_{3f} can be written as $\mathbf{e}_{3f} = [\mathbf{R}]_1 \times \mathbf{e}_{2f}$. Considering (5.15), θ can be determined as follows

$$\sin \theta = -R_{13}, \quad \cos \theta = R_{11} \cos \psi + R_{12} \sin \psi \quad (5.19)$$

By specifying the yawing angle ψ and the pushing force F_1 , the pitching angle θ and the rear axle position / displacement (assuming it starts from the origin of the global referenced frame, $u_0 = x_1|_{s=0}$) can be obtained by solving the BVP (2.26) with the boundary conditions determined as

$$\begin{aligned} s = 0: & \quad R_{11} = 1, R_{12} = R_{13} = \varphi = 0; x_2 = x_3 = 0; F_1 \\ s = L: & \quad x_1, x_2, x_3, M_1, M_2, M_3 \text{ given by (5.16) and (5.18)} \end{aligned}$$

Numerical values used in the simulation can be found in Figure 5.22(c), Table 5.3 and Table 5.6.

Table 5.6 Numerical values for simulation.

k_θ	d_1	d_3
0.69 N.m/radian	-21.79mm	7.11mm

Figure 5.27 shows the deformed beam shapes for several combinations of ψ and θ . The beam deformation is 2-D for $\psi = 0$ and 3-D for $\psi \neq 0$. It is noted that the beam deformation is symmetric for $\psi > 0$ and $\psi < 0$, so only the case of $\psi > 0$ is presented here. Besides, for $\theta < 0$ it requires the rear axle to push forwards ($u_0 > 0$) while for $\theta > 0$ the rear axle has to pull backwards ($u_0 < 0$).

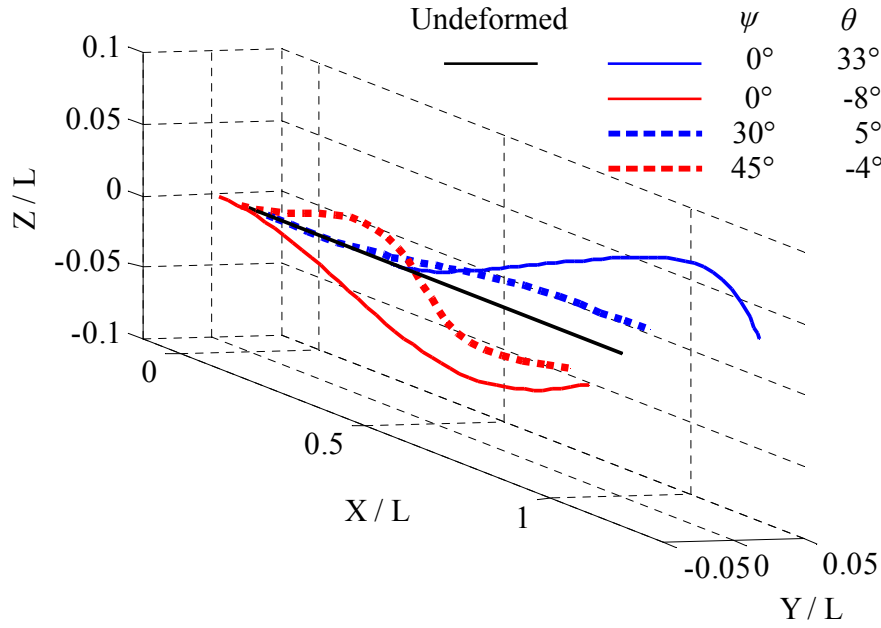
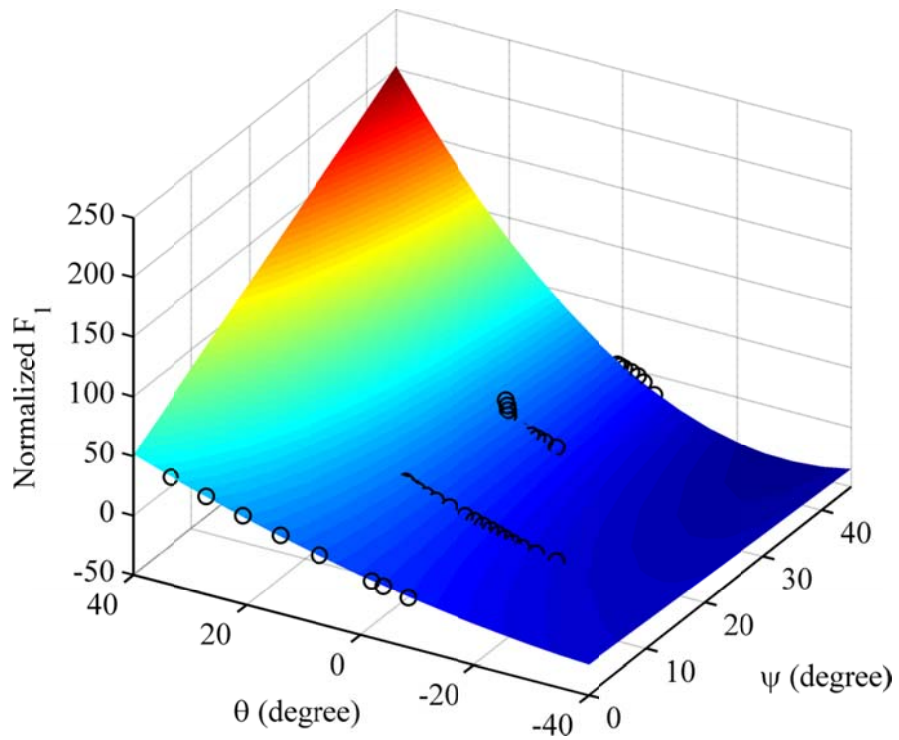


Figure 5.27 Deformed beam shapes for a pitching camera.

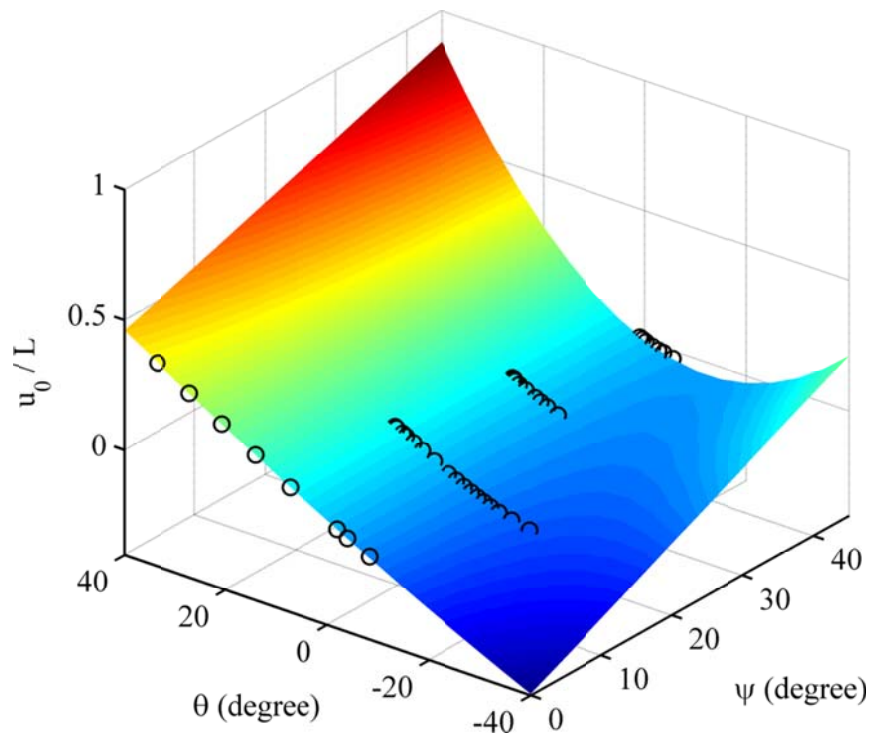
Figure 5.28 shows the required input (force F_1 or displacement u_0) of the rear axle to tilt the front axle for different ψ and θ . The black circles denote the simulated results and the interpolated surfaces of $F_1(\psi, \theta)$ and $u_0(\psi, \theta)$ can be quantified as follows:

$$F_1\left(\frac{4L^2}{\pi^2 EI_2}\right) = -0.15\theta + 54.54|\psi| + 147.32\theta|\psi| + 27.28\psi^2 + 182.01\theta\psi^2 + 2.50\theta^3 \quad (5.20a)$$

$$\frac{u_0}{L} = -0.0067\theta + 0.61|\psi| - 0.17\theta|\psi| + 0.07\psi^2 + 1.34\theta\psi^2 + 0.015\theta^3 \quad (5.20b)$$



(a) Normalized force from the rear axle.



(b) Normalized displacement of the rear axle.

Figure 5.28 Required input of the rear axle for different of ψ and θ .

Results are discussed as follows:

- 1) The input force F_1 is a nonlinear function of ψ and θ . Given an electric motor, the maximum output torque τ_m can be found from its specification sheet. Then the limits on the front axle tilting motion can be determined from $|F_1| \leq \frac{2\tau_m}{r_w}$.
- 2) For $\psi = 0$, u_0 is a linear function of θ which is similar to the case of corner negotiation in Section 5.3.3. As ψ increases, u_0 becomes nonlinear with θ because the beam deformation becomes 3-D and twisting along the beam is nonzero. However, u_0 is still the preferred control variable because displacement control is much simpler than force control.
- 3) The surface functions in (5.20) are obtained by multiple variable regression, where the functional form is determined such that it is an even function of ψ (because of symmetry) but odd function of θ because when $\theta > 0$, $F_1 > 0$, $u_0 > 0$ and when $\theta < 0$, $F_1 < 0$, $u_0 < 0$.

5.5 Summary

This chapter presents the design concept of a novel magnetic FMN incorporating a compliant beam and permanent magnets, and a 3-D model for simulating the deformed shape of the compliant beam. Simulation results show that there exist consistent relations between the input/output displacements and rotation angle for open-loop control implementation in sensor attachment and corner negotiation regardless of gravity direction or the critical force for buckling. The theoretical models for sensor attachment and corner negotiation are also experimentally validated .

Along with an analytical model for simulating the large deformation of a compliant beam in 2D space, a magnetic flexonic mobile node (FMN) incorporating a compliant mechanism has been designed to negotiate corners and carry a sensor for placing on a ferromagnetic structure. Two illustrative examples of sensor attachment and corner negotiation are presented for different constraints for the same mechanical design of FMN. Simulation results show that there exist consistent relations between input/output displacements and rotation angle for control implementation in sensor attachment and corner negotiation regardless of gravity direction. In sensor attachment, a nonlinear relation between the front assembly displacement and the sensor displacement is valid for different critical forces for buckling which is affected by the working surface slope. In corner negotiation, a linear relation can be obtained between the displacement of the rear assembly and the rotation angle of the front assembly within the highly nonlinear load-displacement behaviors of a compliant beam. However, the gravity affects the loading and displacement/rotation angle relation. To set off the beam buckling for the sensor attachment, the smaller the surface slope angle, the larger the critical force needed; a heavier sensor weight tends to give rise to a larger critical force for slope angle $\varphi \leq 45^\circ$ while smaller critical force for $\varphi > 45^\circ$. For a desired rotation angle in corner negotiation, a larger pushing force is required with a larger angle ψ between the gravity and the norm of the initial plane. The analytical model is validated by an experiment on a cantilever beam and the corresponding FE model. Finally, the experimental results of two functionalities of sensor attachment and corner negotiation are provided to validate the simulation analysis.

CHAPTER VI

CONCLUSIONS AND FUTURE WORKS

6.1 Conclusions

A Curvature-based Beam Model (CBM) has been rigorously formulated and validated for solving 3-D large deformation problems in which a compliant beam plays an important role. The following summarizes contributions made in this thesis:

- 1) CBM using global coordinates

The 3-D large deformation formulation based on curvature distinguishes itself from other methods, such as FEM, based on displacements and/or rotational angles in that the principle of superposition holds even for large rotation; hence, the formulation based on curvature is much simpler; and the results can be efficiently computed.

The advantage of curvature description by formulating all state variables of a curved 3-D beam in the global reference frame has been fully explored. The relation between the curvature and absolute nodal coordinates of a curved beam is derived. It has shown that the curvature characterizes curved beam geometry via three differential equations. The CBM is verified by the FEM through the large deformation analysis of 3-D curved beams under cantilever constraints.

2) The generalized bio-joint constraint

The bio-joint constraint (BJC) has been described as a generalized boundary condition for the CBM, which relaxes common assumptions in traditional boundary constraints such as fixed, pinned or sliding constraint where none or only one DOF is allowed. This generalized constraint is capable to emulate multi-DOF motions of a natural biological joint. The BJC is formulated as a contact constraint between two rigid bodies approximated locally as two ellipsoids for ease of illustration. Applications to the knee joint kinematic and dynamic analysis are discussed in details.

3) Bio structure modeling

For the first time, an overall bio structure accounting for both soft tissues and bones has been modeled as a multi-body compliant mechanism. By formulating the boundary conditions for the CBM as bio-joint constraints, a musculoskeletal model characterizes the bone and soft tissue deformation by accounting for the large size variation of natural products. Given the large variation of force profiles among specimens, the proposed model agrees well with experiment results.

An application of the musculoskeletal model to wing manipulation is illustrated by analyzing the effects of size variations on the required manipulating force and the shoulder deformation. This musculoskeletal model can be potentially used to develop design criteria to automate the process of de-boning chicken breast-meat. While it is written in the context of poultry meat de-boning, the method can be used in other bio-tissues, joints, and systems.

4) Bio inspired robot design

With the analysis of a bio structure in mind, the modeling method of a CBM can be used to design a flexible structure for field robots to emulate the dexterities of bio-joints. The design concept of incorporating a compliant beam is presented to replace traditional pin joint configuration of a two-axle autonomous robot. Possible situations in deforming the compliant beam for specific applications in structure health monitoring (SHM) are numerically analyzed and experimentally validated. Based on the analysis with normalized form of CBM, a compliant beam has been designed for a prototype flexonic mobile node (FMN).

6.2 Future Works

The analysis of a multi-body system formulated using the CBM with the BJC provides a foundation for other research in the area of bioengineering. Future works are summarized as followed:

- 1) In this thesis, the CBM with the BJC is formulated only for quasi-static cases, where the deformation is assumed to accumulate in a very slow speed. In order to better understand the dynamic response of bio structures, such as flapping of bird wings or fish tails, a complete formulation of the dynamic model is necessary. In order to do this, two recommendations are listed:
 - a. The BJC has been formulated to facilitate for differentiation in the time domain, so it is readily used for kinematic and dynamic analysis. It just requires proper expression of the boundary constraints on the beam dynamic equations.

- b. The dynamic form of CBM requires additional inertia terms consisting of masses and time derivatives, which transforms the current ODE into a PDE.

For example, (2.22) would become

$$m \frac{\partial \mathbf{x}}{\partial t^2} + \frac{\partial \mathbf{F}}{\partial s} = -\mathbf{q}_F$$

where m is the mass per length along the beam axis.

- 2) In the view of applications, the CBM can be extended to account for coupling effects among multiple physical fields, such as magnetic field or thermal dynamics. This is achievable via explicitly determining the distributed force \mathbf{q}_F and distributed moment \mathbf{q}_M as the quantities in corresponding fields. For example, in considering the magnetic effects on structural deformation, \mathbf{q}_F and \mathbf{q}_M are the corresponding magnetic force and moment.
- 3) The BJC considered in this thesis employs ellipsoids in the modeling, which captures the non-uniform shapes of bio joints in general. For specific applications, more accurate geometry description rather than the elliptic approximation would be required. In this case, the curvature description will be valid for such purposes.

APPENDIX A

DERIVATION OF CURVATURE

In Chapter 2, both rotational matrix and curvature are used to describe the curved shape of a beam axis. Since only three components in a rotational matrix are independent, a rotational matrix is mutually interchangeable with a three-component vector of curvature. This appendix shows how they are correlated and a theorem will be proved.

Given any curve in a 3D space, the moving frame along its axis has been given in (2.1). Without losing generality, the compact tensor form of (2.1) can be expand into the following matrix form:

$$\begin{Bmatrix} \mathbf{e}_1 \\ \mathbf{e}_2 \\ \mathbf{e}_3 \end{Bmatrix} = [\mathbf{R}] \begin{Bmatrix} \mathbf{E}_1 \\ \mathbf{E}_2 \\ \mathbf{E}_3 \end{Bmatrix} \quad (\text{A.1})$$

Then, taking the derivative with respect to the path length s

$$\frac{d}{ds} \begin{Bmatrix} \mathbf{e}_1 \\ \mathbf{e}_2 \\ \mathbf{e}_3 \end{Bmatrix} = \frac{d[\mathbf{R}]}{ds} \begin{Bmatrix} \mathbf{E}_1 \\ \mathbf{E}_2 \\ \mathbf{E}_3 \end{Bmatrix} = \frac{d[\mathbf{R}]}{ds} [\mathbf{R}]^T \begin{Bmatrix} \mathbf{e}_1 \\ \mathbf{e}_2 \\ \mathbf{e}_3 \end{Bmatrix} \quad (\text{A.2})$$

Then, the curvature $\mathbf{K} = [k_1 \ k_2 \ k_3]^T$ is defined as

$$\text{skew}(\mathbf{K}) = \begin{bmatrix} 0 & k_3 & -k_2 \\ -k_3 & 0 & k_1 \\ k_2 & -k_1 & 0 \end{bmatrix} = \frac{d[\mathbf{R}]}{ds} [\mathbf{R}]^T \quad (\text{A.3})$$

Ordinary differential equations governing \mathbf{R} can be expressed in terms of \mathbf{K} :

$$\frac{d[\mathbf{R}]}{ds} = skew(\mathbf{K})[\mathbf{R}]^T \quad (\text{A.4})$$

Theorem A.1: Given \mathbf{R} as any rotational matrix, $[\mathbf{A}] = \frac{d[\mathbf{R}]}{ds}[\mathbf{R}]^T$ is a skew matrix.

Proof: For a rotational matrix \mathbf{R} , it satisfies the following condition

$$[\mathbf{R}][\mathbf{R}]^T = [\mathbf{R}]^T[\mathbf{R}] = [\mathbf{I}]$$

where $[\mathbf{I}]$ is an identity matrix.

$$\begin{aligned} [\mathbf{A}] + [\mathbf{A}]^T &= \frac{d[\mathbf{R}]}{ds}[\mathbf{R}]^T + [\mathbf{R}]\frac{d[\mathbf{R}]^T}{ds} \\ &= \frac{d[\mathbf{R}][\mathbf{R}]^T}{ds} = \frac{d[\mathbf{I}]}{ds} \\ &= 0 \end{aligned}$$

Hence, $[\mathbf{A}] = -[\mathbf{A}]^T$ is a skew matrix. \square

So the curvature \mathbf{K} has been introduced in the form of a skew matrix for the derivative of the moving frame along the path length s ,

$$\frac{d}{ds} \begin{Bmatrix} \mathbf{e}_1 \\ \mathbf{e}_2 \\ \mathbf{e}_3 \end{Bmatrix} = skew(\mathbf{K}) \begin{Bmatrix} \mathbf{e}_1 \\ \mathbf{e}_2 \\ \mathbf{e}_3 \end{Bmatrix} \quad (\text{A.5})$$

It is clear that \mathbf{K} is independent of what referenced frame $\{\mathbf{E}_i\}$ ($i = 1, 2$ and 3) is chosen and determined by the geometry of curve via the rotational matrix in (A.3).

APPENDIX B

MULTIPLE SHOOTING METHOD (MSM)

The boundary condition problem (BVP) of a 3D compliant beam can be written in the following form:

$$\mathbf{X}' = \mathbf{f}(s, \mathbf{X}), \quad \mathbf{g}(\mathbf{X}(0), \mathbf{X}(l)) = \mathbf{0} \quad (\text{B.1})$$

where \mathbf{X} is a vector of the 13 variables; $0 \leq s \leq l$; and $\mathbf{g}(\bullet)$ is the boundary conditions specifying the geometrical loading constraints at both ends. The BVP (B.1) is recast as an IVP and solved using a MSM [34, 35]. For this, the region $[0, l]$ is divided into $m-1$ sections by m nodes as shown in Figure B.1, where s_i is the arc length from the root of the beam to the i^{th} node; $x_i^{(n)}$ is the initial guesses for the i^{th} section, and the superscript (n) denotes the n^{th} guess.

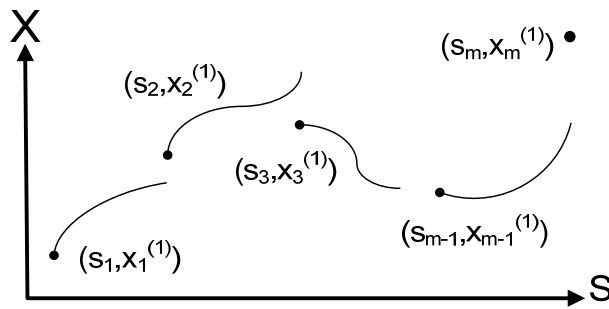


Figure B.1 Multiple shooting method.

The BVP can then be posed as a set of m first-order non-linear equations (B.2) subject to a set of m constraints (B.3) as functions of the initial guesses:

$$\mathbf{X}' = \mathbf{f}(s, \mathbf{X}), \quad \mathbf{X}(s_i) = \mathbf{x}_i^{(n)} \quad (\text{B.2})$$

$$\mathbf{C}(\mathbf{x}^{(n)}) := \begin{bmatrix} \mathbf{C}_1(\mathbf{x}_1^{(n)}, \mathbf{x}_2^{(n)}) \\ \vdots \\ \mathbf{C}_{m-1}(\mathbf{x}_{m-1}^{(n)}, \mathbf{x}_m^{(n)}) \\ \mathbf{C}_m(\mathbf{x}_1^{(n)}, \mathbf{x}_m^{(n)}) \end{bmatrix} := \begin{bmatrix} \mathbf{X}(s_2; s_1, \mathbf{x}_1^{(n)}) - \mathbf{x}_2^{(n)} \\ \vdots \\ \mathbf{X}(s_m; s_{m-1}, \mathbf{x}_{m-1}^{(n)}) - \mathbf{x}_m^{(n)} \\ \mathbf{g}(\mathbf{x}_1^{(n)}, \mathbf{x}_m^{(n)}) \end{bmatrix} \quad (\text{B.3})$$

Using Newton method, the initial guesses are updated using (A.4):

$$\mathbf{x}^{(n+1)} = \mathbf{x}^{(n)} - \alpha \left[DC(\mathbf{x}^{(n)}) \right]^{-1} \mathbf{C}(\mathbf{x}^{(n)}), \quad n = 0, 1, \dots \quad (\text{B.4})$$

where $DC = \partial \mathbf{C} / \partial \mathbf{x}^{(n)}$ is a matrix, α is a coefficient for the iteration step size. The iteration process of (A.4) stops until $\mathbf{C}(\mathbf{x}^{(n)}) \rightarrow \mathbf{0}$ (or a small tolerance error Err_{tol}) implying that the solution is continuous and satisfies the boundary conditions. The MSM can be implemented using the following steps:

- 1) Set the initial guess $\mathbf{x}^{(0)} = [\mathbf{x}_1^{(0)} \quad \mathbf{x}_2^{(0)} \quad \dots \quad \mathbf{x}_m^{(0)}]$.
- 2) Solve the IVP with $\mathbf{X}(0) = \mathbf{x}^{(0)}$.
- 3) Calculate the residual $\|\mathbf{C}(\mathbf{x}^{(0)})\|$ and corresponding $DC = \partial \mathbf{C} / \partial \mathbf{x}^{(0)}$.
- 4) Update the initial guess by (B.4).
- 5) Repeat steps 2~4 (replacing $\mathbf{x}^{(0)}$ with $\mathbf{x}^{(n)}$) until $\|\mathbf{C}(\mathbf{x}^{(n)})\| < \text{tolerance error}$
 Err_{tol} .

REFERENCES

- [1] S. Genc, R. W. Messler, and G. A. Gabriele, "A systematic approach to integral snap-fit attachment design," *Research in Engineering Design-Theory Applications and Concurrent Engineering*, vol. 10, pp. 84-93, 1998.
- [2] V. Seidemann, S. Butefisch, and S. Buttgenbach, "Fabrication and investigation of in-plane compliant su8 structures for mems and their application to micro valves and micro grippers," *Sensors and Actuators a-Physical*, vol. 97-8, pp. 457-461, Apr 2002.
- [3] B.-J. Yi, G. B. Chung, H. Y. Na, W. K. Kim, and I. H. Suh, "Design and experiment of a 3-dof parallel micromechanism utilizing flexure hinges," *Robotics and Automation, IEEE Transactions on*, vol. 19, pp. 604-612, Aug. 2003.
- [4] W. Daley, T. He, K.-M. Lee, and M. Sandlin, "Modeling of the natural product deboning process using biological," *Advanced Intelligent Mechatronics, IEEE/ASME International Conference on*, pp. 49-54, 1999.
- [5] K.-M. Lee, Y. Wang, D. Zhu, J. Guo, and X. Yi, "Flexure-based mechatronic mobile sensors for structure damage detection," in *the 7th International Workshop on Structural Health Monitoring*, Stanford CA, USA, 2009.
- [6] K.-M. Lee and J. Guo, "Bio joint kinematic model for flexible deboning automation," presented at the International Symposium on Flexible Automation (ISFA), Atlanta, GA, USA, 2008.
- [7] J. Guo and K.-M. Lee, "Effects of musculoskeleton model on flexible deboning automation," presented at the International Symposium on Flexible Automation (ISFA), Atlanta, GA, USA, 2008.
- [8] L. L. Howell, *Compliant mechanisms*, 1st ed. New York: John Wiley and Sons, Inc, 2001.
- [9] J. M. Gere and S. P. Timoshenko, *Mechanics of materials*, 4th ed. Boston: PWS, 1997.
- [10] S. P. Timoshenko, "On the transverse vibrations of bars of uniform cross-section," *Philosophical Magazine*, vol. 43, pp. 125-131, Jan 1922.
- [11] R. Frisch-Fay, *Flexible bars*. Washington, D.C.: Butterworths, 1962.

- [12] P. F. Pai and A. H. Nayfeh, "A fully nonlinear theory of curved and twisted composite rotor blades accounting for warpings and three-dimensional stress effects," *International Journal of Solids and Structures*, vol. 31, pp. 1309-1340, May 1994.
- [13] P. F. Pai and A. N. Palazotto, "Large-deformation analysis of flexible beams," *International Journal of Solids and Structures*, vol. 33, pp. 1335-1353, Apr 1996.
- [14] R. A. Laskin, P. W. Likins, and R. W. Longman, "Dynamical equations of a free-free beam subject to large overall motions," *Journal of the Astronautical Sciences*, vol. 31, pp. 507-527, 1983.
- [15] T. R. Kane, R. R. Ryan, and A. K. Banerjee, "Dynamics of a cantilever beam attached to a moving base," *Journal of Guidance Control and Dynamics*, vol. 10, pp. 139-151, Mar-Apr 1987.
- [16] J. C. Simo and L. Vuquoc, "On the dynamics of flexible beams under large overall motions - the plane case .1," *Journal of Applied Mechanics-Transactions of the Asme*, vol. 53, pp. 849-854, Dec 1986.
- [17] J. C. Simo and L. Vuquoc, "On the dynamics of flexible beams under large overall motions - the plane case .2," *Journal of Applied Mechanics-Transactions of the Asme*, vol. 53, pp. 855-863, Dec 1986.
- [18] A. A. Shabana and R. Y. Yakoub, "Three dimensional absolute nodal coordinate formulation for beam elements: Theory," *Journal of Mechanical Design*, vol. 123, pp. 606-613, Dec 2001.
- [19] D. E. Stewart, "Rigid-body dynamics with friction and impact," *Siam Review*, vol. 42, pp. 3-39, Mar 2000.
- [20] D. E. Stewart, "Convolution complementarity problems with application to impact problems," *Ima Journal of Applied Mathematics*, vol. 71, pp. 92-119, Feb 2006.
- [21] P. Song, P. Kraus, V. Kumar, and P. Dupont, "Analysis of rigid-body dynamic models for simulation of systems with frictional contacts," *Journal of Applied Mechanics-Transactions of the Asme*, vol. 68, pp. 118-128, Jan 2001.
- [22] S. Adly and D. Goeleven, "A stability theory for second-order nonsmooth dynamical systems with application to friction problems," *Journal De Mathematiques Pures Et Appliquees*, vol. 83, pp. 17-51, Jan 2004.
- [23] N. Kikuchi and J. T. Oden, *Contact problems in elasticity: A study of variational inequalities and finite element methods*. Philadelphia: SIAM, 1988.
- [24] T. A. Laursen and J. C. Simo, "A continuum-based finite-element formulation for the implicit solution of multibody, large-deformation frictional contact problems,"

International Journal for Numerical Methods in Engineering, vol. 36, pp. 3451-3485, Oct 1993.

- [25] R. Kelkar, V. M. Wang, E. L. Flatow, P. M. Newton, G. A. Ateshian, L. U. Bigliani, R. J. Pawluk, and C. C. Mow, "Glenohumeral mechanics: A study of articular geometry, contact, and kinematics," *Journal of Shoulder and Elbow Surgery*, vol. 10, pp. 73-84, Jan-Feb 2001.
- [26] H. Iwaki, V. Pinskerova, and M. A. R. Freeman, "Tibiofemoral movement 1: The shapes and relative movements of the femur and tibia in the unloaded cadaver knee," *Journal of Bone and Joint Surgery-British Volume*, vol. 82B, pp. 1189-1195, Nov 2000.
- [27] B. D. Yang and C. H. Menq, "Characterization of 3d contact kinematics and prediction of resonant response of structures having 3d frictional constraint," *Journal of Sound and Vibration*, vol. 217, pp. 909-925, Nov 1998.
- [28] D. J. Montana, "The kinematics of contact and grasp," *International Journal of Robotics Research*, vol. 7, pp. 17-32, Jun 1988.
- [29] K.-M. Lee, "On the development of a compliant grasping mechanism for online handling of live objects. I. Analytical model," in *Advanced Intelligent Mechatronics (AIM), Proceedings of IEEE/ASME International Conference on*, 1999, pp. 354-359.
- [30] K.-M. Lee, A. B. Webster, J. Joni, X. Yin, R. Carey, M. P. Lacy, and R. Gogate, "On the development of a compliant grasping mechanism for online handling of live objects. Ii. Design and experimental investigation," in *Advanced Intelligent Mechatronics (AIM), Proceedings of IEEE/ASME International Conference on*, 1999, pp. 360-365.
- [31] X. Yin, K.-M. Lee, and C.-C. Lan, "Computational models for predicting the deflected shape of a non-uniform, flexible finger," in *Robotics and Automation (ICRA), Proceedings of IEEE International Conference on*, 2004, vol. 3, pp. 2963-2968.
- [32] C.-C. Lan and K.-M. Lee, "Generalized shooting method for analyzing compliant mechanisms with curved members," *Journal of Mechanical Design*, vol. 128, pp. 765-775, Jul 2006.
- [33] Q. Li and K.-M. Lee, "An adaptive meshless method for analyzing large mechanical deformation and contacts," *Journal of Applied Mechanics-Transactions of the Asme*, vol. 75, Jul 2008.
- [34] H. B. Keller, *Numerical methods for two-point boundary-value problems*. Waltham, Massachusetts.: Blaisdell, 1968.

- [35] J. Stoer and R. Bulirsch, *Introduction to numerical analysis*. New York: Springer-Verlag, 1993.
- [36] R. Holsapple, R. Venkataraman, and D. Doman, "A modified simple shooting method for solving two-point boundary-value problems," in *Aerospace Conference, IEEE Proceedings. of 2003*, vol. 6, pp. 2783-2790.
- [37] C. S. Liu, "The lie-group shooting method for nonlinear two-point boundary value problems exhibiting multiple solutions," *Cmes-Computer Modeling in Engineering & Sciences*, vol. 13, pp. 149-163, May 2006.
- [38] C. M. Wang and S. Kitipornchai, "Shooting optimization technique for large deflection analysis of structural members," *Engineering Structures*, vol. 14, pp. 231-240, 1992.
- [39] S. R. Li and Y. H. Zhou, "Shooting method for non-linear vibration and thermal buckling of heated orthotropic circular plates," *Journal of Sound and Vibration*, vol. 248, pp. 379-386, Nov 2001.
- [40] C.-C. Lan, K.-M. Lee, and J.-H. Liou, "Dynamics of highly elastic mechanisms using the generalized multiple shooting method: Simulations and experiments," *Mechanism and Machine Theory*, vol. 44, pp. 2164-2178, Dec 2009.
- [41] J. R. Chang, C. S. Liu, and C. W. Chang, "A new shooting method for quasi-boundary regularization of backward heat conduction problems," *International Journal of Heat and Mass Transfer*, vol. 50, pp. 2325-2332, Jun 2007.
- [42] C. S. Liu, "Identifying time-dependent damping and stiffness functions by a simple and yet accurate method," *Journal of Sound and Vibration*, vol. 318, pp. 148-165, Nov 2008.
- [43] M. C. Sandlin, "Model-based vision-guided automated cutting of natural products," Master, Mechanical Engineering, Georgia Institute of Technology, Atlanta, 1998.
- [44] T. He, "Effects of rotor configurations on the characteristic torque of a variable-reluctance spherical motor," Ph.D., Mechanical Engineering, Georgia Institute of Technology, Atlanta, 2000.
- [45] K.-M. Lee and C.-K. Kwan, "Design concept development of a spherical stepper for robotic," *Robotics and Automation, IEEE Transactions on*, vol. 7, pp. 175-181, Feb 1991.
- [46] M. R. Claffee, "The effects of wing manipulation on automated cutting of biological materials," Master, Mechanical Engineering, Georgia Institute of Technology, Atlanta, 2006.

- [47] *Joints and corresponding models*. Available: <http://ovrt.nist.gov/projects/vrml/h-anim/jointInfo.html> (last accessed in November 2011).
- [48] R. Huiskes, J. Kremers, A. Delange, H. J. Woltring, G. Selvik, and T. J. G. Vanrens, "Analytical stereophotogrammetric determination of 3-dimensional knee-joint geometry," *Journal of Biomechanics*, vol. 18, pp. 559-570, 1985.
- [49] N. Nuno and A. M. Ahmed, "Three-dimensional morphometry of the femoral condyles," *Clinical Biomechanics*, vol. 18, pp. 924-932, Dec 2003.
- [50] B. Esser, J. Miller, D. Huston, and P. Bourn, "Robotic systems for homeland security," in *Conference on Nondestructive Detection and Measurement for Homeland Security II*, San Diego, CA, 2004, vol. 5395, pp. 134-142.
- [51] T. Yukawa, M. Suzuki, Y. Satoh, and H. Okano, "Design of magnetic wheels in pipe inspection robot," presented at the Systems, Man and Cybernetics (SMC), IEEE International Conference on, 2006.
- [52] F. Tache, W. Fischer, G. Caprari, R. Siegwart, R. Moser, and F. Mondada, "Magnebike: A magnetic wheeled robot with high mobility for inspecting complex-shaped structures," *Journal of Field Robotics*, vol. 26, pp. 453-476, May 2009.
- [53] P. G. Backes, Y. Bar-Cohen, and B. Joffe, "The multifunction automated crawling system (macs)," in *Robotics and Automation, Proceedings., IEEE International Conference on*, 1997, vol. 1, pp. 335-340.
- [54] J. Z. Xiao, W. Morris, N. Chakravarthy, and A. Calle, "City-climber: A new generation of mobile robot with wall-climbing capability - art. No. 62301d," in *Unmanned systems technology viii, pts 1 and 2*. vol. 6230, G. R. S. C. M. G. D. W. Gerhart, Ed., ed Bellingham: Spie-Int Soc Optical Engineering, 2006, pp. D2301-D2301.
- [55] Y. Ota, K. Yoneda, T. Tamaki, and S. Hirose, "A walking and wheeled hybrid locomotion with twin-frame structure robot," presented at the Intelligent Robots and Systems, IEEE/RSJ International Conference on, 2002.
- [56] S. Ahmad, "Control of cooperative multiple flexible joint robots," *Systems, Man and Cybernetics, IEEE Transactions on*, vol. 23, pp. 833-839, May/June 1993.
- [57] M. A. Arteaga and B. Siciliano, "On tracking control of flexible robot arms," *Automatic Control, IEEE Transactions on*, vol. 45, pp. 520-527, Mar 2000.
- [58] M. Filipovic and M. Vukobratovic, "Modeling of flexible robotic systems," in *Computer as a Tool. EUROCON. The International Conference on*, 2005, vol. 2, pp. 1196-1199.

- [59] J. G. Garcia, A. Robertsson, J. G. Ortega, and R. Johansson, "Sensor fusion for compliant robot motion control," *Robotics, IEEE Transactions on*, vol. 24, pp. 430-441, April 2008.
- [60] J. Guo, K. M. Lee, D. Zhu, X. Yi, and Y. Wang, "Large-deformation analysis and experimental validation of a flexure-based mobile sensor node," *Mechatronics, IEEE/ASME Transactions on*, vol. PP, pp. 1-11, 2011.
- [61] H. W. Guggenheimer, *Differential geometry*. New York: Dover Publications, 1977.
- [62] T. Nomiya, A. Lawi, T. Katsuhara, and S. Hirokawa, "Model analysis of lower limb at deep knee flexion," in *Proceedings of the International Conference on Electrical Engineering and Informatics*, Institut Teknologi Bandung, Indonesia, 2007.
- [63] Y. C. B. Fung, "Elasticity of soft tissues in simple elongation," *American Journal of Physiology*, vol. 213, pp. 1532-1544, 1967.
- [64] J. Kastelic, I. Palley, and E. Baer, "The multicomposite ultrastructure of tendon," *Conn. Tiss. Res.*, vol. 6, pp. 11-23, 1978.
- [65] S. H. Foong and K. M. Lee, "Magnetic field-based multi-dof orientation sensor for pm-based spherical actuators," in *Advanced Intelligent Mechatronics (AIM), 2009 IEEE/ASME International Conference on*, Singapore, 2009, vol. 1-3, pp. 481-486.